UNIVERSITY OF OKLAHOMA

GRADUATE COLLEGE

EXPLORING TORNADOGENESIS WITH HIGH-RESOLUTION SIMULATIONS INITIALIZED WITH REAL DATA

A DISSERTATION

SUBMITTED TO THE GRADUATE FACULTY

in partial fulfillment of the requirements for the

Degree of

DOCTOR OF PHILOSOPHY

By

ALEXANDER DANIEL SCHENKMAN
Norman, Oklahoma
2012

EXPLORING TORNADOGENESIS WITH HIGH-RESOLUTION SIMULATIONS INITIALIZED WITH REAL DATA

A DISSERTATION APPROVED FOR THE
SCHOOL OF METEOROLOGY

BY

_____
Dr. Ming Xue, Chair

_____
Dr. Alan Shapiro

_____
Dr. Keith Brewster

_____
Dr. Jidong Gao

_____
Dr. Lance Leslie

_____
Dr. Julia Ehrhardt

Acknowledgements

My completion of this dissertation and Ph. D. was made possible by a great number of great people. First, I would like to thank my advisor, Dr. Ming Xue, for his help, advice, and encouragement over the last four years. I also very much appreciate him giving me the freedom to explore areas that were of great interest to me. To me, this freedom reflects an unwavering confidence that Ming has had in my abilities as a student and scientist. This confidence is contagious and allowed me to press on with my research even during the times when I felt like I was not getting anywhere. Additionally, I think that being able to research tornadogenesis has made many of my fellow graduate students a little bit jealous over the years. Having the freedom to research such an interesting problem has been fantastic.

Next, I would like to thank Dr. Alan Shapiro for many informal meetings in which we discussed vorticity dynamics, surface drag, and of course delicious food and beer. Alan's impressive knowledge of these important topics has been instrumental in the completion of my degree. I also consider him a good friend, in addition to a mentor. Camping trips and Grillfests hosted by Alan are some the best times I have had in my whole ten years in Oklahoma.

Thank you also to the rest of my committee members: Drs. Keith Brewster, Jidong Gao, Lance Leslie, and Julia Ehrhardt.

My friends and peers (there are too many to name them all) at the University of Oklahoma and in the School of Meteorology have been instrumental in research discussions and keeping me sane. Thanks to Brett Roberts for many discussions and for working with me on the trajectory code. Discussions with Dr. Mike French about the

myth of the descending TVS have helped validate my own research. Huge thanks to my roommate Dr. Matt Kumjian. Late night discussions with Matt about research have been invaluable in allowing me to clarify my thoughts and ideas. Matt also has served as an informal reviewer for my papers and has been my partner in crime in making the School of Meteorology, the University of Oklahoma, and Norman a more bizarre and interesting place.

On a more personal note, I want to thank my girlfriend, Melissa, for her patience, love, support, and understanding. Her incredible work ethic and ability to somehow do everything (and do it well) is a huge source of inspiration.

Also, thanks to my mom and my dad. My mom, Susan, instilled a go get 'em , no-procrastination mentality in me. I also believe that I became interested in meteorology and science because she always watched (and enjoyed) The Weather Channel, Nova, and other educational programs on PBS when I was growing up. Her love and support has been invaluable throughout graduate school. She is, empirically, the best mom in the world. And, I must thank her for coming out to Oklahoma to help me move out of my apartment, a task that seemed nearly as insurmountable as doing a Ph. D! Thanks to my dad, Max, for being supportive and for teaching me how to be a really good undergraduate and graduate student. By that I mean, of course, for teaching me how to get free stuff!

I also want to acknowledge the rest of my family: OTAF, OTUW, Grandma Gibbons, Grandma Anne, Walter, Angela, Janelle, Auntie Debbie and many more (sorry if I forgot someone, it is getting late!). You are all so wonderful and loving and I could not have done it without you!

Financial support for this dissertation came primarily from NSF grants EEC-0313747 and AGS-0802888. This work used the Extreme Science and Engineering Discovery Environment (XSEDE), which is supported by National Science Foundation grant number OCI-1053575. Some of the computing for this project was performed at the OU Supercomputing Center for Education & Research (OSCER) at the University of Oklahoma (OU).

Table of Contents

List of Figures

Abstract

Despite large advances in our understanding of tornadogenesis over the past fifty years, a comprehensive dynamical understanding of the processes behind tornado formation remains elusive. The purpose of this dissertation is to augment the current body of knowledge by exploring the dynamical processes responsible for tornadogenesis using high-resolution numerical weather prediction. To accomplish this goal, two high-resolution numerical simulations of tornadic storms were performed with the Advanced Regional Prediction System (ARPS) model. Both simulations were nested within lower-resolution domains that were initialized via high-frequency (5 min) data assimilation cycles conducted with the ARPS three dimensional variational (3DVAR) data assimilation package. Radar reflectivity and radial velocity, in addition to conventional observations, were assimilated in these five-minute assimilation cycles. In both simulations, tornadogenesis timing and location were well forecast.

The first simulation examined used 100-m grid spacing to simulate a tornadic mesovortex. The mesovortex was one of two tornadic mesovortices spawned by a mesoscale convective system (MCS) that traversed southwest and central Oklahoma on 8-9 May 2007.

Results from the 100-m simulation provide a detailed picture of the development of a mesovortex that produces a sub-mesovortex-scale tornado-like vortex (TLV). Closer examination of the genesis of the TLV suggests that a strong low-level updraft is critical in converging and amplifying vertical vorticity associated with the mesovortex. Vertical cross-sections and backward trajectory analyses from this low-level updraft reveal that the updraft is the upward branch of a strong rotor that forms just northwest

of the simulated TLV. The horizontal vorticity in this rotor originates in the near surface inflow and is caused by surface friction. An additional simulation with surface friction turned off does not produce a rotor, strong low-level updraft, or TLV. Comparison with previous two-dimensional numerical studies of rotors in the lee of mountains shows striking similarities to the rotor formation presented herein.

This study is the first to simulate, analyze, and propose a dynamical mechanism responsible for mesovortex tornadogenesis. This dynamical mechanism is summarized in a four-stage conceptual model that describes the evolution of the event from mesovortexgenesis through rotor development and finally TLV genesis and intensification.

The second case examined is a 50-m grid spacing simulation of the 8 May 2003 Oklahoma City tornadic supercell. This thunderstorm produced a strong, long-track tornado that produced F-4 damage on the south side of Oklahoma City. A 40-min forecast run on the 50-m grid produces two tornadoes that track within 10 km of the location of the observed long-track tornado.

The development of both simulated tornadoes is analyzed and presented with unprecedented detail in order to determine the processes responsible for tornadogenesis. This analysis reveals that tilting of low-level vorticity generated by surface drag plays an important role in the origin of vertical vorticity near the ground for both tornadoes. This result represents the first time that such a mechanism has been shown to be responsible for generating near-surface vertical vorticity leading to tornadogenesis. Two conceptual models are presented that summarize the development of the first and second tornado, respectively.

A simulation run without surface drag was found to be considerably different from the simulated with drag included. A tornado still developed in the no-drag simulation, but it was shorter-lived and took a substantially different track than the tornadoes in the drag simulation. Tilting of environmental vorticity in an outflow surge was determined to be the most likely cause of the tornado in the no-drag simulation.

Baroclinic vorticity generation was found to be unimportant in the development of the tornadoes in both the drag and the no-drag simulation. This is a marked departure from current theories of tornadogenesis and the broader implications of this finding, in addition to the important discovery of the substantial role of surface drag in the origins of near-surface vertical vorticity in the drag simulation, are discussed.

Errors in trajectory analysis are also discussed. A simple, one-dimensional flow is invoked to demonstrate the sensitivities of trajectory analysis to divergent/convergent flows. Possible remedies and alternatives to trajectory analysis are proposed for future work.

Chapter 1: Introduction

It has been nearly 50 years since Browning (1964) introduced the term 'supercell' to describe single large thunderstorm cells that move to the right of the mean flow. In the intervening years, research on supercells and tornadoes has yielded tremendous progress in our understanding of the dynamical processes responsible for these meteorological phenomena. Yet, despite large leaps in understanding, there remain a number of unanswered questions surrounding tornadoes and especially tornadogenesis. Specifically, a complete understanding of the dynamical processes behind tornadogenesis in supercells and other severe storms remains elusive. More importantly for practical applications, it is still not well understood why some storms spawn tornadoes while other, seemingly equally intense, storms do not. Because completely solving and answering the remaining questions surrounding tornadic storms is impossible in a single study, this dissertation seeks to augment the current body of knowledge by providing detailed analyses of two high-resolution numerical simulations of tornadic storms. The key mechanisms responsible for tornadogenesis in these simulations are explored and explained.

Both of the simulations discussed in this dissertation are of actual tornadic events that occurred in Oklahoma. The first simulation discussed is of a quasi-linear convective system (QLCS) that produced a few weak tornadoes in Oklahoma on 8 May 2007. The study of this case is particularly significant as it represents the first detailed study of the dynamics behind tornadogenesis in this type of meteorological scenario. The second simulation discussed is of a tornadic supercell that produced a large, damaging tornado in the Oklahoma City metro area on 8 May 2003. The major

assumption behind this entire dissertation is if a simulation faithfully reproduces reality, then maybe the dynamics governing the simulation are also similar to those that govern reality.

In the following chapter, the major assumption of this dissertation is given context by explaining the five major approaches used to study the dynamics of tornadic storms. The following chapter also reviews our current understanding of tornadic storms and highlights areas where understanding remains incomplete. Chapter 3 contains a detailed study of the tornadogenesis in a mesovortex associated with a quasi-linear convective system, focusing particularly on the important role surface friction plays in the case. Chapter 4 switches gears and discusses the simulation of the 8 May 2003 tornadic supercell. In chapter 5, the limitations of using Lagrangian trajectory analysis to dynamically understand an Eulerian simulation are explored and explained. This dissertation concludes with a discussion of key results and their implications for guiding future research.

Chapter 2: Review of Tornadic Storms.

As mentioned in the previous chapter there are five methods for studying the dynamics of tornadic storms: (i) observation based studies, (ii) studies using simple models, (iii) studies using more complex three-dimensional cloud models with highly-idealized initial conditions, (iv) studies in which data assimilation is used to synthesize observed data into three-dimensional model space, and (v) studies that assimilate observed data into a three-dimensional model and then run a simulation proceeding from this initial state. Of course, some studies contain more than one of these approaches and (v) is a subset and extension of (iv), however, for the most part, the main methodology of research in this area will focus on one of the above approaches. The first section of this chapter reviews the philosophy, advantanges, and disadvantages behind each of these five approaches. This is followed by a detailed review and synthesis of all five approaches leading to a summary of the present understanding of tornadic storms.

2.1 Five approaches for studying tornadic storms

2.1.1 Observational approach

Of the five approaches for studying tornadic storm dynamics the most utilized (at least, in terms of the number of publications) is the observational approach. As the name implies, the observational approach involves using direct or indirect observations of tornadic storms in order to glean some understanding of the important physical processes in tornadic storms. The observation types used in this category of research are wide-ranging and will be discussed in the following section of this chapter, but first the advantages and disadvantages of the observational approach are discussed.

Perhaps the single greatest advantage of the observational approach is that fact that observations are measurements of reality. This simple fact implies that, accounting for systematic errors in observational platforms, observations may be interpreted at face value. There is no need to be concerned that important physical processes are being neglected in an observational analysis because the observation is the result of all relevant physical processes occurring in the atmosphere. In other words, if an observational data set were to exist that measured all thermodynamic and kinematic variables everywhere within and close to a tornadic storm, there would be little ambiguity in the interpretation of such a data set with regard to the dynamical processes governing the tornadic storm.

Unfortunately, the collection of such a comprehensive data set is nearly impossible and would be prohibitively expensive. This brings up the main disadvantage of observational studies – they are generally very limited spatially and temporally. In addition, many important variables are generally only indirectly observed, if they are observed at all. This necessitates large assumptions and extrapolations about what the atmosphere is doing outside of observed areas and between observed times. This limitation may lead investigators to make incorrect conclusions about the governing dynamics behind a tornadic storm. It is possible that important processes are occurring that simply cannot be resolved or measured by the observational data, even in the most advanced observational study.

2.1.2 Simple models

The limitations of the observational approach have motivated many investigators to construct physical models in their search for understanding. The most

basic of these models (the simple model) can be constructed in order to isolate the impact of one (or perhaps a few) process(es) or parameter(s). This approach is appealing because the interpretation of results is greatly simplified when processes are isolated. Additionally, this approach can be compared to observations in order to determine the importance (or lack thereof) of a particular process. For example, if observations reveal a particular signature and a simple model that neglects most processes can reproduce, or even partially reproduce, that signature then the investigator can conclude with fairly high confidence that the process being modeled is physically important for the production of the signature in question.

While simple models can be useful in the situation outlined above, there are strong limitations on their applicability. Because of their inherent simplicity, in many cases, it is impossible to determine whether a process that a simple model indicates is important would still be important when other processes are included. For example, simple models have been used to study vortex dynamics and while these models can be used to explain behaviors observed in tornadoes, one must exercise caution as a different process or a combination of multiple other processes may combine to produce nearly identical vortex behavior in the real world.

A more specific limitation of simple models in their application to tornadic storms is the fact that tornadic storms are multi-scale phenomena. It is difficult in a simple model to represent the complex interactions between scales that are likely occurring between the tornado and the parent storm. Thus, while simple models are quite useful to investigate the importance of a process, conclusions about the

importance of that process to the overall convective storm must be at least somewhat speculative.

2.1.3 Non-hydrostatic numerical weather prediction

As a result of the limitations in the applicability of simple models to tornadic storms, many investigators have considered more complex atmospheric models. These models typically numerically solve the Navier-Stokes equations of motion and include many different physical processes, many of which are parameterized owing to computational cost or insufficient physical understanding. These models are initialized using some sort of idealized (or quasi-idealized) initial condition for the atmosphere. In principle, these models can be thought of as 'supercell in a box' type simulations. As such, it is assumed that if the simulations can reproduce key features of observed tornadic storms, the relevant physical processes in the model might also be the relevant physical processes in the real atmosphere. As long as this assumption is valid, the model can be used to examine the impact of varying different parameters on the behavior of the simulated storm.

When the above assumption is violated it can lead to incorrect conclusions and false diagnoses of the important processes in tornadic storms. As will be discussed in more detail later, an oversimplification in microphysical parameterizations appears to have led to researchers making an incorrect conclusion about the importance of a low-level baroclinic zone along the forward flank gust front in the development of low-level rotation in supercell thunderstorms. Observational studies were unable to verify the existence of this cold air suggesting that the models may have produced the right

answer for the wrong reasons. As such, results from this category of study must always be interpreted with this caveat in mind.

Another limitation of this approach is the difficulty of making direct attributions to specific parameters. In other words, because these models are quite complicated and non-linear, it can be difficult to isolate the impact of varying a single parameter upon the model solution. For the same reason, it is also can be fairly difficult to determine why the model solution proceeded in the manner it did. This can obfuscate the important processes and make conceptual understanding difficult for the investigator.

2.1.4 Storm-scale data assimilation

In order to combine the advantages of the observational and NWP approaches, investigators have begun using storm-scale data assimilation to extract as much information as possible from observations. Storm-scale data assimilation can provide many useful unobserved quantities by adjusting the model state based upon observed quantities. Similar to the idealized NWP approach, the key assumption behind data assimilation for the understanding of storm dynamics is: if the analyzed storm resembles the observed storm (especially when verified against independent observations), then perhaps the unobserved variables provided by the model analysis are accurate and can be used to provide a more complete picture of the storm than observations alone. Because the analysis uses real data, it should provide a dynamical analysis of the storm that is consistent with reality as long as the data assimilation produces an optimal analysis. This is the main advantage of the data assimilation method when compared to the idealized NWP approach

Unfortunately, the above assumption is often violated because of sub-optimal data assimilation. Sub-optimal data assimilation may give incorrect cross-variable correlations, developing relationships between model variables that may be artificial while missing relationships that are real. This could lead investigators to make incorrect conclusions based upon a data set they think is dynamically consistent but in reality is not. Moreover, in some data assimilation schemes some variables are analyzed in a separate step that virtually assures there will not be internal consistency between analyzed model variables. For example, in this dissertation a three-dimensional variational (3DVAR) data assimilation scheme is used along with a cloud analysis for moisture variables. Thus, there is no guarantee that moisture and mass fields will be dynamically consistent in the analysis.

The previous paragraph implies that success of this approach is likely case and data assimilation scheme dependent. This makes it difficult to generalize conclusions reached using this approach. Additionally, there is generally a paucity of independent observations with which to verify the accuracy of the data assimilation analysis.

2.1.5 Storm-scale data assimilation to initialize a simulation

A natural extension to the storm-scale data assimilation approach is to use the analysis as the initial condition for a forecast. This is the approach taken in this dissertation. As mentioned in the introductory chapter, the major assumption behind this approach is that if the model faithfully reproduces reality then perhaps the dynamical processes that drove the model solution are the same as those that govern reality. An advantage of running a simulation proceeding from the storm-scale data assimilation analysis is it can help constrain the model trajectory and assure the

investigator that the model is doing the right thing for the right reason. In other words, if the analysis and subsequent free-forecast both resemble reality it is unlikely that such a resemblance could occur only by coincidence.

Even with this approach's advantages, there are still many disadvantages which make this approach difficult. First, it is computationally expensive to perform storm-scale data assimilation and forecasts. Because results are likely case dependent, a large number of cases are necessary to make general conclusions implying the need for a great deal of computer resources. Even if the computer resources are readily available, there are likely a limited number of cases that have sufficient observational data required to produce a high quality analysis and subsequent forecast. In addition, as a result of inaccurate parameterizations, it is still possible that the model could produce the correct evolution of the storm for the wrong reason. Finally, as with the idealized NWP approach, the complexity and strong non-linearity of the model can preclude straightforward attribution of physical processes to the behavior of the modeled storm.

2.2 A review of tornadic supercell dynamics

Now that the five approaches for studying tornadic storms have been discussed, it is appropriate to review the knowledge of tornadic storms that has been acquired via studies in all five of these areas. For the sake of brevity, this review is mainly focused on studies that made significant contributions in our understanding of the dynamics of tornadoes and their parent storm. The review in this chapter is fairly general and reviews of topics more specifically related to the two cases studied and the methods therein are presented (as needed) in subsequent chapters.

2.2.1 Early studies of tornadic storms

It is perhaps most appropriate to begin this review with a discussion of Browning (1964), the paper that first coined the term supercell[1] to refer to single large cells that persist in a nearly steady state for several hours. Drawing on a collection of past studies, most of which used radar to analyze supercell storms (e.g., Stout and Huff 1953; Fujita 1958; Browning and Donaldson 1963), Browning (1964) developed a model of the airflow of supercell storms. In his schematic, inflow at low-levels feeds a vigorous updraft leading to the development of an echo-free precipitation vault. The precipitation formed in the updraft falls downstream of the inflow air, allowing the convective storm to persist. A downdraft occurs as dry mid-level air is chilled by evaporative cooling as it encounters precipitation along the downshear side of the updraft. Fig. 2.1 reproduces the three-dimensional schematic presented in Browning (1964).

Fujita was also actively researching supercells (though he did not call them that at the time) during the mid and late 1960's. Fujita (1965) and Fujita and Grandoso (1968) attempted to explain both hook echo development and storm-splitting with the Magnus force. Fujita explained that a rotating updraft initially at the center of a main precipitation area would drift to the south owing to the Magnus effect and would then advect precipitation around it leading to the development of a hook echo. The rotation in the thunderstorm was assumed to be from the amplification of pre-existing mesoscale rotation. Storm-splitting and the tendency for the splitting storms to propagate away from each other were also explained via the Magnus effect. Fujita conceptualized that

[1] It is interesting to note that the term 'supercell' is introduced in somewhat nonchalant manner and is only mentioned once in Browning (1964). It was not until the early 1970's and the research of John Marwitz that the term appears to have gained prominence in the literature.

an initial storm would give rise to two counter-rotating storms. The counter rotating storms were caused by the shedding of vortices as a result of mid-level winds flowing around the initial updraft which behaved as an obstacle. The new updrafts on either side of the original updraft captured these counter-rotating vortices. The Magnus effect then led to the cyclonic member to move south while the anti-cyclonic member moved north.

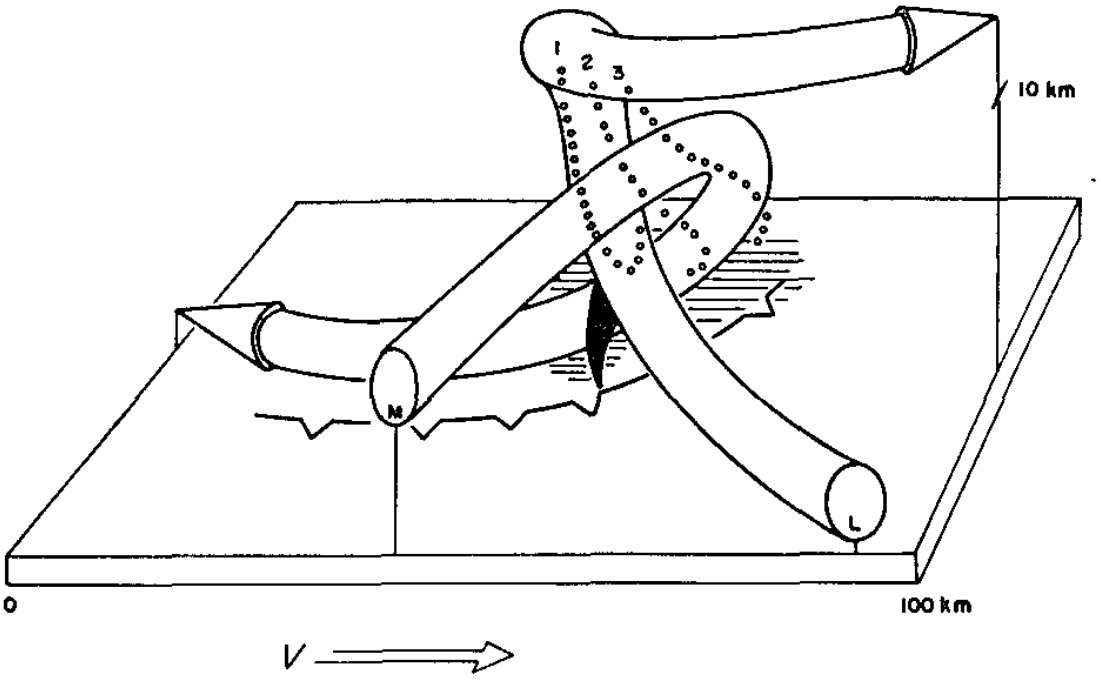

Fig. 2.1. Conceptual model of airflow in a supercell. Reproduced from Browning (1964).

While early studies identified that storms rotated, it was not until a report by Barnes (1968) that a more plausible mechanism for rotation was introduced. Barnes noted that little, if any, data were available to support the idea that thunderstorm rotation was the result of pre-existing mesoscale rotation. He then used proximity soundings from 16 severe weather cases and surmised that storm rotation was the result of the tilting of environmental horizontal vorticity (associated with vertical wind shear)

by the convective updraft. Barnes schematic of updraft tilting of environment horizontal vorticity is reproduced in Fig. 2.2.

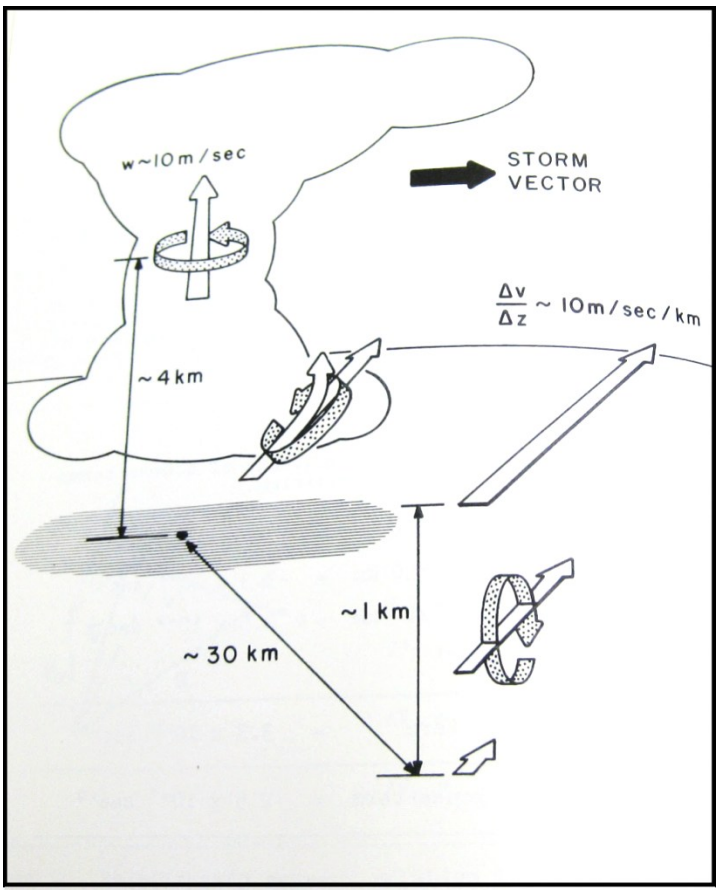

Fig. 2.2. Schematic showing how horizontal vorticity associated with the environmental vertical wind shear is tilted in a convective updraft. Reproduced from Barnes (1968).

The 1970's brought additional observational and the first numerical simulations of supercell thunderstorms. The conceptual model of Browning (1964) was updated by Marwitz (1972) to show the regions of updraft, large hail, and the visual cloud boundary. Brown et al. (1978) introduced the idea of the tornado vortex signature (TVS), a radial velocity couplet that appears aloft tens-of-minutes before a tornado is present at low-levels. The dynamic pipe effect (Leslie 1971), whereby convergent air into a mid-level vortex acquires rotation leading the vortex to extend downward to the ground, was invoked to explain the behavior of the TVS (Smith and Leslie 1978, 1979).

Lemon and Doswell (1979) represents the synthesis and culmination of the early observational studies of supercells and tornadoes. Drawing predominantly on analyses presented in Brown et al. (1973), Lemon (1976, 1977), Burgess et al. (1976; 1977), Lemon et al. (1978), Barnes (1978), and Brandes (1978), LD79 develops a three stage conceptual model of tornadic supercells. In the first stage, a deep, persistent convective updraft develops, slows down and turns to the right. This development leads into the second stage during which, LD79 state, large hail and funnel clouds are often observed. During this stage a bounded weak echo region (BWER) is typically observed to be collocated with a strong mid-level mesocyclone. This mesocyclone is completely within the updraft of the supercell at this time. The third stage of LD79's conceptual model begins when downdrafts strengthen and the mesocyclone descends while becoming divided [i.e., straddling the updraft-downdraft interface of the supercells main updraft and rear-flank downdraft (RFD)]. LD79 states that strong tornadoes are most likely to occur during this stage even though the storm is collapsing with weakening updrafts and strengthening downdrafts. LD79 speculated that strong tilting of vorticity in the strengthening RFD was responsible for tornadogenesis. Observations of the descending TVS were one of the main reasons they came to this conclusion.

LD79 also discusses the origin of the RFD, explaining that strong flow between 7 and 10 km is forced to descend as it impinges on the updraft. LD79 emphasize that while the RFD develops 7-10 km AGL, it is unlikely that air from these levels makes it all the way to the surface. Fig. 2.3 presents the planar conceptual model of a supercell from LD79. This conceptual model features separate forward-flank and rear-flank

downdrafts and gust fronts. The gust front structure and location of the tornado is reminiscent of an extratropical wave cyclone.

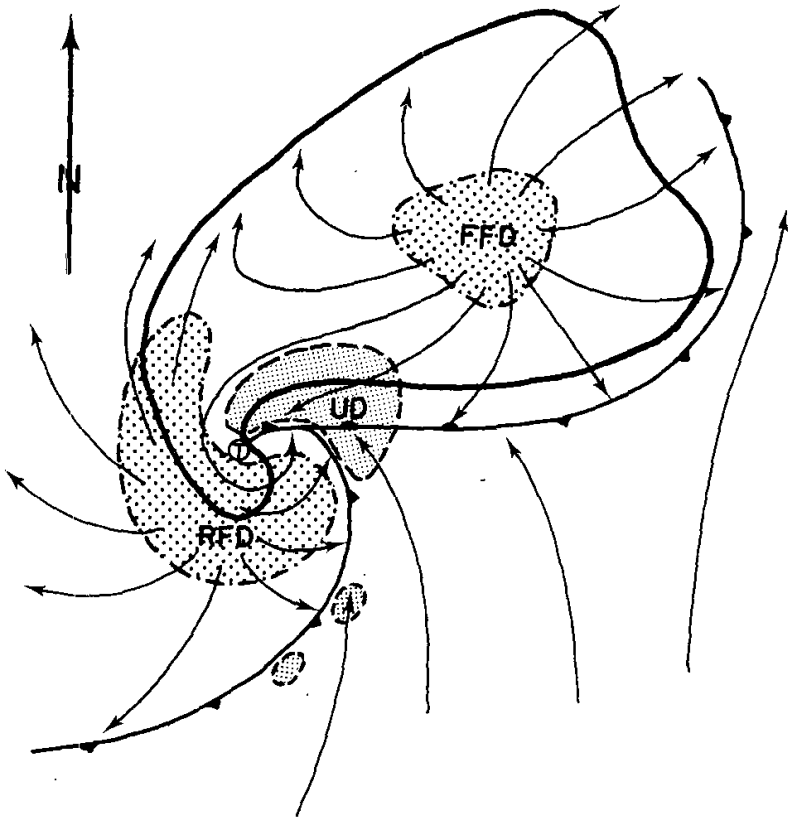

Fig. 2.3. Schematic plan view of the surface features in a supercell thunderstorm. Included features are the rear-flank downdraft (RFD), forward flank downdraft (FFD), gusts fronts, the main updraft (UP), and the location of the tornado (T). Reproduced from Lemon and Doswell (1979).

2.2.2 Numerical simulations and the modern era of tornadic storm research

Increasing computational power and the consequential development of three-dimensional numerical simulations of idealized supercells set the stage to explain the development of many of the features described by LD79 and earlier studies. Schlesinger (1975) presented one of the earliest three-dimensional simulations of deep convective clouds in vertical wind shear and while his model did not produce storms

that closely resembled supercells; he was able to tentatively conclude that tilting of environmental vorticity may be responsible for the development of mesoscale rotation. Schlesinger (1975) also suggested that horizontal pressure forces associated with rotation may steer the convective cloud at an appreciable angle to right or left of the mean wind.

A few years after Schlesinger's study, Wilhelmson and Klemp (1978) and Klemp and Wilhelmson (1978a, b) used a non-hydrostatic numerical model to generate the first simulations of supercells that closely resembled observations. Storm-splitting and propagation to the right or left of the mean wind were successfully simulated in their studies. Wilhelmson and Klemp (1978) and Klemp and Wilhelmson (1978a) showed that storm-splitting was the result of water loading splitting an initial storm that developed in wind shear. Klemp and Wilhelmson (1978b) explained that the cyclonic or anti-cyclonic split would be favored depending on the curvature of the hodograph owing to a relative enhancement of gust front convergence beneath the storm. This enhanced convergence also was responsible for propagation to right or left of the mean flow. For unidirectional shear, mirror image storms were created.

By linearizing the vertical vorticity equation, Rotunno (1981) confirmed that mid-level rotation in supercells was the result of tilting of environmental vorticity just as Barnes (1968) had proposed. However, the key insight of Rotunno's work was that tilting of vorticity resulted in a mid-level vortex couplet as vortex tubes were tilted upward/downward on the periphery of a developing updraft. This partially explained the tendency for counter-rotating supercells that were frequently observed.

While storm-splitting and propagation away from the mean flow had been successfully modeled, the dynamics behind the effects remained only partially explained until Rotunno and Klemp (1982; hereafter RK82). Noting that Schlesinger (1980) had discovered the importance of an upward vertical pressure gradient force on storm-splitting, RK82 first presented a linear analysis of the vertical component of the equation of motion to explain the impact of an updraft in the presence of shear on the pressure field. A summary of their analysis follows.

RK82 Begins with the shallow, inviscid, anelastic equations of motion,

$$\frac{\partial \boldsymbol{v}}{\partial t} + \mathbf{v} \cdot \boldsymbol{\nabla}\mathbf{v} = -\boldsymbol{\nabla}\pi + \mathbf{B}\mathbf{k} \ , \tag{2.1}$$

$$\frac{dB}{dt} + \mathbf{v} \cdot \boldsymbol{\nabla}\mathbf{B} = -N^2 \, w \ , \tag{2.2}$$

$$\boldsymbol{\nabla} \cdot \mathbf{v} = 0 \ , \tag{2.3}$$

where $\mathbf{v}$ and $\boldsymbol{B}$ are the velocity and buoyancy vectors respectively; $\pi = C_p \theta_o (\frac{p}{p_o})^{\frac{R}{C_p}}$, where p, p_o, θ_o, R, and C_p are the pressure, ground pressure, potential temperature at the ground, universal gas constant and specific heat at constant pressure, respectively and N is the Brunt-Vaisala frequency. RK82 then linearized (2.1)-(2.3) about the environmental wind vector, $\boldsymbol{V} = [U(z), V(z), 0]$, to obtain

$$\frac{D}{Dt}\mathbf{v}' + w' \frac{d}{dz}\boldsymbol{V} = -\boldsymbol{\nabla}\pi' + \boldsymbol{B}'\mathbf{k}, \tag{2.4}$$

$$\frac{D}{Dt}\mathbf{B}' = -N^2 w', \tag{2.5}$$

$$\boldsymbol{\nabla} \cdot \mathbf{v}' = 0, \tag{2.6}$$

Where the total derivative is $\frac{D}{Dt} = \frac{\partial}{\partial t} + \boldsymbol{V} \cdot \boldsymbol{\nabla}$. Assuming a horizontally homogeneous environment, keeping in mind the definition of the total derivative, and taking the divergence of (2.4) an equation for π' can be obtained as

$$\nabla^2\pi' = -2\frac{d\boldsymbol{V}}{dz}\cdot\boldsymbol{\nabla}w'. \quad (2.7)$$

By approximating that the Laplacian of a function is negatively proportional to the function itself, the expression

$$\pi' \sim \frac{d\boldsymbol{V}}{dz}\cdot\boldsymbol{\nabla}w' \quad (2.8)$$

can be obtained. This expression implies that the linear effect of an updraft in vertical wind shear is, at any given level, for there to be a high pressure perturbation upshear and a low pressure perturbation down shear of the updraft. RK82 then explained that for a curved hodograph, where the shear vector rotated cyclonically with height, this linear effect would lead to an upward pointing vertical pressure gradient force on the right flank and a downward pointing pressure gradient on the left flank of a storm. This configuration (Fig. 2.4) favors the enhancement of a developing right-moving supercell. RK82 found that after the early development stages of the storm, non-linear effects begin to become important and can cause storm-splitting even when rain processes are turned off in the model. They conclude that storm-splitting is likely caused by a combination of rainwater loading [as suggested in Wilhelmson and Klemp (1978a)] and the non-linear effects of rotation on the vertical pressure field. These non-linear effects imply that even in unidirectional shear, updrafts will tend to be favored on the flanks of convective cells and storms will tend to split and move with a component different from the mean flow. A final important aspect of RK82 is the argument they made against the obstacle flow analogy that was used [e.g., by Fujita and Grandoso (1968) in implying the importance of the Magnus effect] to describe supercells. RK82 pointed out that a supercell's updraft is highly porous and the comparison between the updraft and a

cylinder is greatly complicated by the fact that the updraft and shear vector orientation typically change with height.

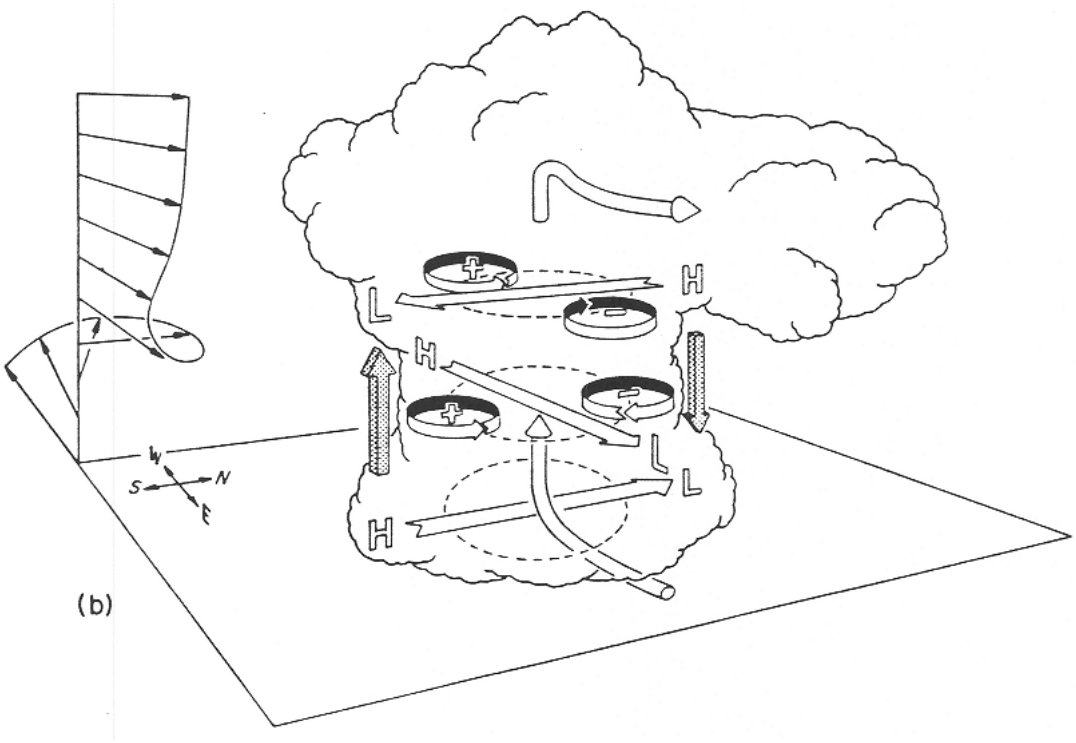

Fig. 2.4. Schematic of the tendency for updraft (downdraft) to be favored on the right (left) flank of a convective updraft in cyclonic vertical wind shear. Reproduced from Klemp (1987).

Using the same model as RK82, Klemp and Rotunno (1983; hereafter KR83) nested a high-resolution domain with 250-m horizontal grid-spacing within a lower resolution simulation of the 20 May 1977 Del City Oklahoma supercell that had been performed by Klemp et al. (1981). The high-resolution simulation reproduced the intensification of a low-level vortex, and also featured the development of a strong downdraft near the low-level vortex which KR83 named the 'occlusion' downdraft. The occlusion downdraft was found to be the result of the intensification of low-level rotation leading to a downward directed pressure gradient force. Based on a streamline analysis, KR83 concluded that the low-level vertical vorticity comprising the low-level

circulation had its origins as a combination of environmental horizontal vorticity associated with vertical wind shear and, more importantly, was baroclinically generated predominantly along the horizontal buoyancy gradients associated with the storm's cold pool. The convergence of streamlines into the low-level circulation implied that after some tilting of this horizontal vorticity, vertical vorticity was dramatically amplified via stretching.

The 20 May 1977 supercell was also studied observationally via a dual-Doppler analysis in Brandes (1981). Brandes (1981) concluded that stretching of vorticity, as a result of the collocation between the tornado and a strong low-level updraft, was critical to tornadogenesis. This interpretation differed significantly from LD79 because it implies a bottom-up rather than top-down series of events leading to tornadogenesis. KR83 confirmed Brandes' conclusion.

Many of the conclusions reached by RK82 were rigorously proven in Davies-Jones (1984). Using a linear theory of dry, shallow, inviscid, isentropic, convectively unstable flow in vertical wind shear, Davies-Jones (1984) showed a positive correlation between vertical velocity and vertical vorticity. The introduction of the concept of streamwise vorticity helped to clarify this finding. Davies-Jones defined streamwise vorticity as the portion of the horizontal vorticity vector parallel to the storm-relative wind. He explained that vorticity with a streamwise component implied that the maximum in vertical velocity and vertical vorticity would be located on the same side of an isentropic hump (Fig. 2.5). For purely crosswise vorticity, there is no correlation between the vertical velocity and vertical vorticity associated with an isentropic peak. Davies-Jones (1984) concludes with a discussion of the importance, especially for

forecasters, of recognizing areas of large storm-relative streamwise vorticity as these storms will most likely be the most severe with the greatest likelihood of tornadoes.

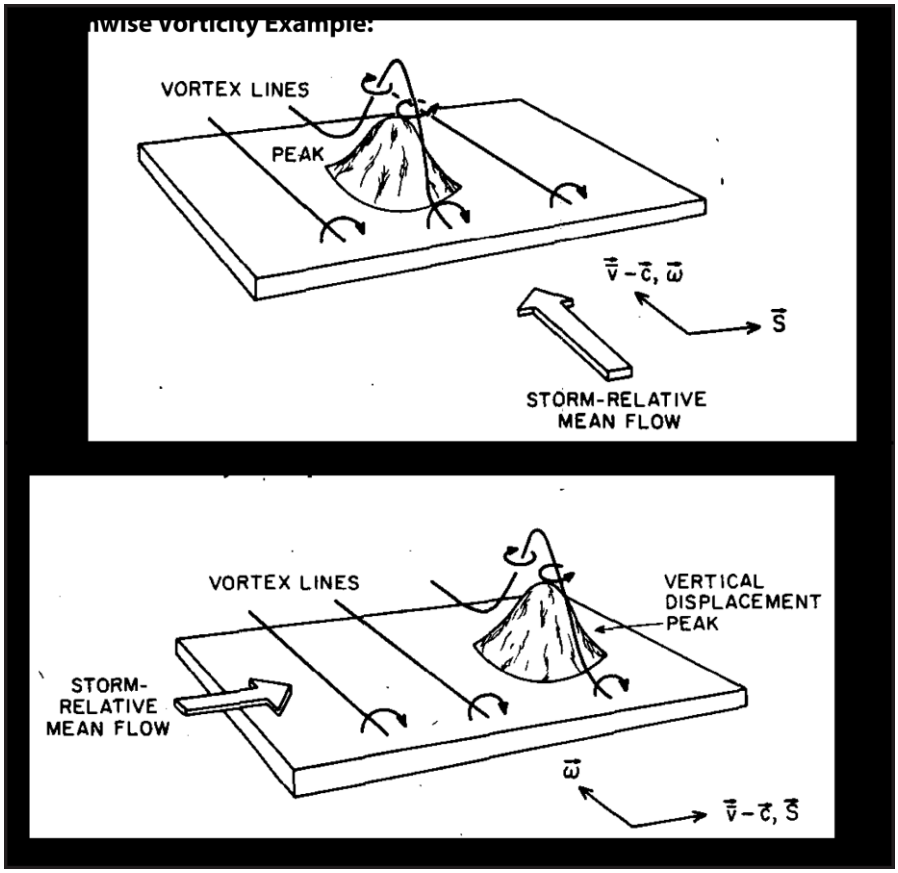

Fig. 2.5. Conceptual example of the difference between a crosswise and streamwise vorticity when flow is forced to rise over an isentropic 'hump'. In the streamwise example, the resulting vertical vorticity is positively correlated with the updraft. In the crosswise example, there is no correlation between vertical vorticity and the updraft. Reproduced from Davies-Jones (1984).

The final significant contribution in the area of supercell dynamics from Rotunno and Klemp came in their 1985 paper "On the Rotation and Propagation of Simulated Supercell Thunderstorms". Rotunno and Klemp (1985) looked further at storm propagation and low-level rotation using, for the first time, the conservation of equivalent potential vorticity and Bjerknes first circulation theorem. The conservation of equivalent potential vorticity is mainly used to explain that vortex lines along

isentropic surfaces will remain on these surfaces and as such tilt upward with the updraft. This explanation is very similar to the theoretical work done in Davies-Jones (1984).

Perhaps the more significant contribution of Rotunno and Klemp (1985) was their use of Bjerknes' first circulation theorem to find the origin of low-level rotation in their simulated supercell. By calculating backward trajectories for a ring of parcels initially (in backward time) surrounding the low-level vortex, Rotunno and Klemp were able to approximate the circulation around the material closed curve made up by the ring of parcels. Circulation C(t) is defined as

$$C(t) = \oint \mathbf{v} \cdot \boldsymbol{dl} \tag{2.9}$$

where $\mathbf{v} \cdot \boldsymbol{dl}$ is the portion of the velocity vector tangential to the curve at a given point. Bjerknes' first circulation theorem for the inviscid Boussinesq approximation states that circulation can only change as a function of buoyancy, i.e.,

$$\frac{dC}{dt} = \oint B\boldsymbol{k} \cdot \boldsymbol{dl} = \oint B dz. \tag{2.10}$$

By evaluating (2.9) and (2.10) around the ring of parcels, Rotunno and Klemp (1985) showed that as the parcels converged toward the low-level vortex, the circulation, which began negative, became large and positive as a result of the generation due to buoyancy. Most of the circulation was generated in the part of the circuit that passed through the forward flank of the supercell suggesting that baroclinic vorticity generated in this region is critical for developing low-level rotation. Another important implication to this finding is it indicates that there is not a direct relationship between the mid-level and low-level mesocyclones. The relationship is indirect and relates to the way in which the mid-level mesocyclone impacts the location of the cold pool which leads to a

favorable configuration for baroclinic generation of horizontal vorticity. This horizontal vorticity is then tilted into the vertical and stretched to generate the low-level mesocyclone. Re-running the simulation with rain processes turned off still generated a mid-level mesocyclone but lacked a low-level mesocyclone. These dry simulations also verified the result from RK82 that storm propagation is a result of pressure forces associated with vertical wind shear and thunderstorm rotation. It is also important to note that Rotunno and Klemp (1985) verified the radar-based observational evidence in Brandes (1984) that the RFD does not directly lead to the generation of low-level circulations. Brandes (1984) does suggest though that the RFD leads to enhanced surface convergence that can assist with amplification of vertical vorticity generated through tilting of inflow horizontal vorticity.

Verification of the conclusions of the numerical simulations presented above would require detailed observations not just from radar but also from in-situ probes in order to investigate the thermodynamic properties of the thunderstorm outflow. These observations would not be available until the Verification of the Origins of Rotation in Tornadoes experiment (VORTEX) conducted in 1994 and 1995. Results from VORTEX will be discussed later. In the meantime, researchers refined the existing theories of supercell dynamics with a focus on distinguishing supercell environments and, perhaps more importantly, tornadic supercell environments.

One of the principal ideas developed during this time period was of the importance of helicity (defined as the dot product between the velocity and vorticity vectors) to supercells. Lilly (1986) was the first to apply helicity to supercells, finding that helical flows were more stable than non-helical flows with regard to energy losses

due to turbulent dissipation. More importantly, Lilly stated that the optimal configuration to take advantage of this helical effect was for the updraft and vorticity center to be collocated with motion lateral to the mean flow. In my view, this conclusion is nearly identical to that shown in the schematic of Davies-Jones (1984); presented above in Fig. 2.5. The difference is likely mainly that of semantics given the close association between streamwise vorticity and helicity [i.e., helicity as defined in Lilly (1986) is essentially the same quantity as streamwise vorticity as defined in Davies-Jones (1984)].

Davies-Jones (1990) unified the concepts of streamwise vorticity and helicity with the introduction of storm-relative (s-r) helicity, H, which he defined as

$$H(\boldsymbol{c}) = -\int_0^h \mathbf{k} \cdot (\boldsymbol{V} - \boldsymbol{c}) \times \frac{\partial \boldsymbol{V}}{\partial z} dz \qquad (2.11)$$

where $\boldsymbol{c}$ is storm motion, $\boldsymbol{V}$ is the environmental wind, and h is an assumed inflow depth. Davies-Jones (1990) found that h of 3-km was useful as a tornado forecasting tool. He also explained that owing to large temporal and spatial variability, the use of s-r helicity could be difficult for operational forecasters. A simulation by Brooks et al. (1993) shows that a storm with large s-r helicity, but weak storm relative surface winds, does not develop a strong, persistent low-level mesocyclone as the storm's gust front rapidly cuts off low-level inflow to the storms updraft. This led to them to conclude the storm-relative inflow wind strength plays a critical role in storm evolution.

In a companion paper to Brooks et al. (1993), Davies-Jones and Brooks (1993) examined low-level mesocyclone formation from a theoretical perspective. They explained that tilting and subsequent stretching of low-level vorticity could only be effective if cyclonic vertical vorticity was already in existence near the surface.

However, in the absence of pre-existing vertical vorticity external to the storm, the only way it would be possible to have vertical vorticity next to the surface would be for it to be generated in a downdraft because if vertical vorticity were tilted and then stretched by an updraft, significant vertical vorticity would only become present far above the ground. The complicating factor, however, was the fact that for air that entered the downdraft with streamwise vorticity, the resulting vertical vorticity generated would be negative in a barotropic flow because vortex lines are frozen in the fluid for barotropic flows. Davies-Jones and Brooks (1993) then explained that baroclinity, which causes continuous southerly pointed horizontal vorticity generation, introduces "slippage" between the vortex and streamlines, with the vortex lines pointing toward higher streamlines. As a result of the frozen vortex lines effect, when the air begins starts to turn horizontal again this orientation of the vortex lines relative to the streamlines is maintained and positive vertical vorticity is generated near the ground. This vertical vorticity and is then stretched as is enters the storm's updraft. This process is shown schematically in Fig. 2.6.

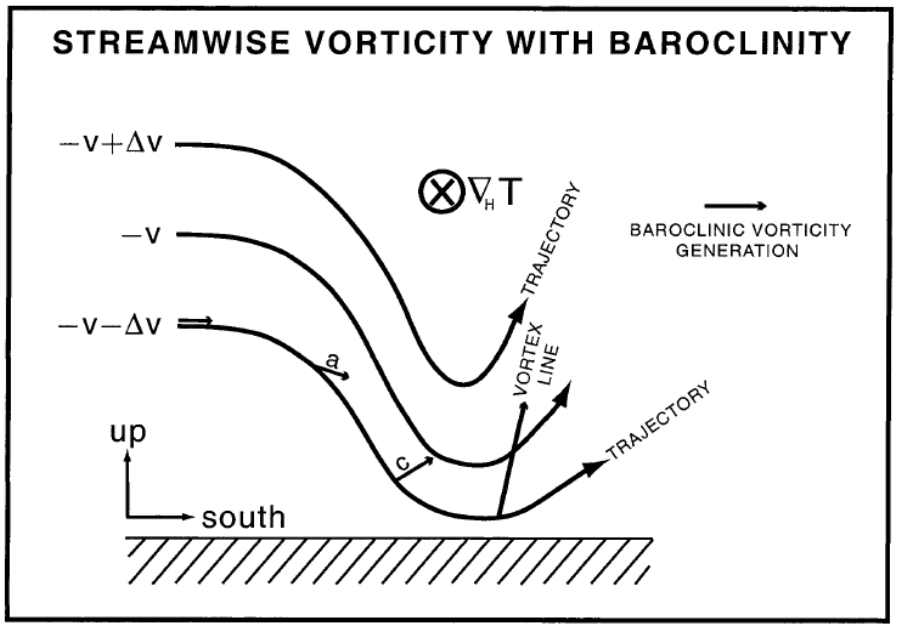

Fig. 2.6. Conceptual model describing the way in which vertical vorticity can be generated at the surface by baroclinity in a downdraft. Reproduced from Davies-Jones and Brooks (1993).

It is interesting to note that Davies-Jones (1990) does not reconcile physically why s-r helicity is important in the generation of tornadoes. Based on Davies-Jones (1984; 1990) and Lilly (1986) it clearly follows that high s-r helicity would lead to a strong mid-level mesocyclone, but as shown by Rotunno and Klemp (1985; amongst many others) this does not necessarily directly influence the low-level mesocyclone which is created by baroclinic processes. There is no explanation provided as to why strong helical storm-relative environmental flow should influence the vorticity production at low-levels. This mismatch in theory and applications will be discussed further in the summary and discussion section of this chapter.

The next significant contribution to supercell research came from the high-resolution numerical simulations presented in Wicker and Wilhelmson (1995; hereafter WW95). The simulation discussed in WW95 was similar to that performed by KR83

except the integration was performed for a much longer period with substantially higher resolution, especially in the vertical (dzmin of 50 m as opposed to 500 m in KR83). The WW95 simulation produced two tornado-strength vortices, both of which were preceded by intensification of the lower to mid-level updraft. These updraft intensifications led to the intensification of the low-level mesocyclone which in turn dynamically forced a low-level updraft leading to tornadogenesis. WW95 does not explain the cause of the mid-level updraft surges responsible for low-level mesocyclone intensification. Trajectory analyses presented in WW95 indicate that vorticity generated baroclinically along the forward flank gust front was critical in the generation of both the low-level mesocyclone and tornado. This result agrees well with the findings of Klemp and Rotunno (1985) and Davies-Jones and Brooks (1993). However, WW95 were unable to find trajectories that behaved in the manner shown in the schematic in Davies-Jones and Brooks (1993), as all parcels that descended in the RFD in their simulation had negative vertical vorticity. WW95 also explained that the intensification of the low and mid-level mesocyclone preceding tornadogenesis was possibly the simulated version of the descending TVS signature. They felt this finding helped to reconcile differences between bottom-up theories of tornadogenesis and observations of the descending TVS.

As mentioned earlier, the VORTEX (Rasmussen et al. 1994) was designed to answer some of the outstanding questions and verify results garnered from earlier theoretical, observational, and modeling studies. In the spring of 1994 and 1995, VORTEX surrounded storms with a variety of instruments including mobile mesonets (Straka et al. 1996), the Oklahoma Mesonet (Brock et al. 1995), ground based mobile

Doppler radars (e.g., Bluestein et al. 1993), airborne Doppler radars (e.g., Wakimoto et al. 1996), mobile sounding systems (Rust et al. 1990), atmospheric profilers, photogrammetric teams, and ground based instrument packages called 'turtles' (Brock et al. 1987).

Most of the early studies that were performed utilizing VORTEX data were detailed case studies (Wakimoto and Atkins 1996; Bluestein et al. 1997b; Bluestein et al. 1997a; Wakimoto and Liu 1998; Wakimoto et al. 1998). Wakimoto and Atkins (1996) is of particular interest because it documented the formation of an F3 tornado that formed along the flanking line of a supercell on 29 May 1994. This was the first documented instance of a strong tornado forming in such a manner and, given the lack of an associated mid-level mesocyclone, was clearly an instance of a tornado forming from the ground up. Interestingly, it is uncertain how rare such tornadoes really are as Wakimoto and Atkins (1996) point out that it likely would not have been recognized that the tornado formed in such a manner had it not been observed by the VORTEX field team as WSR-88D observations were barely capable of resolving the small cell that the tornado developed in association with. In fact, WSR-88D observations alone may have led researchers to believe the tornado formed in association with the already well-formed supercell. Very high-resolution Doppler radar observations from a different storm presented in Bluestein et al (1997b) also found small-scale vortices along the rear-flank gust front, in a similar area to the location that the tornado studied in Wakimoto and Atkins (1996) originated.

Another significant study resulting from VORTEX was presented by Wakimoto et al. (1998), in which high-resolution dual-Doppler analyses were used to generate a

thermodynamic retrieval with high enough resolution to determine the origin of the occlusion downdraft. This retrieval confirmed that the occlusion downdraft was the result of a strong downward-pointing vertical pressure gradient force associated with the strong rotation of the low-level mesocyclone. This was the first observational study with sufficient resolution to confirm the conclusions about the occlusion downdraft origins based on numerical simulations (e.g., KR83).

VORTEX also yielded some unexpected results, one of which was the surprising lack of distinguishable differences in the kinematic fields of tornadic and non-tornadic supercells. Trapp (1999) presented observations from six supercells, three of which were tornadic. These observations showed that both the tornadic and non-tornadic storms contained persistent low-level mesocyclones, suggesting that the physical mechanisms explaining the genesis of low-level mesocyclones are not the same as those responsible for tornadogenesis. Trapp (1999) did note that the non-tornadic mesocyclones were larger with weaker vortex stretching than tornadic mesocyclones. In agreement with Trapp (1999), Wakimoto and Cai (2000) compared observations from a tornadic and non-tornadic supercell and found very similar structures for the two storms, with virtually identical low-level mesocyclones. The only differences between the two storms were stronger updrafts along the rear-flank gust front, stronger storm-relative inflow, and more precipitation behind the RFGF for the non-tornadic storm. Given the sample size of only two storms, it is impossible to determine whether these differences had any bearing on tornado potential or whether they are simply coincidental.

Perhaps even more surprising than the similarities between tornadic and non-tornadic supercells were the thermodynamic observations presented by Markowski et al (2002; hereafter MSR2002). Using observations collected by the mobile mesonets from 30 different hook echoes of between 1994 and 1999, MSR2002 found that strongly tornadic supercells had significantly warmer RFDs than non-tornadic or weakly tornadic supercells. Additionally, all RFDs in tornadic storms contained surface-based CAPE and substantially less CIN than non-tornadic supercells. In the most prolific tornado producing storms there was little or no baroclinic generation of vorticity in the RFD. This result is somewhat contradictory to the explanation of the generation of positive vertical vorticity in a downdraft proposed by Davies-Jones and Brooks (1993). MSR2002 also found that [as in Wakimoto and Cai (2000)] the gust front and low-level kinematic structure was often indistinguishable between tornadic and non-tornadic supercells.

In attempt to explain the results of MSR2002, Markowski et al. (2003a) performed highly idealized axisymmetric simulations of the interaction between updrafts and surrounding downdrafts. The simulations were designed so that the downdraft would transport angular momentum from the rotating updraft to the surface. This air then converged into the updraft and a tornado was generated. Simulations in which the downdraft was warmer (i.e., those with large low-level relative humidity or a lower concentration of precipitation particles) generated stronger, longer-lived tornadoes. This result led Markowski et al. (2003a) to conclude that a similar process may be occurring in supercells, whereby supercells with warmer RFDs were able to more effectively concentrate circulation-rich downdraft air, leading to tornadogenesis.

Shabbott and Markowski (2006) examined mobile mesonet observations from the FFD region for a subset of the cases examined in MSR2002. Interestingly, they found similar results to MSR2002, namely, that the FFD was warmer for tornadic supercells than for non-tornadic supercells. The results of Shabbott and Markowski (2006) confirm that the relationship between the low-level mesocyclone and tornado is much less clear than was suggested in earlier studies. In fact, non-tornadic supercells had stronger baroclinic generation of horizontal vorticity in the FFD suggesting that stronger low-level mesocyclones might be expected if this baroclinic vorticity is really the source of vorticity for low-level rotation in supercells [e.g., as suggested in Klemp and Rotunno (1985)]. However, the increased cold air in the forward flank may tend to undercut the inflow to the storm (e.g, Brooks et al. 1994) implying that the relationship between baroclinic generation and mesocyclone strength and persistence is not as straightforward as it may seem. Polarimetric radar observations of the Z_{DR} arc (a signature aligned along the forward flank gust front of supercells occurring as a result of size sorting of precipitation particles in wind shear) from Kumjian and Rhzykov (2008, 2009) indicate that the disruption of the arc may indicate updraft undercutting. This disruption occurs more frequently in non-tornadic supercells than tornadic supercells. As an aside, because the Z_{DR} arc marks an area where mainly large drops are present, it may also be an important indication of the thermodynamic characteristics of the FFD. Because the evaporation of large drops results in less evaporative cooling than that of small drops (Rogers and Yau 1989), the local effect may be to create a less well-defined baroclinic zone along the FFGF. A similar point about the impact of large drops is made by Romine et al. (2008).

In recent years, vortex line analysis has become a popular diagnostic tool for the examination of supercell tornadogenesis (Straka et al. 2007; Markowski et al. 2008; Markowski et al. 2011; Markowski 2012a, b; Marquis et al. 2012). Straka et al. (2007) was the first to propose examining vortex lines to explain previous observations of vortex couplets straddling the supercell hook echo (e.g., Table 1 in Straka et al. 2007). They found that a vortex line 'arch' connected the counter-rotating vortices and proposed a mechanism by which a baroclinically-generated vortex ring in a downdraft was later arched upward by the low-level updraft along the RFGF. Markowski et al. (2008) applied vortex line analysis to six observed supercell thunderstorms (three tornadic and three non-tornadic) and found vortex arches between the vortex couplets in all six cases. The prevalence of vortex arches in supercells led Markowski et al. (2008) to speculate about whether their existence was a ubiquitous trait of supercells. Moreover, Markowski et al. (2008) explained the presence of vortex arches strongly argued the low-level vorticity (e.g., for low-level mesocyclones and tornadoes) was generated along the RFGF rather than along the FFGF. This generation mechanism is quite different than that suggested in the modeling studies presented earlier (e.g., Klemp and Rotunno 1985).

While Markowski et al. (2008) references that the generation of low-level vertical vorticity for the vortex arches is similar to that proposed in Davies-Jones and Brooks (1993), in my view there are some serious differences. The schematic of Davies-Jones and Brooks (1993) showed how baroclinically generated streamwise vorticity in a downdraft could lead to the generation of positive vertical vorticity at the ground. In Markowski et al. (2008), the schematic (Fig. 2.7) indicates that the vortex

couplet is generated by an updraft tilting crosswise vorticity rather than streamwise vorticity. This difference implies that in order for positive vertical vorticity to exist at the ground [e.g., the vortex lines intersect the ground in many of the figures of Markowski et al (2008)] the vortex line must be 'snapped' during or after the arching process. Markowski et al. (2008) does not mention this and does not explain how such a phenomenon might occur. Thus, in my view, the vortex arches can explain the genesis of counter-rotating low-level mesocyclones but fall short of explaining how that rotation can be brought to the surface. It also should be noted that presence of an arch structure implies a significant horizontal gradient of vertical velocity, with the maximum updraft at the center of the arch, suggesting that the portion of the vortex line that becomes vertically oriented would (at least initially) not be in an area of strong stretching of vorticity. It is possible, however, that dynamically induced updrafts owing to the generation of rotation at low-levels could re-orient the updraft structure.

A recent study by Markowski et al. (2012a,b) has documented in detail the development of low-level rotation and tornadogenesis in a supercell observed during the Second Verification of the Origins of Rotation in Tornadoes Experiment (VORTEX II; Wurman et al. 2012). Markowski et al (2012a) found vortex arches connecting a vortex couplet that straddled the RFD, which they took to indicate to the importance of baroclinic vorticity generated in the RFD in the generation of low-level rotation. However, the circulation analysis presented in Markowski et al (2012b) indicates that much of the circulation of the low-level mesocyclone is generated in the FFD. Markowski et al. (2012b) tries to reconcile this contradiction by stating "perhaps distinguishing between RFDs and FFDs is no longer fruitful, given that the RFD and the

FFD are typically within one large contiguous region of downdraft." It is my opinion that the lack of agreement between these two views of the origin of low-level rotation is symptomatic of the absence of a complete dynamical understanding of supercells, and genesis of low-level mesocyclones and tornadoes. Further complicating matters, Markowski et al. (2012b) was unable to rule out the possibility that surface friction was playing a role in the development of the low-level mesocyclone.

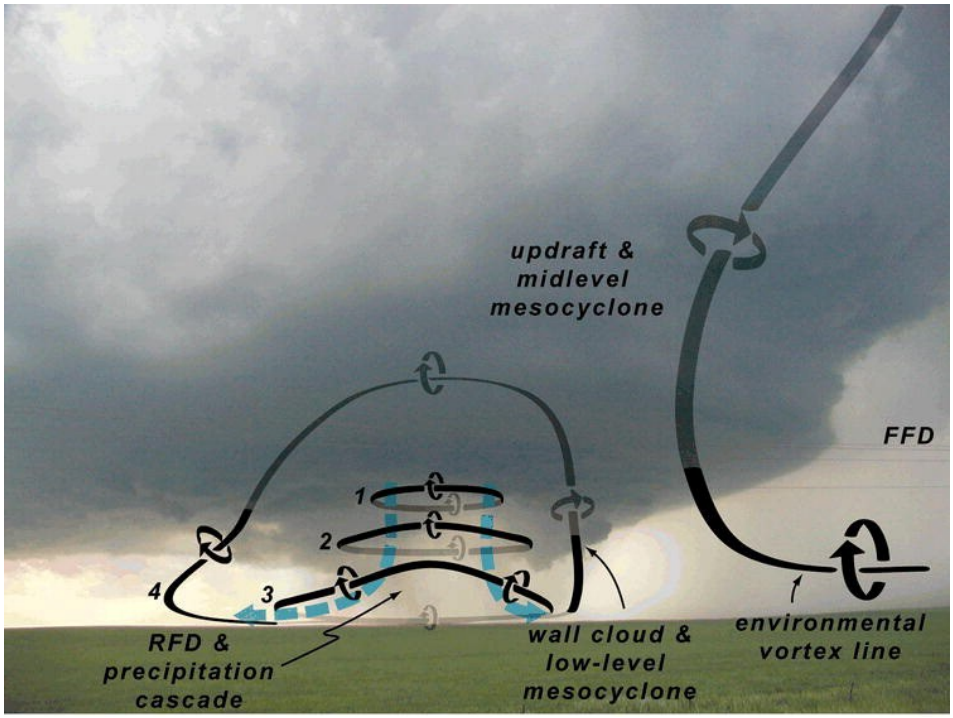

Fig. 2.7. Photo of a supercell overlaid with the idealized evolution of vortex lines in the RFD. Reproduced from Markowski et al. (2008)

The most recent significant finding in tornadic storm research has been the discovery of the presence (and importance) of internal secondary outflow surges behind the RFD[2] made by high-resolution observational studies (Wurman et al. 2007; Marquis et al. 2008; Wurman et al. 2010; Lee et al. 2011; Skinner et al. 2011; Kosiba et al. 2012; Lee et al. 2012; Marquis et al. 2012). Using high-resolution dual-Doppler and storm-

[2] These surges were first noted in the numerical simulations of Adlerman (2003) .

scale ensemble Kalman Filter (EnKF; Evensen 1994) analyses, Marquis et al. (2012) concluded that secondary RFD surges were important for tornadogenesis and maintenance when the tornado was not connected to primary RFGF. The reliability of the EnKF analysis presented is somewhat questionable as dual-Doppler analyses indicate vortex arches present over the secondary RFD surges, suggesting the surges were relatively colder than the main RFD. Meanwhile, the EnKF analysis indicates relatively warm air associated with the surges.

Mobile mesonet data presented in Lee et al. (2012) also indicate that internal surges were important for tornadogenesis and maintenance. In particular, one internal surge was coincident with tornadogenesis as it encountered a pre-existing vortex, while vertical vorticity along a subsequent internal surge appeared to play a direct role in intensifying and sustaining a later, more intense, tornado.

Mashiko et al. (2009) indicated that secondary RFD surges were critical to tornadogenesis in their high-resolution numerical simulations of a mini-supercell associated with a landfalling typhoon. They explain that, in addition to enhancing convergence, the secondary RFD surge provides an additional source of vorticity by transporting large streamwise vorticity, associated with the extreme low-level shear in the typhoon environment, into the inflow of the developing tornado. By conducting sensitivity experiments in which they turned off water loading or evaporation, they concluded that the secondary RFD surges in their simulation were the result of water loading. A tornado did not form in experiments where water loading is turned off.

While the results presented in Mashiko et al. (2009) are compelling for the tropical mini-supercell, it is unknown how applicable the study is to the more typical

supercell environment which is much drier with less low-level environmental helicity. Simplified numerical simulations presented in Davies-Jones (2008) suggest that a descending rain curtain can transport high angular momentum air from aloft and lead to tornadogenesis. However, this process differs somewhat from that presented in Mashiko et al. (2009) because in Davies-Jones (2008) the descending rain curtain brings angular momentum to the surface from the mid-level mesocyclone rather than from environmental streamwise vorticity. Davies-Jones (2008) explains that this barotropic process may be a way of explaining the lack of low-level baroclinity in tornadic supercells (e.g., MSR2002).

2.2.3 Summary and discussion

It is evident from the previous two sections that despite great advances in understanding the dynamics of supercells and tornadoes, there remain a number of existing questions and uncertainties. This subsection summarizes what we know, what we think we know, and what is still uncertain.

1) The mid-level mesocyclone: It is nearly certain that the mid-level mesocyclone is the result of tilting and subsequent stretching of environmental vorticity associated with vertical wind shear. Streamwise vorticity has been shown to be important in this process because of the implied correlation between the updraft and vertical vorticity.
2) Storm splitting and motion: It is well agreed upon that storm splitting is the result of a combination of water loading and dynamic pressure perturbations resulting from a rotating updraft in vertical shear. The effect of these dynamic

pressure perturbations combined with the mean wind are used to explain and estimate (e.g., Bunkers et al. 2000) supercell motion.

3) Low-level rotation: The origin of low-level rotation is much more uncertain than mid-level rotation. Early studies found temperature gradients along the FFGF played an important role. Observational studies did not confirm this result, showing that, especially in tornadic storms, thermal gradients along the FFGF were weak (Shabbot and Markowksi 2006). More recently, vortex line analyses suggest that baroclinically generated vorticity in the RFD plays an important role in low-level rotation. However, because vortex line analyses are only a diagnostic tool it is difficult to establish strong causal relationships. Other effects have been proposed to explain low-level rotation such as baroclinic vorticity owing to anvil shading (Dowell and Bluestein 1997; Markowski et al. 1998a; Markowski et al. 1998b) and pre-existing boundaries (Markowski et al. 1998a; Rasmussen et al. 2000). However, pre-existing boundaries are not always present and anvil shading has been shown in simulations by Frame and Markowski (2010) to generate little baroclinic vorticity. It should be noted, however, that one potentially important finding of Frame and Markowski (2010) was the generation of low-level horizontal vorticity owing to the impact of surface friction on the stabilized anvil shaded areas. Markowski et al. (2012b) could not rule out that frictionally generated vorticity in this same area was responsible for the generation of circulation around a circuit enclosing the low-level mesocyclone they studied. Indeed, frictionally-generated vorticity is found

to be of great importance to tornadogenesis in the numerical simulations presented in chapters 3 and 4 of this dissertation.

4) Tornadoes and low-level storm-relative helicity: An operationally useful, but physically unexplained, correlation has been shown between the occurrence of tornadoes (particularly for strong tornadoes) and large values of low-level (e.g, 0-1km) storm-relative helicity (Kerr and Darkow 1996; Rasmussen and Blanchard 1998; Markowski et al. 2003b; Rasmussen 2003; Thompson et al. 2007). While this relationship has proven beneficial for forecasting applications, a satisfactory explanation of the physical relationship between this parameter and tornado potential remains elusive, especially given that storm-generated vorticity is currently the primary suspect for the origin of low-level rotation in supercells. As mentioned above, Mashiko et al. (2009) did find that environmental streamwise vorticity directly enhanced the tornado in their simulation. However, this result may be highly case dependent.

5) Internal outflow RFD surges: As discussed at the end of the previous section, advances in observational platforms have led to increasing recognition of the presence, and importance, of secondary RFD surges in tornadic supercells. However, the origin and ubiquity of such surges is unknown. It is also not known if secondary RFD surges are found exclusively in tornadic supercells. Further complicating the issue, there are examples of tornadoes occurring in supercells that do not appear to have secondary RFD surges (e.g., Marquis et al. 2012).

6) Thermodynamic characteristics of RFDs: Over the past ten years there has been a growing body of evidence that tornadic and non-tornadic supercells possess different thermodynamic characteristics, with generally warmer RFDs in tornadic supercells (MSR2002; Grzych et al. 2007; Lee et al. 2011; Lee et al. 2012). Reasons for this discrepancy are somewhat speculative, but the tendency of warm RFDs to be associated with tornadoes is generally attributed to the storm being capable of lifting and converging less negatively buoyant air with greater ease than more negatively buoyant air. In the recent study by Lee et al. (2012), 2.5 hours of mobile mesonet observations from a strongly tornadic supercell show a large degree of heterogeneity in the RFD. Though the RFD outflow is typically warmer in close proximity to the tornado, areas farther from the tornado are occasionally fairly cold. In addition, multiple RFD internal surges are observed and found to possess a large variety thermodynamic properties, with some warmer and some notably colder than the larger-scale RFD. These results suggest that RFD outflow temperature may be more complicated and heterogeneous than originally thought (e.g., MSR2002).

In fact, an important (but perhaps underemphasized) finding in Lee et al. (2012) was the strong vertical gradient in equivalent potential temperature (θ_e) between from ~700 m – 2500 m AGL. Through this layer θ_e decreases by about 38 K. A similar vertical profile of θ_e was observed in Markowski (2002). This suggests that, if θ_e is approximately conserved, very small differences in parcel origin height will lead to large differences in the thermodynamic characteristics of the RFD. This could be the root cause of the large heterogeneity observed in

the RFD in Lee et al. (2012). Assuming that such a strong θ_e gradient is also present for non-tornadic supercells, determining why downdrafts in non-tornadic supercells come from slightly higher levels may aid in understanding the differences between tornadic and non-tornadic supercells. On the other hand, it is possible that the causal relationships have been interpreted incorrectly and the presence of warmer RFDs is simply the result of greater dynamical forcing (at low-levels) owing to large pressure deficits associated with the tornado and/or tornado cyclone at the surface in tornadic supercells. Unfortunately, if this is the case, it likely implies that the observations of relative warm RFDs in tornadic supercells will do little for enhancing our dynamical understanding of tornadogenesis in supercells.

7) The tornadic vortex signature (TVS): A paradoxical aspect of many early studies was the fact that although tornadoes appeared to be generated near the ground, Doppler radar data seemed to indicate that the TVS formed initially aloft and descended to the ground. Reconciliation of these contradictory observations was elusive for many years and most theories for tornadogenesis were unable to explain the presence of the descending TVS. Moreover, Trapp et al. (1999) found that about half of TVSs descended while the remainder formed near the ground and ascended. Very recently, high-temporal resolution observations from a phased-array mobile Doppler radar (Bluestein et al. 2010) may have reconciled the TVS issue (French 2012). More specifically, the descending TVS may be the result of insufficient temporal resolution of the observational platform, in this case the WSR-88D. When the same storm is sampled by both

high-temporal resolution phased-array mobile Doppler radar and the WSR-88D, the phased-array radar indicates an ascending TVS while the WSR-88D indicates the TVS is descending. A detailed explanation of this discrepancy is still a work in progress (M. French, personal communication), however, a descending TVS has never been observed by a mobile Doppler radar with high temporal resolution (Alexander 2010; French 2012).

2.3 Non-supercell tornadoes

For completeness, this chapter concludes with a brief review of non-supercell tornadoes. In general, non-supercell tornadoes can be separated into two categories, those that occur with quasi-linear convective system (QLCS) and those that are categorized as land/waterspouts.

2.3.1 Landspouts

Landspouts and waterspouts are likely the most well understood but may have the poorest predictability of all tornadoes (Markowski and Richardson 2009). Because there is some debate about the classification of a gustnado as a tornado (Agee and Jones 2009; Markowski and Dotzek 2010), the discussion here focuses on landspouts (with analogies to waterspouts).

Wakimoto and Wilson (1989, hereafter WW89) present the most in-depth observational study of the development of landspouts (hereafter, referred to as non-supercell tornadoes to maintain continuity with WW89 and more recent studies). In WW89, non-supercell tornadoes were studied as part of a field project called the Convective INitiation and Downburst Experiment (CINDE). WW89 presents data from 27 different non-supercell tornadoes that developed in the Colorado high plains during

summer 1987. By studying the properties and life-cycle of these non-supercell tornadoes, WW89 propose that such tornadoes initially develop as small vortices that are formed via the release of shearing instabilities along a convergence boundary [in the case of WW89, the Denver Convergence zone (e.g., Wilczak and Christian 1990)]. These small vortices then strengthen to tornado strength via stretching as they become collocated with developing deep moist convection. Brady and Szoke (1989) propose a similar development mechanism which they find to be similar to waterspout formation [presented by Golden (1971)].

Lee and Wilhelmson (1997a, b) investigated non-supercell tornadogenesis via numerical simulations. Using a dry, non-hydrostatic model, Lee and Wilhelmson (1997a) showed (in agreement with WW89) that small low-level vortices (hereafter, misocyclones) are the parent vortex of non-supercell tornadoes. Numerous misocyclones initially formed via shearing instability along a simulated outflow boundary in their study. With time, energy cascades upscale as a result of vortex coalescence and vorticity extrusion; a process by which a stronger vortex extracts vorticity from a weaker vortex. Lee and Wilhelmson (1997a) find that misocyclones act to enhance convergence along the outflow boundary, leading them speculate that misocyclones play a role in the initiation of deep moist convection. Preliminary results presented in Lee et al. (2000) confirm this speculation by showing deep moist convection develops first, and is most significant, in association with misocyclones.

Lee and Wilhelmson (1997b) extend the results of Lee and Wilhelmson (1997a) by using a non-hydrostatic numerical model that includes moist processes. This study proposed a six stage conceptual model of the non-supercell tornado lifecycle (Fig. 2.8)

and found that moist convection is critical for non-supercell tornadogenesis. In the first two stages of the Lee and Wilhelmson (1997b) conceptual model, a vortex sheet develops along wind-shift boundary that encounters an air mass with a component of the wind parallel to the boundary. Horizontal shearing instability then leads to the development of many misovortices. In stage III, the misovortices begin to merge and combine, with dominant misovortices extruding vorticity from smaller vortices and/or vortices of the same size coalescing. In the stage IV, deep moist convection forms in response to the low-level convergence pattern associated with the dominant misovortices. Non-supercell tornadogenesis also occurs during this stage in response to friction-induced radial inflow into the misovortices. During stage V, the non-supercell tornadoes reach their most intense phase as rain-induced downdrafts further enhance low-level convergence and vorticity stretching at low-levels. These rainy downdrafts lead to the dissipation of the non-supercell tornado in stage VI, as the low-level circulation becomes displaced from the convective updraft.

A theoretical study by Mak (2001) confirms that misocyclones can form without moist processes via non-hydrostatic barotropic instability; however, growth of the vortices by stretching likely requires moist processes. A more recent radar-based observational study by Marquis et al. (2007) confirms the enhanced convergence pattern associated with misocyclones (e.g., Lee and Wilhelmson 1997a,b).

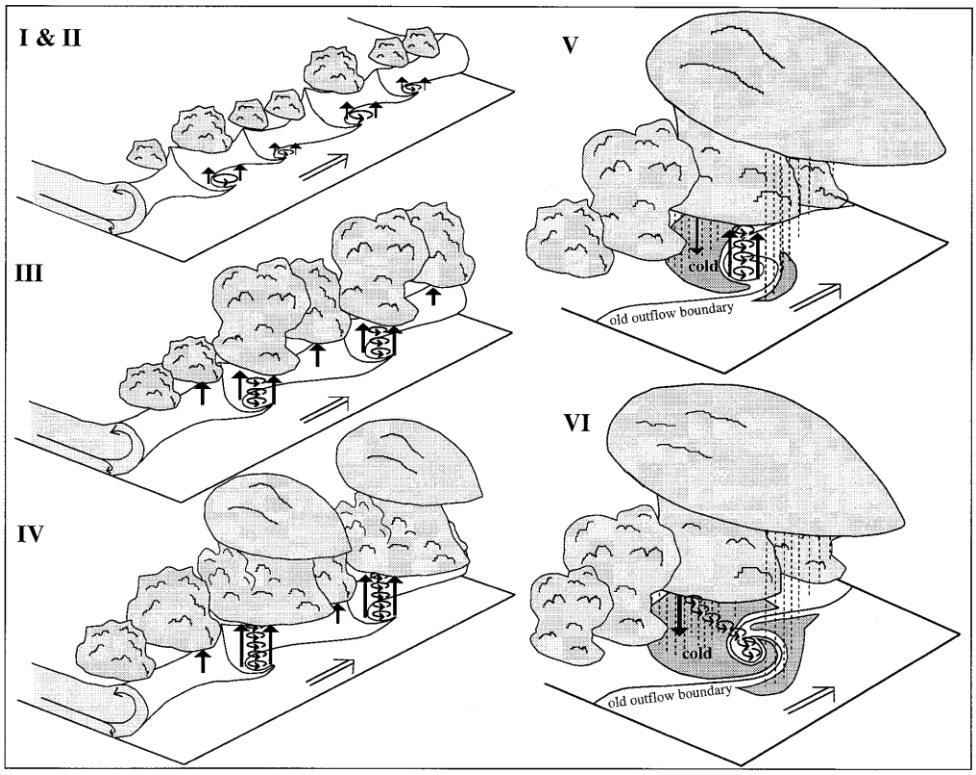

Fig. 2.8. Six stage conceptual whereby non-supercell tornadoes are thought to develop in convective updrafts along a pre-existing shear zone. Reproduced from Lee and Wilhelmson 1997b).

2.3.2 QLCS tornadoes

The tendency of quasi-linear convective systems (QLCSs) to produce tornadoes has been well documented (e.g, Forbes and Wakimoto 1983; Przybylinski 1995; Atkins et al. 2004; Davis et al. 2004; Wakimoto et al. 2006a; Atkins and Laurent 2009a, b). Moreover, a climatological study by Trapp et al. (2005b) showed that about 18% of tornadoes were spawned by QLCSs. QLCS tornadoes typically form in association with strong, long-lived low-level meso-γ-scale (e.g., Orlanski 1975) vortices, hereafter referred to as mesovortices. These mesovortices are not only associated with tornadoes in QLCSs, but also have been shown to be responsible for most of the wind damage reports associated with QLCSs (e.g., Wakimoto et al. 2006b). Observational studies (e.g., Atkins et al. 2004; Atkins et al. 2005) have found a clear relationship between

mesovortex lifetime, strength, and propensity to produce tornadoes. For example, Atkins et al. (2004) find an average lifetime of 76 min for tornadic mesovortices vs. 32 min for non-tornadic mesovortices.

The formation and evolution of mesovortices has been studied in detail through both idealized numerical simulations (Trapp and Weisman 2003; Weisman and Trapp 2003; Atkins and Laurent 2009b, a) and dual-Doppler analyses (e.g., Wakimoto et al. 2006a). Trapp and Weisman (2003) proposed that mesovortices are generated as vortex couplets via downward tilting of southward pointing cold pool vortex lines along the gust front by a precipitation-induced downdraft (Fig. 2.9a). However, the dual-Doppler analysis of Wakimoto et al. (2006a) suggested that this downdraft was induced mechanically by the pressure-field rather than by precipitation loading (Fig. 2.9b).

Regardless of the origin of the downdraft, the formation mechanism of Trapp and Weisman (2003) and Wakimoto et al. (2006a) implies the anticyclonic vortex is north of the cyclonic vortex in the couplet. In contrast, Atkins and St. Laurent (2009b, hereafter AL09) explain that upward tilting of crosswise southward-pointing cold pool vortex lines occurs due to a locally enhanced updraft along a bulge in the convective outflow[3] (Fig. 2.9c). For a low-level westerly momentum surge in the Northern Hemisphere, this implies the cyclonic vortex is the poleward one within the vortex couplet. AL09 also proposes a second mesovortex generation mechanism that involves the development of only a cyclonic mesovortex via tilting of baroclinically generated streamwise horizontal vorticity into the vertical and subsequent stretching by the updraft along the convective storm-generated gust front (Fig. 2.9d). The authors note

[3] This mechanism is similar to the process by which line-end vortices in MCSs develop (Weisman and Davis 1998), as well as to the vortex line arches presented in Straka et al. (2007) and Markowski et al. (2008).

that this genesis mechanism is similar to the proposed mechanism for the genesis of the low-level mesocyclones in supercells (e.g., Rotunno and Klemp 1985). Observational examples exist for vortex couplets owing to upward tilting (e.g., Atkins et al. 2004, 2005; (Wheatley et al. 2006) and downward tilting (e.g., Wakimoto et al. 2006a; Wheatley and Trapp 2008). There is currently little explanation or reconciliation between the differing vortex formation mechanisms of Trapp and Weisman (2003), Wakimoto et al (2006a), and AL09.

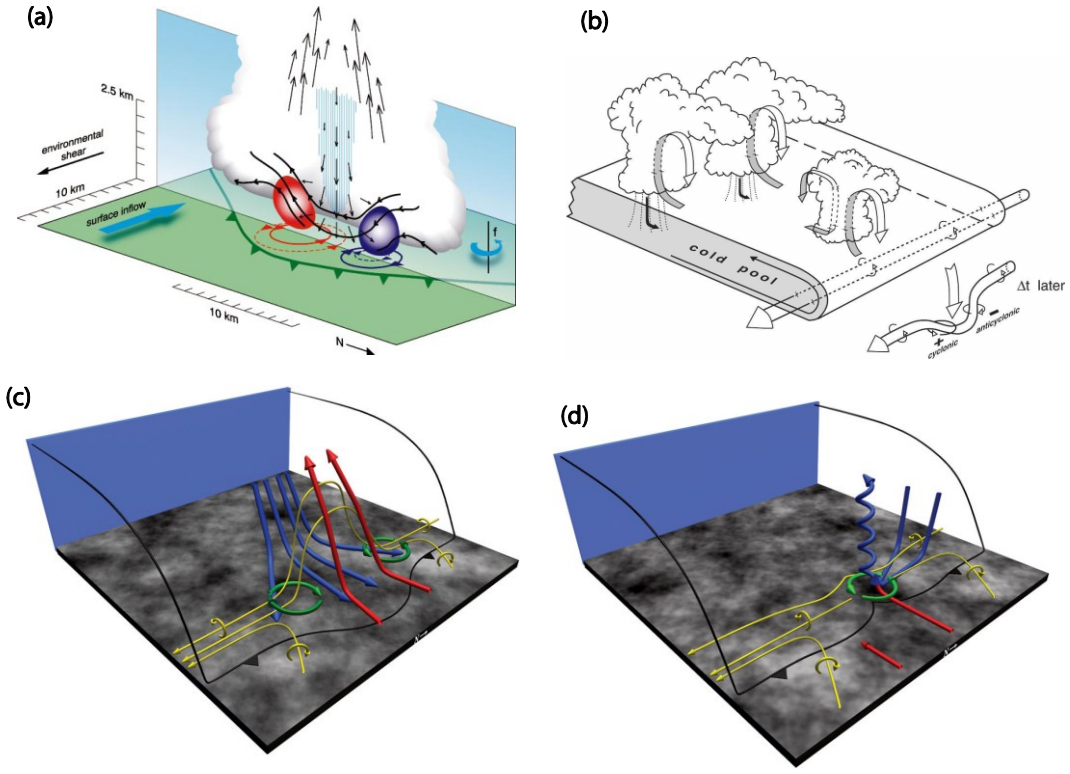

Fig. 2.9. Four different conceptual models explaining the generation of mesovortices in quasi-linear convective systems. Panel (a) is reproduced from Trapp and Weisman (2003) and features a vortex couplet that is generated as a rainy downdraft tilts baroclinically generated horizontal vortex lines downward. Panel (b) is reproduced from Wakimoto et al. (2006a) and also features baroclinically generated vortex lines that are tilted downward but by a mechanically induced downdraft rather than by water loading and evaporation. Both (c) and (d) are reproduced from Atkins and St. Laurent (2009b). In (c), baroclinically generated crosswise vortex lines are tilted upward leading to a vortex couplet that has the opposite orientation to that in (a) and (b). In (d), a single cyclonic mesovortex is generated via upward tilting of baroclinically streamwise vorticity along the gust front.

While the above studies disagree on the details of the mesovortex formation mechanism and the orientation of the vortex couplet, they do agree that mesovortices tend to be stronger and longer-lived in environments with stronger low-level shear. The studies explain that stronger shear leads to updrafts that are stronger and more upright, leading to more intense stretching of low-level vorticity. This result has recently been confirmed in a study by Schenkman et al. (2011a ; hereafter, S11a), wherein real-data experiments that more effectively analyzed low-level shear forecasted stronger, longer-lived mesovortices.

The dynamical link between mesovortices and tornadoes remains relatively unexplored. To the authors' knowledge, no study has examined a case with sufficient resolution (either observationally or numerically) to capture concurrent mesovortex and tornado circulations. The following chapter aims to do this by analyzing high-resolution numerical modeling results of a real-data initialized convective storm and the associated mesovortex which produced a sub-mesovortex scale tornado-like vortex[4] (hereafter, TLV).

[4]The vortex is referred to as 'tornado-like' because even with 100-m grid-spacing, the simulation cannot fully resolve the vortex structure, thus it cannot be said for certain that the simulated vortex qualifies as a tornado.

Chapter 3: Tornadogenesis in a Simulated Mesovortex within a Mesoscale Convective System[5]

3.1 Overview of the 8-9 May 2007 and associated mesovortices

On 8-9 May 2007, a MCS (Fig. 3.1) moved through much of the western half of Texas and Oklahoma. A well-defined line-end vortex (LEV) developed in the northern portion of the main convective line of the MCS as it moved into southwest Oklahoma. Convective cells associated with the LEV produced several weak tornadoes that struck parts of southwest and central Oklahoma. According to a National Weather Service (NWS) damage survey (NCDC Storm Data), the first tornado caused EF-1 damage in Grady County, near Minco. Another weak tornado produced EF-0 damage near Union City in Canadian County. The most destructive tornado, a high-end EF-1, caused an estimated three million dollars of damage in El Reno, Oklahoma. Two very short-lived EF-1 tornadoes were reported a short time after the El Reno tornado near Piedmont.

Examination of radial velocity observations of the 9 May 2007 MCS and LEV from the Oklahoma City Terminal Doppler Weather Radar (TDWR) over the period 0300 through 0500 UTC reveals at least five distinct mesovortices (not shown). All of the mesovortices developed on the southeast side of the LEV during the comma-echo stage of the MCS (Fujita 1978). Radar reflectivity observations indicate that the mesovortices were associated with strong convective cells embedded within the head of the comma echo (see the zoomed in portion of Fig. 3.1). The wind field around the LEV caused the mesovortices to move to the north and west. As the mesovortices

[5] This chapter (as well as section 2.3.2) is adapted from Schenkman et al. (2012).

intensified, the associated convective cells briefly took on supercellular characteristics with hook-echoes becoming apparent. A particularly well-defined hook echo is apparent in TDWR observations (not shown) of the convective cell associated with the mesovortex that spawned the Minco tornado (hereafter, the Minco mesovortex).

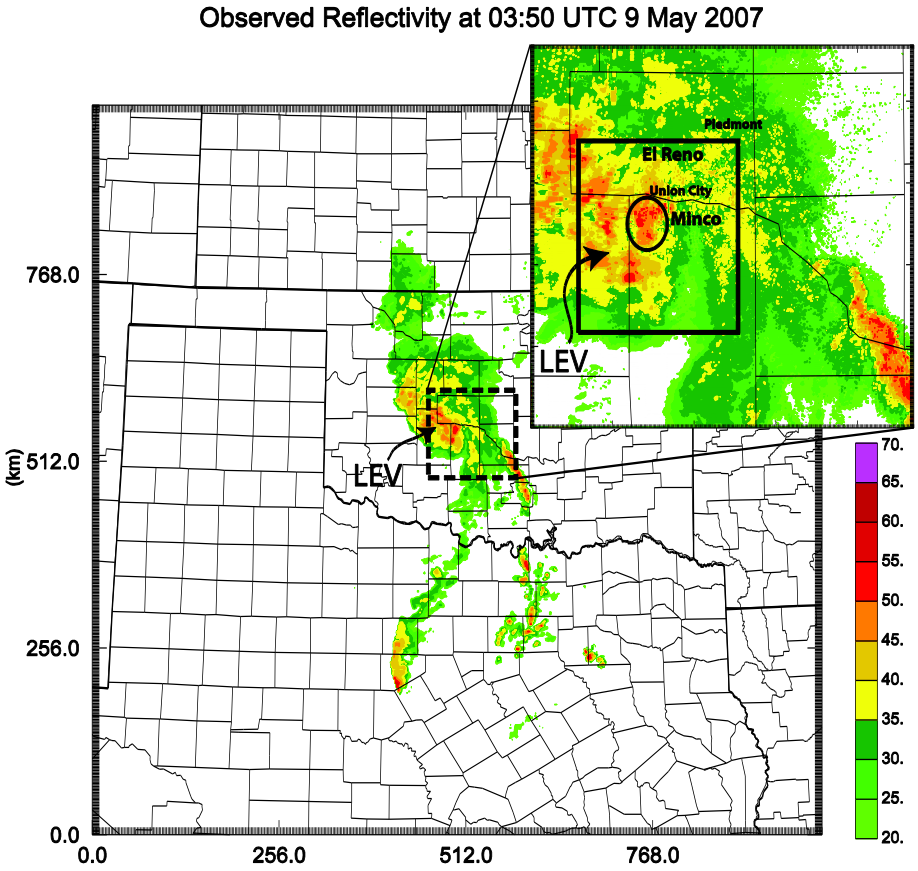

Fig. 3.1. Map of observed radar reflectivity factor at 1 km AGL at 0350 UTC 9 May 2007 within the 2-km resolution computational domain used in Schenkman et al. (2011b). The dashed-line rectangle marks the location of the 400-m resolution domain used in S11a. The image at the upper-right zooms into the 400-m domain. The solid rectangle marks the location of 100-m resolution computational domain. The oval contains the convective cell associated with the Minco mesovortex. The location of the LEV and selected town names are indicated.

Only two of the five mesovortices present in the 9 May 2007 MCS were tornadic. These two were stronger and longer-lived than the non-tornadic mesovortices

(See Table 1 in S11a). Both the Minco and Union City tornadoes appear to have formed in association with the Minco mesovortex. The mesovortex associated with the El Reno tornado formed immediately after the dissipation of the Union City tornado. The El Reno mesovortex persisted after the dissipation of the El Reno tornado and spawned the two brief Piedmont tornadoes (See Fig. 3.1 for a map with town names).

Numerical forecasts presented in S11a successfully simulated the genesis and evolution of the Minco mesovortex on a 400 m resolution grid. Experiments that assimilated radial velocity data from the CASA IP-I radar network (McLaughlin et al. 2009) were particularly accurate in their forecast of the Minco mesovortex (S11a). In this study, a simulation with 100-m grid spacing is nested within one of the experiments that assimilated CASA radial velocity (Vr) data (experiment CASAVrZ5MM in S11a), and the model integration is performed only over the lifespan of the Minco mesovortex. We focus on analyzing the results of this high-resolution simulation, and seek to understand and explain the development of the TLV associated with the Minco mesovortex. The rest of this chapter is organized as follows: section 3.2 briefly describes the configurations of the numerical simulations; section 3.3 describes the evolution of the simulated Minco mesovortex with a detailed analysis of the genesis of a simulated intense low-level TLV. A summary and conclusions are given in section 3.4.

3.2: Experiment design

The numerical simulation was performed using the Advanced Regional Prediction System (ARPS;Xue et al. 1995; Xue et al. 2000; Xue et al. 2001; Xue et al. 2003) model. The ARPS model is three-dimensional, fully-compressible, and non-hydrostatic. It was configured with fourth-order advection in the horizontal and

vertical, a rigid top boundary condition with a wave absorbing layer beginning at 12 km AGL, fourth-order computational mixing, a 1.5-order TKE-based subgrid-scale turbulent mixing scheme and PBL parameterization, and Lin et al. (1983) three-ice microphysics with the rain intercept parameter set to 8.0 x 10^5 m^{-4} according to Snook and Xue (2008). The Coriolis parameter is latitude dependent and includes the effect of earth curvature. A multilayer land surface model is used that is similar to the NOAH land surface model (Chen and Dudhia 2001), with five vertical soil levels. Surface fluxes are determined using a drag coefficient of $3x10^{-3}$, and the skin temperature and top soil moisture content predicted from the land surface model [option *sfcphy*=3, see Xue et al. (1995) for more details]. The domain combines 100-m grid spacing in the horizontal with a vertically stretched grid based on a hyperbolic tangent function (Xue et al. 1995) with a minimum spacing of 20 m near the ground, and the stretching tuning parameter set to 1.0. The model domain is 50 km x 60 km x 30 km with 60 vertical levels.

The 100-m resolution model domain is one-way nested within two outer grids (see Fig. 3.1). The outermost grid has 2-km horizontal spacing and is intended to capture the overall evolution of the MCS and LEV of 8-9 May 2007 (Schenkman et al. 2011b). A 400-m resolution grid was nested inside of the 2-km grid. This nest was designed to capture the mesovortices associated with the 8-9 May 2007 MCS case, through the assimilation of high-resolution wind data from the CASA radars. Results showed that when the low-level shear in advance of the surface cold pool produced by the MCS was properly analyzed, it was possible to forecast the evolution of the Minco mesovortex with good accuracy. In contrast, simulations with less accurate analyses of

the low-level shear produced only weak, short-lived mesovortices. More details on the ARPS 3DVAR data assimilation scheme and the role of low-level shear in accurately forecasting this event are provided in S11a and Schenkman et al (2011b). A 40-min forecast on the 400-m resolution grid from the CASAVrZ5MM experiment in S11a provided the initial condition at 0300 UTC (through spatial interpolation) and boundary conditions at 5-min intervals to the 100-m resolution grid. As explained in S11a, the CASAVrZ5MM experiment is run with an 80-min assimilation window (0100-0220 UTC) in which observations from WSR-88D, CASA, and Oklahoma Mesonetwork are assimilated every 5 min. A free forecast is then run from 0220 UTC thru 0500 UTC 9 May 2007. Simulations on the 100-m resolution grid are run from 0300 to 0410 UTC 9 May 2007. The start time of the 100-m simulation (0300 UTC) is slightly before the genesis of the Minco mesovortex in the 400-m simulation. This allows for the detailed examination of both the genesis and intensification of the Minco mesovortex using 100-m grid spacing.

3.3 The simulated mesovortex and associated tornado-like vortex

3.3.1 General overview of the 100-m grid-spacing numerical simulation

The 100-m simulation begins at 0300 UTC with a well-defined gust front at the low levels (Fig. 3.2a). This gust front marks the leading edge of an outflow surge associated with strong convection near the center of the LEV (see the discussion of the secondary outflow surge in S11a). The gust front is initially oriented north-south. An initial mesovortex[6] is present along the northern portion of the gust front (Fig. 3.2a).

[6] As in S11a, a circulation is considered a mesovortex if it has maximum vertical vorticity > 0.025 s-1 and persists for at least 15 min. These criteria are kept the same despite increased resolution of the present study because mesovortices were already resolved fairly well on the 400 m grid in S11a.

Over the next five minutes, a gust front bulge develops to the southeast of the initial mesovortex. An enhanced updraft develops along the gust front bulge, leading to the generation of cyclonic (anticyclonic) vorticity on the northern (southern) side of the bulge (Fig. 3.2b). The vortex line plotted in Fig. 3.2b arches from the cyclonic vorticity to the area of anti-cyclonic vorticity indicating that the baroclinically generated southward-pointing horizontal vortex lines at the gust front are tilted into the vertical at the bulge, creating the vorticity couplets. The arrangement of the vorticity centers within the couplets is similar to that of the mesovortex couplets discussed in AL09, because the couplets are generated through enhanced updraft between the vorticity centers.

Calculations of the Okubo-Weiss number (e.g., Markowski et al. 2011) were also examined (not shown) to verify that mesovortices were in fact vortices and not just long-lived shear lines.

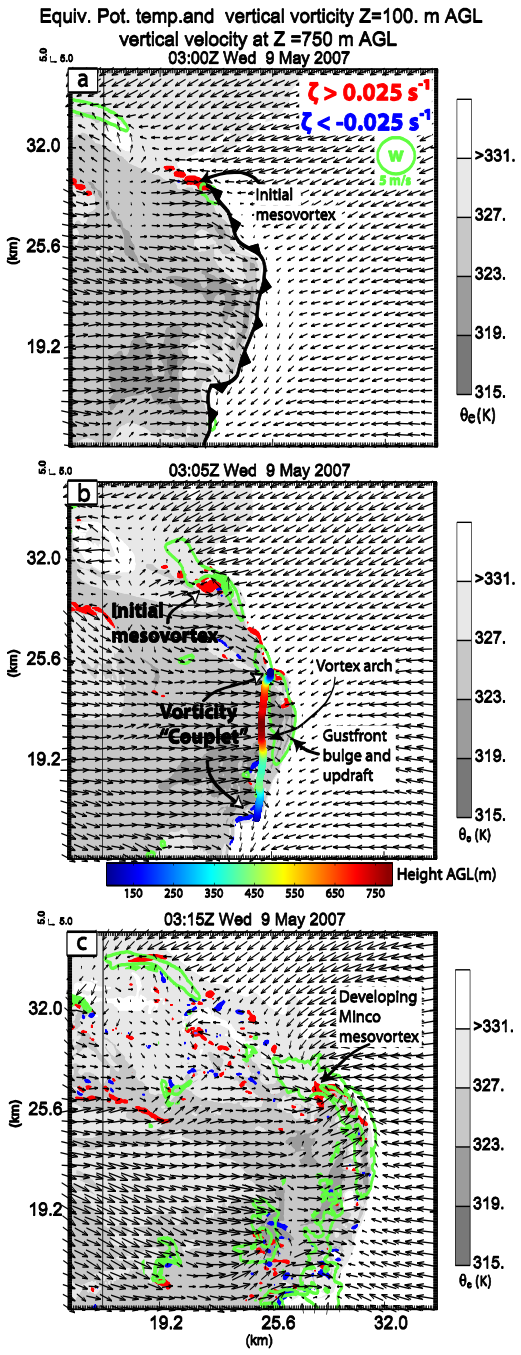

Fig. 3.2. Equivalent potential temperature (shaded, K), horizontal wind (vectors, m s -1), positive vertical vorticity >0.025 s-1 (shaded in red), negative vertical vorticity < -0.025 s-1 (shaded in blue) at 100-m AGL and vertical velocity (> 5 m s-1, heavy green contours) at 750-m AGL at (a) 0300 UTC, (b) 0305 UTC, and (c) 0315 UTC 9 May 2007. The heavy black line in (a) marks the gust front. For clarity, this line is neglected in (b) and (c). In (b) "couplets" is put in quotation marks to imply that while there are not well defined vorticity couplets, there is predominantly positive (negative) vorticity on the northern (southern) side of the gust front bulge. A vortex line, color coded by height AGL, is plotted in (b).

The initial mesovortex decays rapidly, dissipating by 0315 UTC. S11a also discussed this initial mesovortex and showed that it was short-lived because it was generated in an area of weak low-level shear. Meanwhile, the anticyclonic vorticity on the south side of the gust front bulge remains disorganized and does not form a well-defined anticyclonic mesovortex. In contrast, the cyclonic vorticity on the north side of the gust front bulge intensifies[7] and the Minco mesovortex develops by 0315 UTC (Fig. 3.2c). S11a found that the Minco mesovortex developed in an area of much stronger low-level shear than the initial mesovortex (see their Fig. 9).

The Minco mesovortex continues to intensify through 0330 UTC. Concurrently, the flow field associated with the mesovortex begins to resemble that of a divided supercell low-level mesocyclone (Lemon and Doswell 1979), with a strong updraft in the western and northern parts of the circulation and a strong downdraft in the eastern sector of the circulation (Fig. 3.3a). Unlike a supercell, however, there is not a persistent mid-level mesocyclone associated with the low-level circulation (not shown). A TLV forms in association with the intensifying mesovortex around 0327 UTC. This TLV will be discussed in detail in the next sub-section.

After 0330 UTC, the Minco mesovortex begins to broaden and weaken. As this occurs, the updraft in the western and northern sectors of the mesovortex rapidly weakens, and much of the circulation becomes embedded in downdraft by 0340 UTC (Fig. 3.3b). By 0355 UTC, the Minco mesovortex broadens substantially with a

[7] The idealized simulations in Trapp and Weisman (2003) found that the cyclonic circulation in a mesocyclone couplet is favored due to Coriolis forcing. However, the Coriolis force is not important on spatial scales of a few kilometers and temporal scales of a few minutes. As such, in the case under consideration, the pre-existing mesoscale cyclonic vorticity associated with the LEV can also act to enhance the cyclonic circulation, especially through low-level convergence and vertical stretching associated with the cyclonic mesovortex. A similar process will act to weaken the anticyclonic vorticity.

disorganized vertical velocity field (not shown). The Minco mesovortex gradually decays throughout the remainder of the simulation.

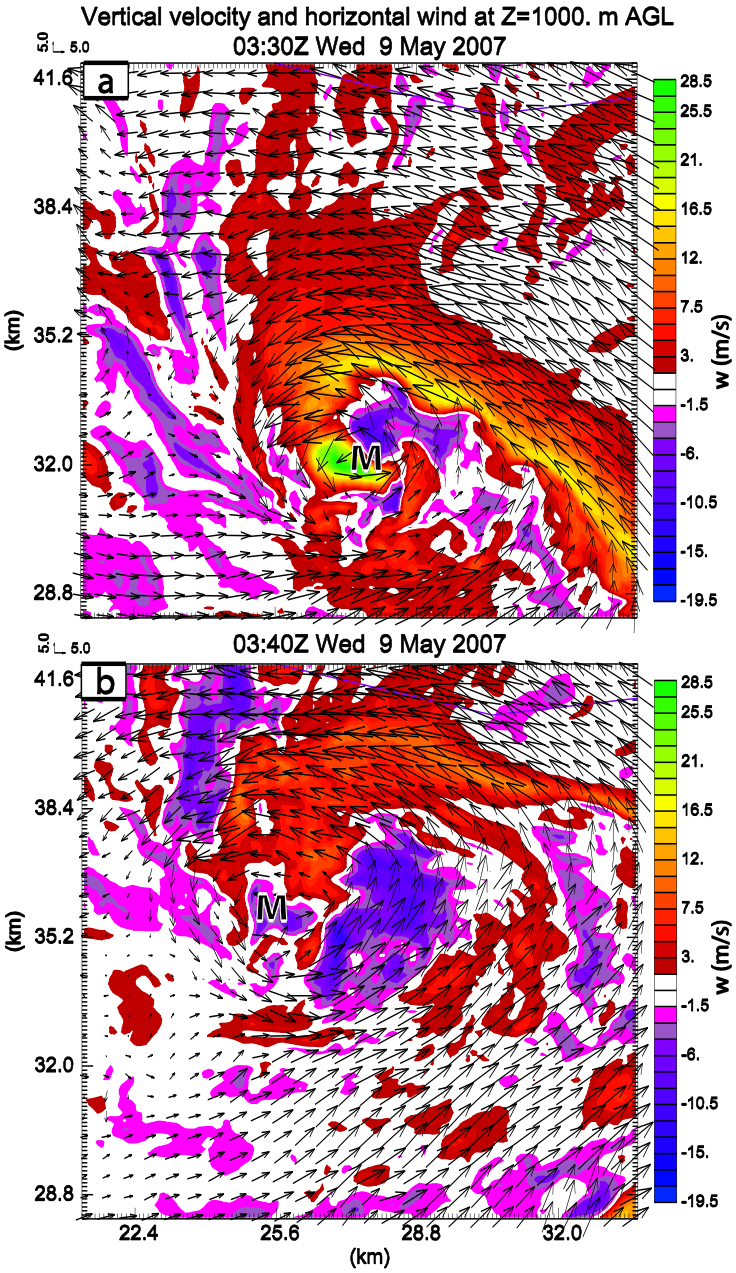

Fig. 3.3. Vertical velocity (m s-1, shaded) and horizontal wind (m s-1, vectors) at 1000 m AGL at (a) 0330 UTC and (b) 0340 UTC 9 May 2007. 'M' marks the approximate center of the Minco mesovortex.

3.3.2 Genesis of a tornado-like vortex

Closer examination of the simulated Minco mesovortex reveals the presence of several submesovortex-scale vortices. Most of these vortices are short-lived and do not produce tornado strength winds. However, one of the vortices is longer-lived and produces EF-0 (40 m s^{-1}) strength winds. The remainder of this sub-section discusses this tornado-like vortex (TLV). In this study, a TLV is defined as a clearly-discernible area of rotation that persists for at least 2 min with maximum vertical vorticity > 0.2 s^{-1} and winds speeds of EF-0 intensity or greater. For convenience in the discussion of the TLV, the following naming convention is used: the bulging portion of the gust front that extends from the Minco mesovortex to the east is hereafter referred to as the rear-flank gust front (RFGF); the gust front that is located to the west of the Minco mesovortex is referred to as the forward flank gust front (FFGF). This naming convention was chosen because the features closely resemble RFGF and FFGF appearance in supercell storms (e.g., see Fig. 2.3 adapted from Lemon and Doswell 1979). This naming convention is meant to simplify the description of the TLV-relative location and appearance of these features and *not* to suggest that we are simulating a classic supercell. The FFGF and RFGF are denoted in Fig. 3.4a.

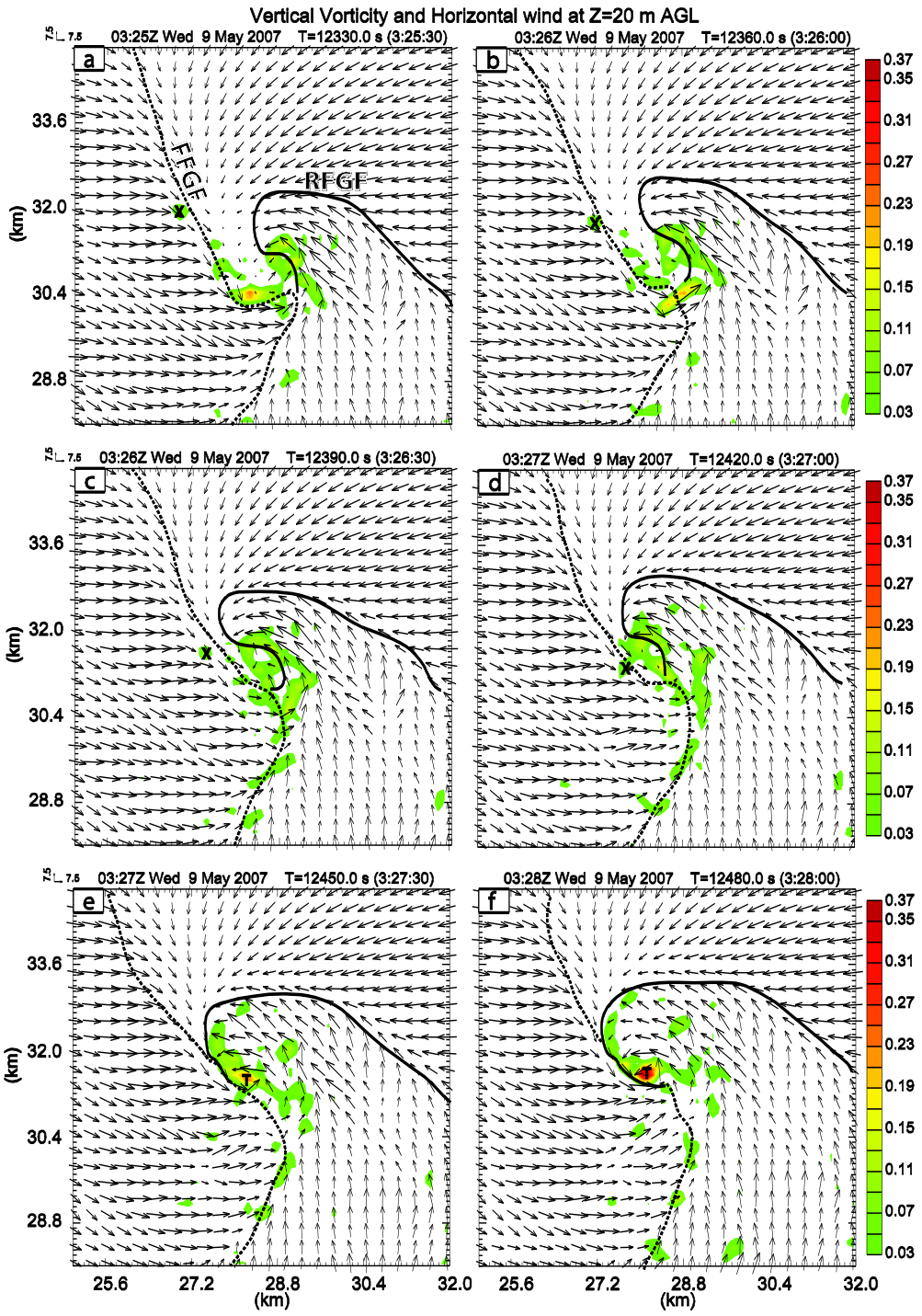

Fig. 3.4. Horizontal wind vectors (m s -1) and vertical vorticity (color shaded, s-1) at 20 m AGL at (a) 0325:30 UTC, (b) 0326:00 UTC, (c) 0326:30 UTC, (d) 0327:00 UTC, (e) 0327:30 UTC, and (f) 0328:00 UTC 9 May 2007. The 'X' in (a-c) marks the location of a small area of cyclonic vorticity that merges with the TLV. The 'T' in (e-f) marks the location of the TLV. The solid and dotted black lines mark the locations of the rear and forward flank gust fronts, respectively. These gust fronts are hand-analyzed through the relative maximum in convergence.

With the above definitions in mind, the evolution of the TLV is now discussed. The TLV forms very rapidly around 0327 UTC as low-level vorticity associated with the Minco mesovortex[8] along the occluding RFGF moves to the northwest and merges with a small vertical vorticity maximum (While this feature is fairly weak, it is persistent and can be tracked back for several minutes prior to TLV genesis. The role of this feature is discussed at the end of this subsection.) that is associated with a surge of westerly momentum at low levels (Fig. 3.4a-c). The developing TLV rapidly contracts with maximum vertical vorticity values increasing from 0.1 s^{-1} to 0.4 s^{-1} in about 60 s (Fig. 3.4d-e). The TLV broadens slightly over the next few minutes while maintaining its intensity (Fig. 3.5a,b). Around 0333 UTC, the TLV broadens and weakens rapidly (Fig. 3.5c) as a strong downdraft forms in its eastern half. This downdraft is only present at low-levels and is dynamically induced by the ~12 hPa low-level pressure drop associated with the TLV (Fig. 3.5a). At the same time, a strong vorticity maximum (marked by 'Y' in Fig. 3.5c) forms to the west of the TLV center. This vorticity maximum is very short lived and has dissipated by 0335 UTC (Fig. 3.5d).

[8] Owing to insufficient model resolution and complicated flow evolution, it is very difficult to determine whether the Minco mesovortex simply contracts and becomes the TLV or if some of the vorticity associated with the Minco mesovortex is concentrated with the Minco mesovortex remaining a separate feature. It may also be unlikely that such a distinction is clear in the actual atmosphere.

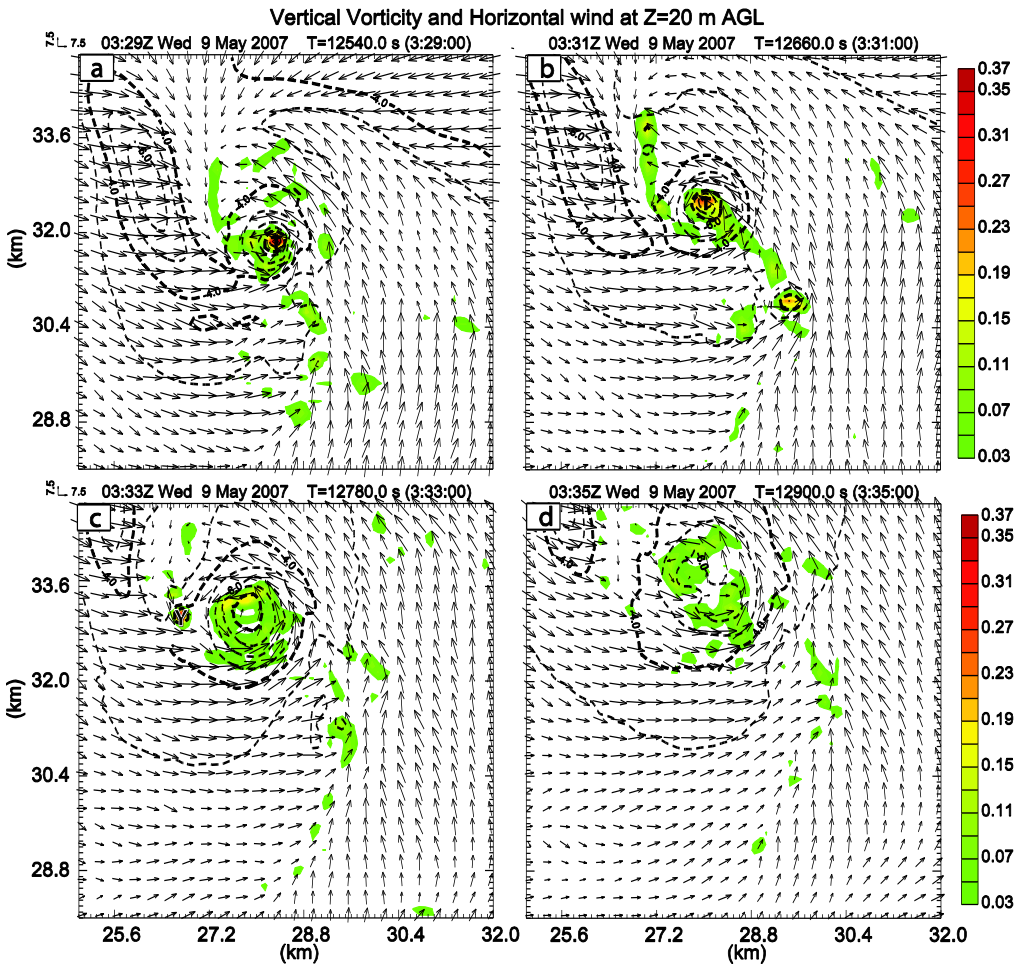

Fig. 3.5. As Fig. 3.4 but at (a) 0329 UTC, (b) 0331 UTC, (c) 0333 UTC, and (d) 0335 UTC. Dashed contours are perturbation pressure (Pa, starting at -300 Pa). The minimum perturbation pressure is ~-1260 Pa in the center of the TLV in (a). The 'Y' in (c) marks a short-lived area of vorticity that forms after the demise of the TLV. Gust fronts are neglected because they have moved out of the plotted area by 0331 UTC.

While the dynamics behind the mature and decaying stages of the TLV are easily explained by the associated low-level pressure perturbation, the rapid genesis and intensification of the TLV warrant closer inspection. Time-height plots of maximum vertical velocity and vorticity indicate that the TLV was associated with a strong updraft, with w > 20 m s^{-1} at 500 m AGL (Fig. 3.6). This low-level updraft formed before, and dissipated after, the TLV. Backward trajectory calculations terminating in the TLV confirm that this updraft played a key role in TLV intensification as low-level

stretching, due to the rapidly increasing updraft above the ground, is the dominant vorticity generation term (Fig. 3.7). Thus, it is important to determine the mechanism by which this intense low-level updraft was generated and maintained, as it plays a critical role in the TLV genesis and maintenance.

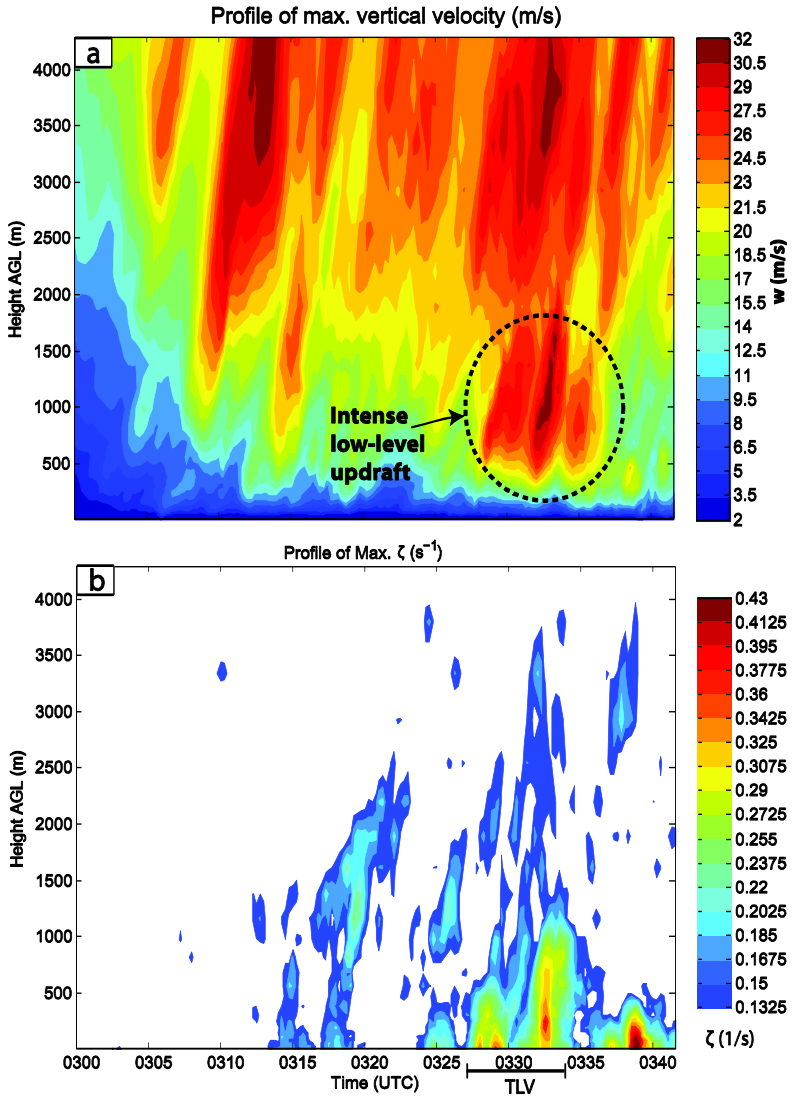

Fig. 3.6. Time-height profiles of (a) maximum vertical velocity (m s-1) and (b) vertical vorticity (s-1) from 0300 to 0342 UTC. Profiles are calculated over a 32 x 42 km subdomain that is centered on the Minco mesovortex and excludes an additional storm in the southeast portion of the domain. The subdomain is chosen to be fairly large in order to include both the mid-level and low-level updrafts through the entire 42 min period. The dotted oval marks the intense low-level updraft located on the west side of the Minco mesovortex.

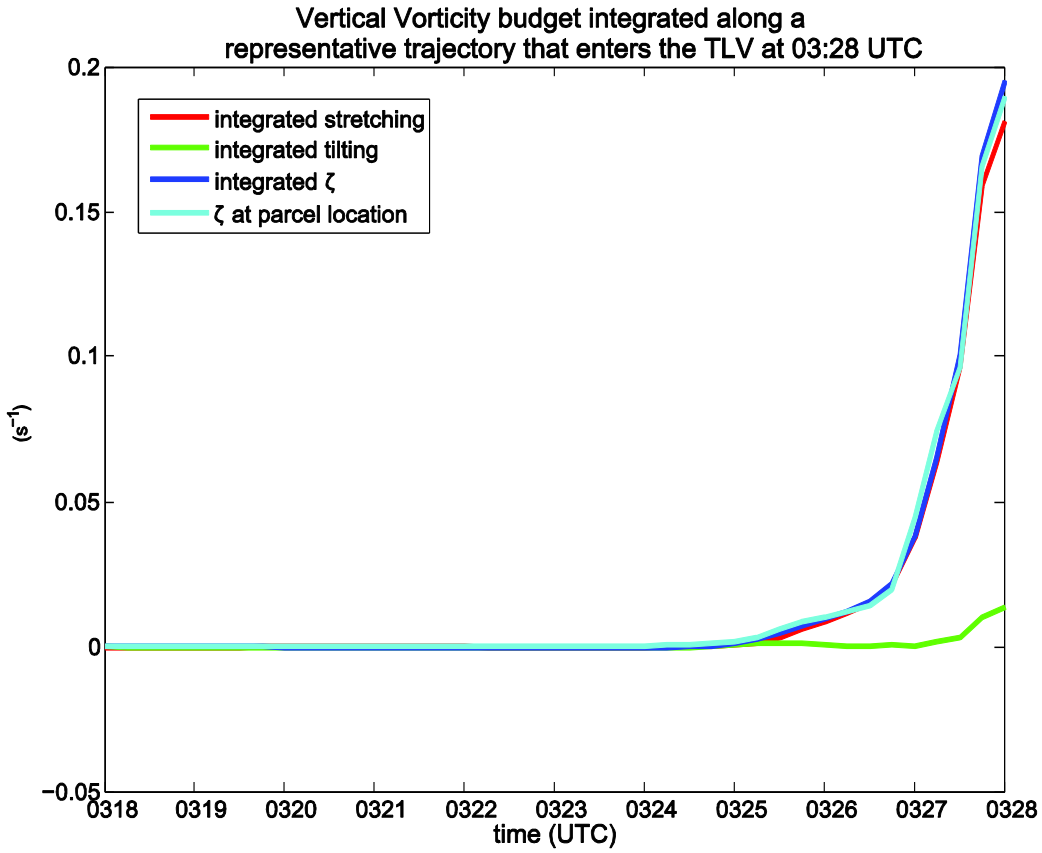

Fig. 3.7. Vertical vorticity budget along a representative backward trajectory that is initialized 100 m AGL near the TLV center at 0328 UTC. The blue line is the sum of the time-integrated vertical vorticity generated through vertical stretching (red line) and tilting (green line). The cyan line represents the vertical vorticity interpolated from the model grid to the location of the parcel at each time. Trajectories are calculated using a 4th order Runge-Kutta integration scheme with 3 s model output. The Lagrangian time integration agrees very well with the Eulerian vorticity prediction by the model in this case.

Examination of low-level flow fields in the five minutes leading up to the development of the TLV reveals that the intense low-level updraft forms along the FFGF. The intense low-level updraft is associated with strong near-surface convergence between easterly flow associated with the occluding RFGF and a narrow band of enhanced westerly flow just to the west of the FFGF (Fig. 3.8a). Vertical cross sections reveal that this westerly flow comprises the bottom part of a rotor that has

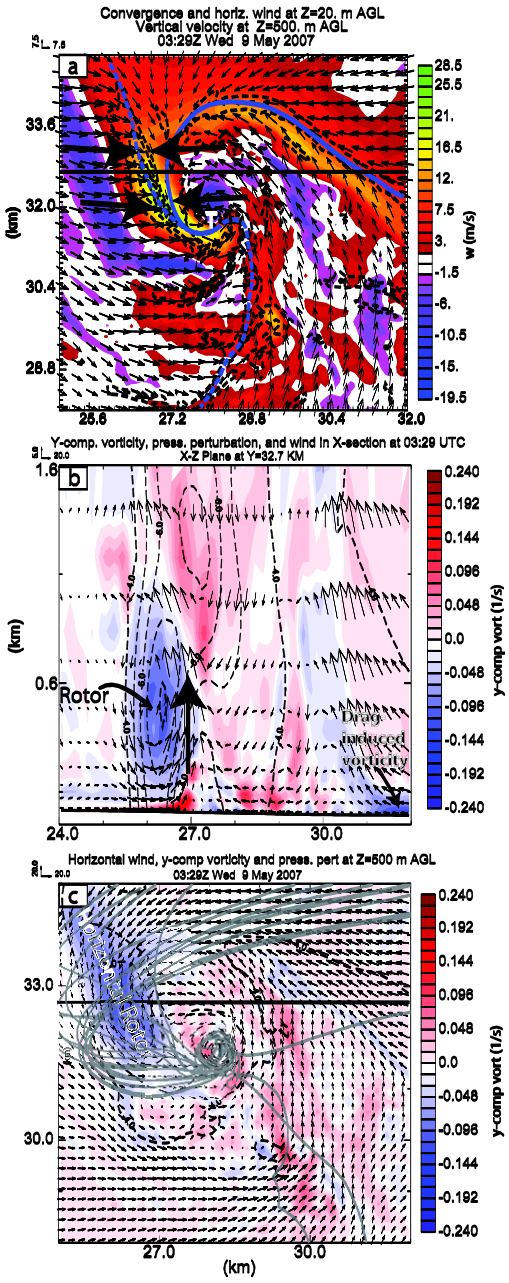

Fig. 3.8. (a) Vertical velocity (shaded, m s-1) at 0329 UTC at 500 m AGL overlaid with horizontal wind (vectors, m s -1) and convergence (s-1) at 20 m AGL. The large black arrows indicate the direction of flow behind the FFGF (dotted blue line) and RFGF (solid blue line) (b) Cross-section along the heavy black line in (a) and (c). Y-component vorticity (shaded, s-1), perturbation pressure (dashed contours, Pa) and wind vectors are plotted in the plane of the cross-section. The large black arrow indicates the location of the strong low-level updraft. (c) Y-component vorticity (shaded, s-1) , perturbation pressure (dashed contours, Pa) and horizontal wind (vectors, m s-1) at 500 m AGL. A 600-m diameter ring of backward trajectories (gray lines) that enter the TLV circulation at 500 m AGL are overlaid in (c). The 'T' in (a) and (c) marks the approximate TLV center.

formed immediately to the west of the FFGF (Fig. 3.8b). This rotor is about 1 km deep, 2 km wide and 4 km long and is oriented along the FFGF (Fig. 3.8c). A 600-m diameter ring of 18 backward trajectories that is initialized around the TLV is also plotted in Fig. 3.8c. The majority of these trajectories pass through the rotor.

The rotor forms around 0320 UTC in association with a surge of westerly momentum at low-levels, which is the result of a low-level downdraft that is associated with the dissipation of the first mesovortex (cf. Fig. 3.2c). As this surge of momentum impinges on the FFGF from the rear, the rotor circulation rapidly intensifies (this rapid intensification will be discussed and shown further in section 3.3.4). This rapid intensification is coincident with a ~8 hPa pressure drop [likely due to the increase in horizontal vorticity as reflected in the 'spin' term of the diagnostic pressure perturbation equation (e.g., eq. (2.131) in Markowski and Richardson 2010)], along the central axis of the rotor by 0325 UTC. It is at this point that the strong low-level updraft forms in the ascending branch of the rotor. TLV genesis occurs rapidly as low-level vertical vorticity associated with the Minco mesovortex moves into the strong convergence associated with the low-level updraft/rotor. This can be seen in Fig. 3.4 as the broad area of vorticity associated with the Minco mesovortex on the left side of the RFGF moves towards FFGF during occlusion.

Another source of vorticity for the TLV is the horizontal vorticity of the rotor itself. Fig. 3.9 indicates that this vorticity is tilted into the vertical and is responsible for the generation of the small vorticity maximum introduced above and highlighted in Fig. 3.4a-d. However, a circulation analysis, in which a 200-m radius ring made up of 3600 parcels surrounding the TLV is initialized 100-m AGL and the parcel trajectories are

integrated backward in time, indicates that this is likely a secondary effect. More specifically, the circulation around the circuit remains nearly constant while the area it encloses decreases dramatically (Fig. 3.10). Thus, according to Stoke's theorem, the vorticity component normal to the area enclosed by the circuit must increase. Moreover, most of the circuit during this time is nearly horizontal; suggesting much of the normal vorticity component is vertical vorticity. This suggests that convergence into the low-level updraft amplifies pre-existing vorticity within the circuit, leading to TLV development through conservation of angular momentum. Thus, the most important role of the rotor is to cause the concentration and intense stretching (in its upward branch) of pre-existing vertical vorticity associated with the Minco mesovortex (whose vorticity was generated mostly from the tilting of horizontal vorticity along the RFGF).

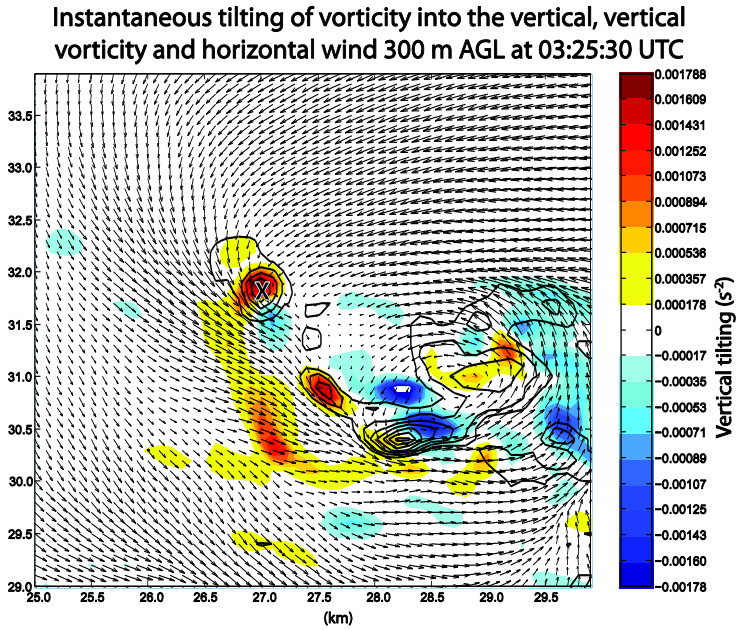

Fig. 3.9. Tilting of horizontal vorticity into the vertical (shaded, s-2), vertical vorticity (contours, s-1), and horizontal wind vectors (m s-1) at 300 m AGL at 03:25:30 UTC. The 'X' marks the location of the small vertical vorticity maximum highlighted in Fig. 3.4

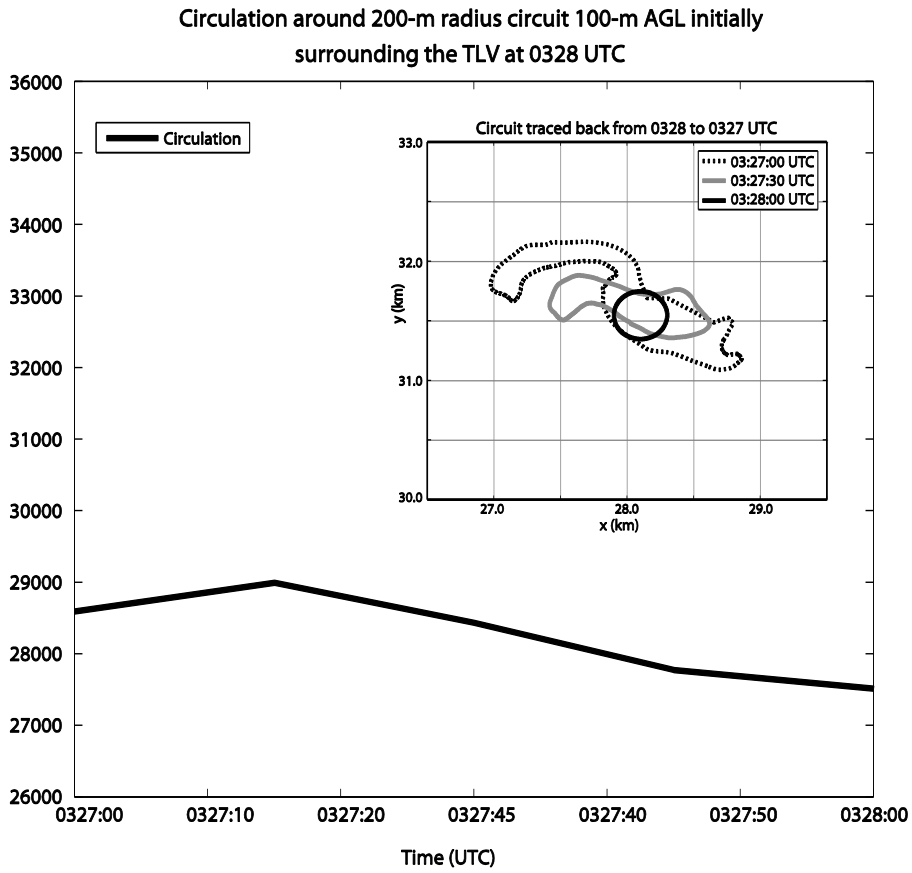

Fig. 3.10. Circulation (black line) around the material circuit (shown in the inset) that was initially (at 0328 UTC) a 200-m radius circle surrounding the TLV 100-m AGL. The circuit is made up of 3600 parcels.

Circulation analyses for longer time periods were also attempted to determine the origin of the circulation (e.g., Rotunno and Klemp 1985). However, circuits become extremely distorted with many overlapping portions and sharp discontinuities after about 90 s of backward integration (not shown), precluding any meaningful analysis.

3.3.3 The generation of the horizontal rotor and low-level updraft

While the important role the rotor plays in TLV genesis in this case has been established, the mechanism responsible for generating the rotor has not yet been examined. To help determine the mechanism, a detailed backward trajectory analysis is performed. This analysis shows that nearly all parcels within the rotor originate at very

low-levels (< 125 m AGL; Fig. 3.11). Furthermore, our trajectory analysis suggests that almost all of the parcels that pass through the rotor came from the inflow air to the northeast of the convective cell. These parcels ascend several hundred meters over the FFGF, descend in the downward branch of the rotor while turning to the south and east, and then ascend sharply in the rotor's upward branch (Fig. 3.12). When plotted in three dimensional space, the typical parcel's path is helical around the rotor's central axis (Fig. 3.12). Inflow parcels have large values of negative y-component vorticity (the same as in the rotor) suggesting this inflow vorticity is the source of the horizontal vorticity in the rotor (see Fig. 3.8b). Given the proximity of these parcels to the ground, the starting location in the fairly thermodynamically-homogenous inflow area (hence, little baroclinic vorticity generation), and large values of vorticity of the opposite sign to the vorticity associated with the environmental shear, it appears likely that these parcels obtained their vorticity from surface drag. Vorticity calculations along backward trajectories that enter the rotor confirm this hypothesis as inflow parcels acquire large negative y-component vorticity from surface drag prior to entering the rotor circulation (Fig. 3.13).

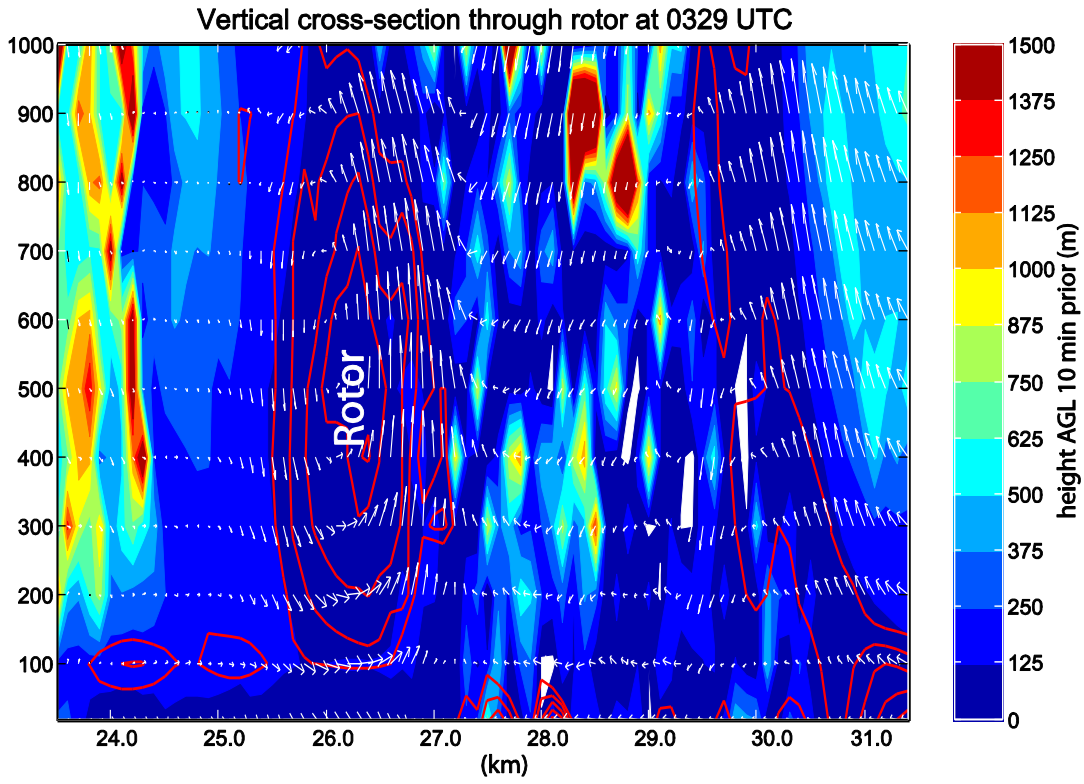

Fig. 3.11. Height AGL that a parcel in a present location at 0329 UTC was located at 0319 UTC (shaded, m AGL), together with the negative Y-component vorticity with a contour interval of 0.02 s-1 beginning at -0.04 s-1 (red contours), and the wind vectors in an east-west cross-section plane (m s-1) along the black line in Fig. 3.8a.

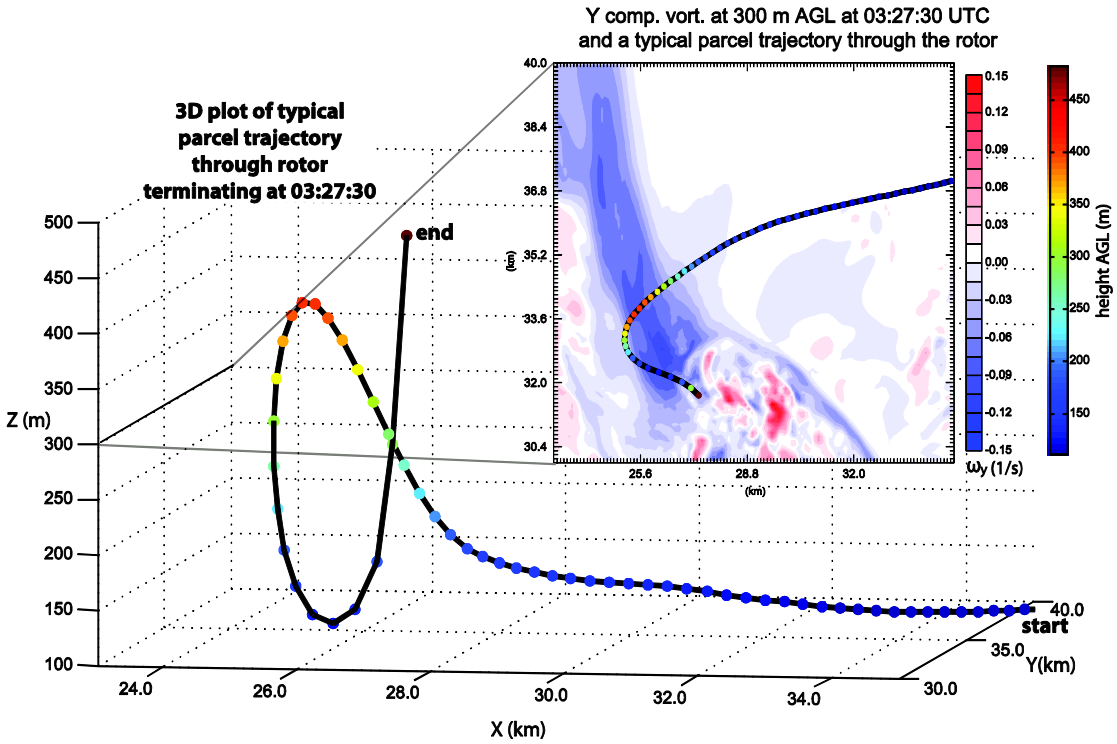

Fig. 3.12. Three dimensional plot (view from the south-southeast) of a typical parcel trajectory traveling through the rotor beginning at 0312:30 UTC and terminating in the rotor's upward branch at 0327:30 UTC. The inset is a XY cross-section plot of the y-component of horizontal vorticity (shaded, s-1) at 0327:30 UTC overlaid with the two-dimensional projection of the trajectory. Dots along the trajectory are color coded by height AGL (m).

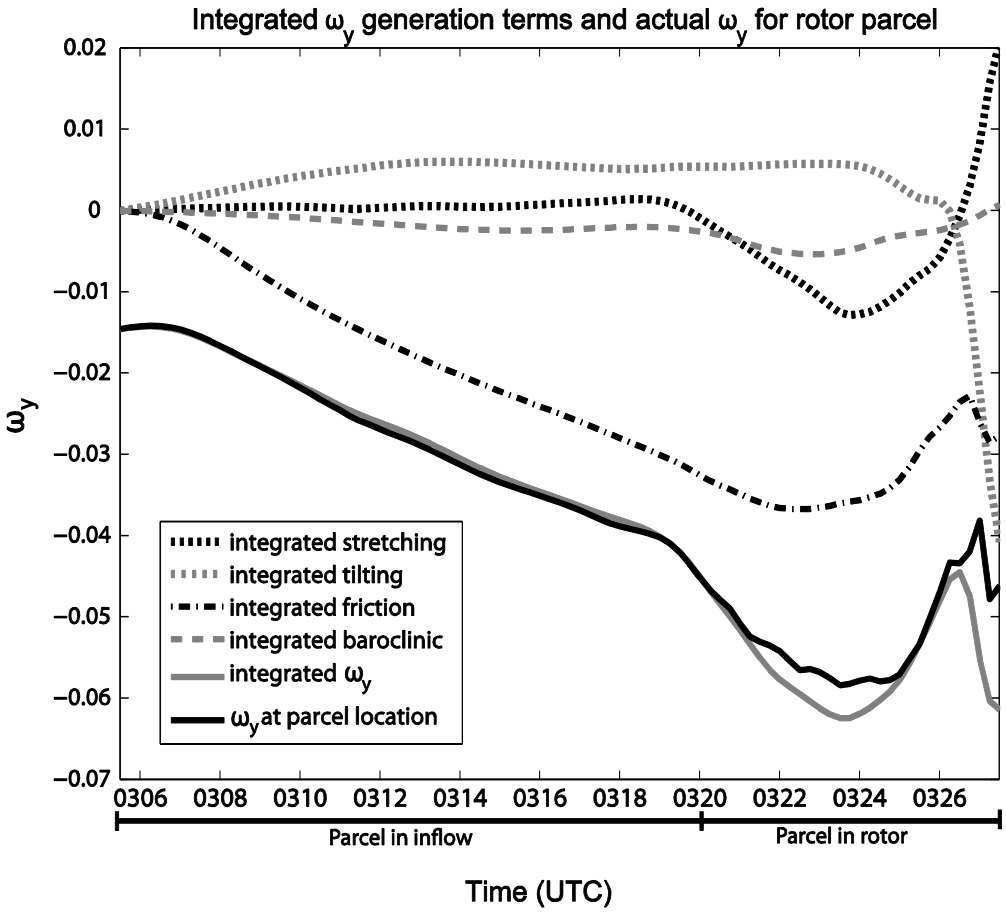

Fig. 3.13. Y-component vorticity budget for the parcel plotted in Fig. 3.12, but integrated backward in time until 0305:30 UTC. The parcel enters the rotor around 0320:00 UTC. The gray solid line is the sum of the time-integrated stretching (short dashed gray line), tilting (short dashed black line), frictional generation (alternating short-long black dashed line) and baroclinic generation (long dashed gray line). The solid black line represents y-component vorticity interpolated to the parcel location from the model grid at each time.

In order to confirm that surface drag is the cause of the rotor circulation, the 100-m simulation was re-run without the surface drag parameterization[9]. On the mesoscale, the simulation evolves in a similar manner to the experiment with surface drag, with an initial mesovortex developing and decaying, followed by the development of the Minco mesovortex (Fig. 3.14). However, closer examination shows that a rotor does not form, and time-height plots of maximum updraft and vertical vorticity reveal that there is no strong low-level updraft. As a result, there is no TLV in the no-drag experiment (Fig. 3.15). Instead, there is a long period of weaker vorticity associated with the broad rotation of the Minco mesovortex. This result strongly suggests that surface drag is the cause of the rotor and associated enhanced low-level updraft, implying that surface drag is critical to the TLV genesis in this case.

[9] A caveat here is, due to computational cost, the outer 400-m and 2-km domains were not re-run without surface drag. Thus, it must be assumed that impact of friction communicated to 100-m grid through the initial and boundary conditions is small. This assumption is likely valid because the features of interest are generally far from the lateral boundaries and most of the vorticity generated by friction in the 100-m experiment that included drag did not come from the initial condition, but rather was generated as the flow accelerated into the intensifying convective cell.

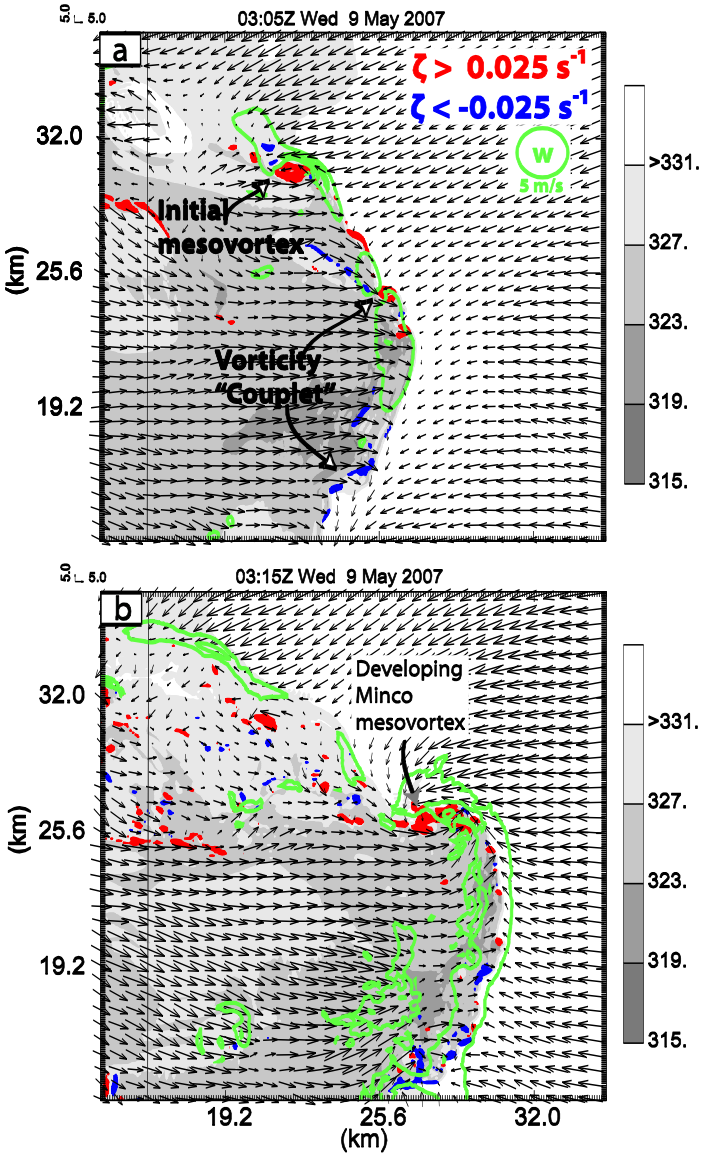

Fig. 3.14. As Fig. 3.2 but for the experiment with surface drag turned off and only at (a) 0305 UTC and (b) 0315 UTC.

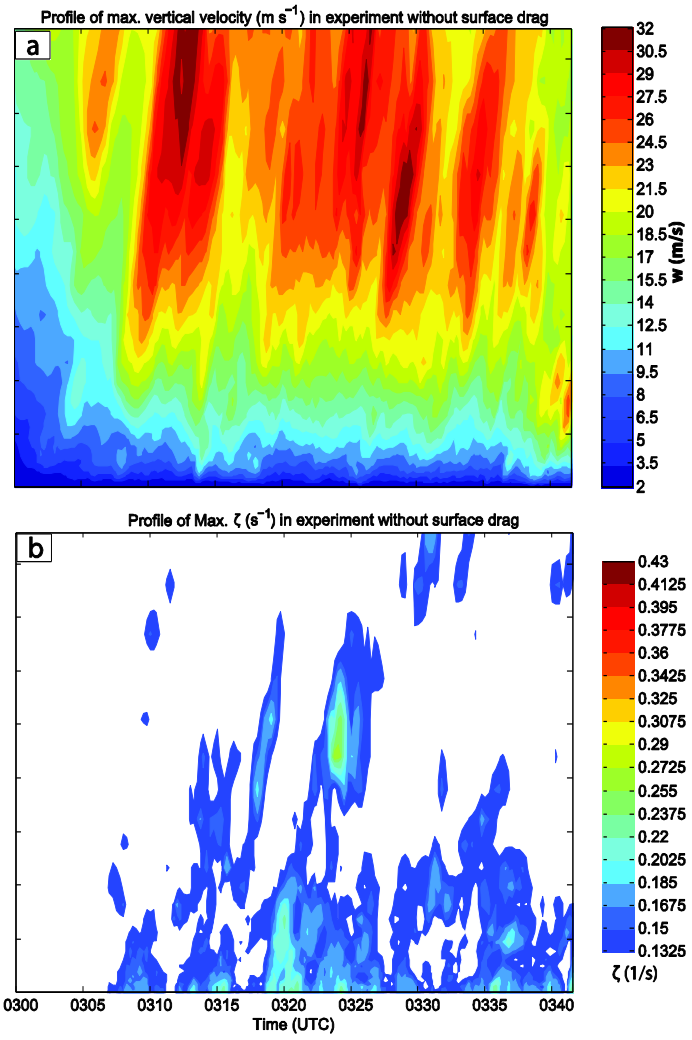

Fig. 3.15. As Fig. 3.6 but for the experiment with the surface drag parameterization turned off.

3.3.4 Analogy with rotors in the lee of mountains

Now that the importance of the rotor (and thus surface drag) in TLV genesis in this case has been established, an attempt is made to explain the mechanism by which surface drag is acting to create the rotor circulation. To do so, another atmospheric flow in which surface drag has been shown to result in the generation of rotors is examined. Namely, rotors that form on the lee slope of mountains associated with mountain wave

flows. Using idealized 2-D numerical simulations of stably stratified flow with and without surface drag, Doyle and Durran (2002) have shown that rotor formation in the lee of a mountain in a simulation with surface drag is the result of boundary layer separation that occurs as the flow turns upward into the updraft at the leading edge of the first lee-wave. Specifically, boundary layer separation occurs as the flow decelerates and is forced to rise by the adverse PGF associated with the pressure maxima beneath the lee-wave crest. As the boundary layer separates, the thin sheet of frictionally-generated vorticity near the surface is advected into the lee-wave and a rotor forms. Mountain wave simulations that do not include surface friction do not produce rotors; instead, they produce a stationary wave train that has substantially higher amplitude than the wave train in corresponding experiments that include surface friction. These results led Doyle and Durran (2002) to conclude that the rotors in their simulations formed via a synergistic interaction between boundary layer drag and trapped mountain lee-waves.

In order to compare the findings of the mountain rotor studies to our study, the following equivalencies between our study and the idealized mountain rotor scenario are noted:

(1) In both studies, there is a strong low-level wind maximum, beneath which boundary layer drag generates large values of horizontal vorticity (cf. Fig. 3.8b). In the mountain wave case, this vorticity maximum is caused by friction acting on the stably-stratified flow accelerating down the lee slope of the mountain. In our study, friction acting on the accelerating inflow east of the intensifying convective storm creates a similar vorticity maximum.

(2) In both studies, the atmosphere is stably stratified at low-levels. In the mountain wave case, this is specified in the initial conditions. In our case, the nocturnal nature of the event and earlier rainfall associated with the leading convective line of the MCS lead to stable stratification of the low-level inflow (Fig. 3.16a). The role of stable stratification in our case is to prevent parcels from continuing to accelerate buoyantly upward after being forced to rise upon encountering the FFGF. Instead, because of stable stratification, parcels descend and become concentrated to the rear of the FFGF.

(3) Both the mountain rotor and the rotor in our simulation form just downstream of an adverse PGF that leads to boundary layer separation. As mentioned above, in the mountain wave case, this adverse PGF is just upstream of and is caused by the pressure maxima present beneath each lee-wave crest. In our case, the inflow is forced to rise by an adverse PGF associated with the pressure maximum due to the gust front. This gust front is reinforced by the westerly momentum surge (Fig. 3.16a) produced as the earlier mesovortex dissipates. This reinforcing surge of westerly flow increases low-level convergence which, through the diagnostic perturbation pressure equation referred to above, implies an increase in the strength of the adverse PGF and is accompanied by the rapid development and intensification of the rotor circulation (Fig. 3.16b). Doyle and Durran (2002) noted that rotor intensity (which they measured by the strength of the reversed flow associated with the rotor) was proportional to the strength of the adverse PGF in corresponding experiments that did not include surface drag.

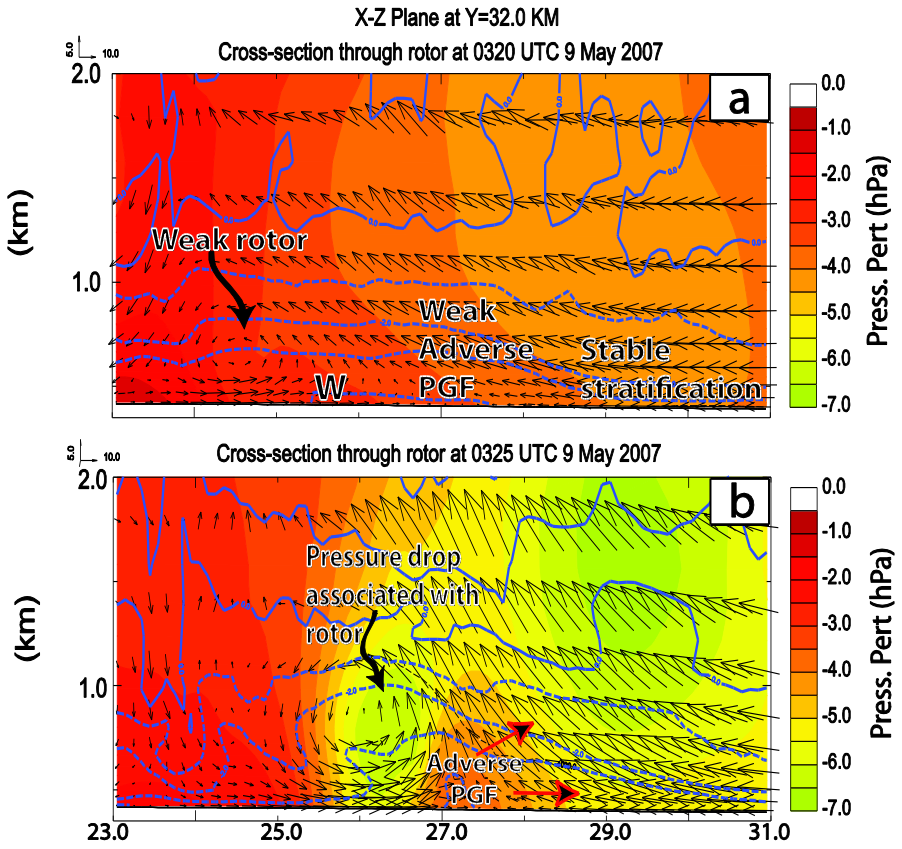

Fig. 3.16. Perturbation pressure (shaded, Pa), perturbation potential temperature (blue contours, K), and velocity in the plane of the cross-section (vectors, m s -1) at (a) 0320 UTC and (b) 0325 UTC 9 May 2007. The 'W' in (a) marks the leading edge of the westerly momentum surge associated with the decaying initial mesovortex. The red-outlined arrows in (b) give the sense of the PGF direction.

While the idealized 2D mountain rotor scenario and the rotor in our simulation share many similarities, there are also important differences. Most significantly, our simulation is three-dimensional and includes flow perturbations associated with a convective storm, rather than two-dimensional and homogenous as in Doyle and Durran (2002)[10]. More specifically, pressure gradient forces associated with the convective storm and the Minco mesovortex accelerate the flow along the rotor axis and into the TLV and Minco mesovortex, leading to the formation of only one rotor instead of the

[10] The impact of three-dimensionality was investigated in Doyle and Durran (2007), however, comparison with these results is even more difficult as three-dimensionality tends to accentuate the inherent differences between the 'flow over a mountain' and convective storm scenarios.

series of rotors that formed in the lee of the mountain in Doyle and Durran (2002). Nonetheless, the striking similarities in the formation of the rotor, environmental conditions, and geometry of the problem (compare Fig. 3.17a to Fig. 3.17b) strongly suggests that the basic rotor formation mechanism in our simulation is largely analogous to that of the two-dimensional mountain simulations.

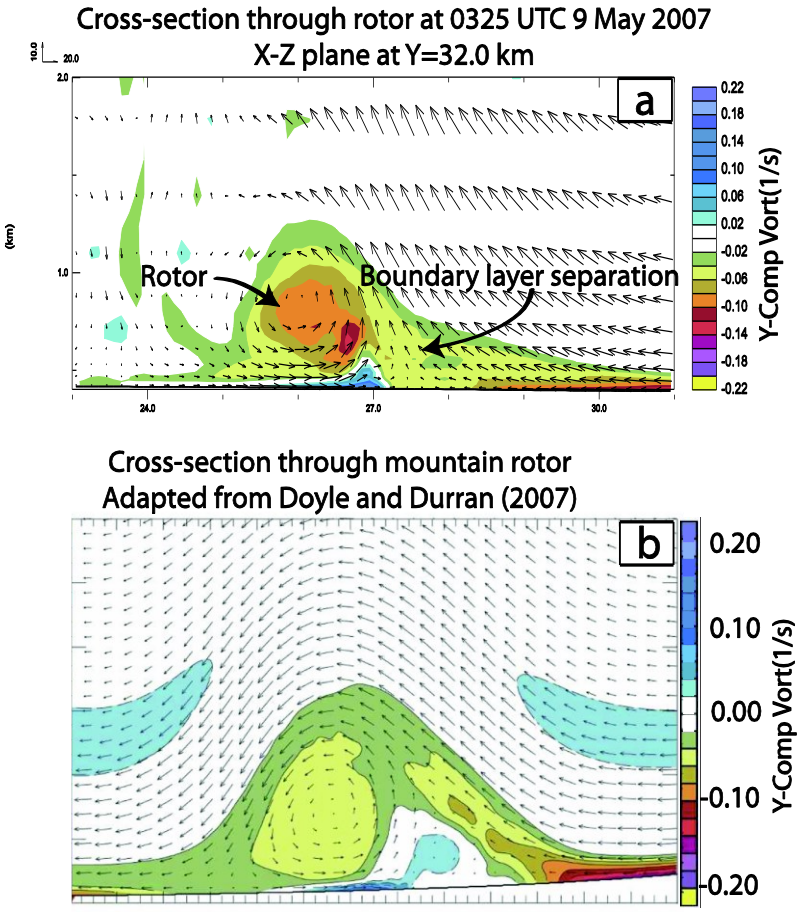

Fig. 3.17. Y-component vorticity (shaded, s-1) and velocity vectors in the plane of the cross-section (vectors, m s-1) from (a) an XZ crossection through the rotor at 0325 UTC and (b) from a XZ cross-section through a simulated rotor in the lee of a mountain [adapted from Doyle and Durran (2007)]. In (b), the original figure of Doyle and Durran (2007) has been reflected about the x-axis in order to directly compare with the flow geometry of the rotor in the 9 May 2007 case.

3.3.5 The role of surface friction in TLV genesis

It is important to make a distinction between the role of friction in TLV genesis presented herein and the role of surface drag in tornado maximum wind speed discussed in Fiedler and Rotunno (1986), Fiedler (1994), Trapp and Fiedler (1995), Grasso and Cotton (1995), and Lewellen et al. (1997). In those studies, surface drag was found to be responsible for producing a maximum wind speed in tornadoes that exceeded the so-called "thermodynamic speed limit". This occurred because surface drag led to the creation of an axial jet and supercritical end-wall vortex that made it more difficult for vortex breakdown to penetrate to the surface. Thus, these studies primarily investigated the impact of surface drag on the tornado and sub-tornado scale. This differs greatly from our study, in which surface drag has a substantial impact at the mesovortex scale (dramatically enhancing the mesovortex-scale updraft at low-levels). It is possible that surface drag is also acting on the tornado and sub-tornado scale in our simulation; however, this is not the focus of the present paper.

In addition to clarifying the difference between the role of surface drag on the tornado scale and the role of surface drag on the storm and mesovortex scale, we also want to expand on the role surface drag is playing in this case. In particular, it is emphasized that the primary role of the rotor in TLV genesis is the concentration and stretching of vorticity by the intense low-level updraft, not the generation of vertical vorticity from the tilting of horizontal vorticity within the rotor. Thus, a small area of intense vertical vorticity that forms within the rotor a few minutes before the TLV is examined (see the vorticity maximum near x=28.3 km, y=30.4 km in Fig. 3.4a). This vorticity center amplified dramatically as it moved into the intense low-level updraft

(not shown). However, the small vorticity center then rapidly moves away from the ascending branch of the rotor and weakens (Fig. 3.4b,c). A TLV does not form until the larger area of vertical vorticity associated with the Minco mesovortex becomes coincident with the rotor. After the dissipation of the TLV, there are several brief, but intense vorticity centers that develop near, and move through the rotor (e.g., the vorticity maximum marked by a 'Y' in Fig. 3.5c). However, the strong downdraft in the eastern portion of the Minco mesovortex (see Fig. 3.3a) combined with the axial downdraft forced by the TLV has substantially broadened the mesovortex circulation. As such, even though the low-level updraft associated with the rotor remains intense, it is unable to re-concentrate the broad mesovortex, and no additional TLVs form in association with the small vorticity centers. Thus, the rotor and associated updraft appear to be necessary, but not sufficient, conditions for TLV genesis in the present case.

3.3.6 Summary and conceptual model

Analysis of the numerical simulations presented herein suggests a multi-step process in the development and intensification of the TLV associated with the Minco mesovortex. Fig. 3.18 presents a schematic of this multi-step process (for the case under consideration) and can be summarized as follows:

I) An updraft that forms at the leading of the gust front bulge tilts baroclinically generated southward pointing vortex lines upward, forming a vortex arch. Areas of cyclonic and anti-cyclonic vorticity straddle the updraft, with cyclonic (anticyclonic) rotation on the north (south) side.

II) The cyclonic vorticity intensifies along with the overall convective storm, given preference for intensification over the anti-cyclonic circulation by the presence and concentration of the background cyclonic vorticity. This intensification leads to increased low-level inflow ahead of the gust front and the generation of strong horizontal vorticity near the surface caused by surface drag.

III) The FFGF is reinforced from the rear by a surge of westerly momentum due to downdrafts from an earlier dissipating mesovortex. A horizontal rotor circulation develops and rapidly intensifies as low-level inflow and associated strong near-surface horizontal vorticity is forced to rise upon encountering the FFGF. Concurrently, the upward branch of the rotor intensifies dramatically leading to the development of an intense low-level updraft.

IV) Tornado-like vortex genesis occurs as vorticity associated with the mesovortex is concentrated and stretched by the intense low-level updraft. The vortex dissipates when a downward-directed pressure gradient force develops, inducing a downdraft at the vortex center and broadening the vortex.

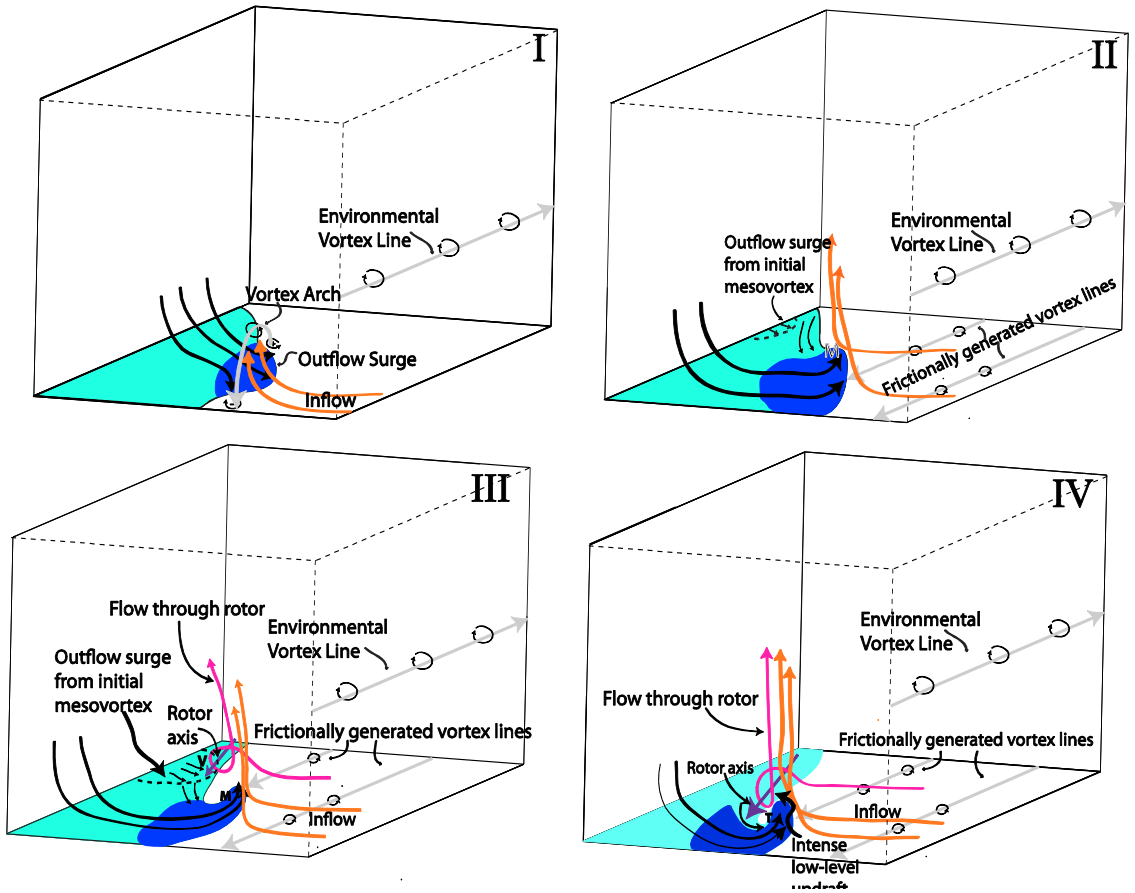

Fig. 3.18. Schematic of four-stage process leading up to TLV genesis. Vertical vorticity couplet development is depicted in (I). (II) shows the development of the of dominant cyclonic Minco mesovortex and associated development of the frictionally-generated horizontal vorticity. (III) illustrates the development of the rotor. TLV genesis is shown in (IV). The cyan shading represents the cold pool. The dark blue shading represents the cold air within the cold pool bulge. Black arrows represent the surface flow trajectories. The orange arrows represent trajectories which enter the main updraft. The purple arrow in (III) and (IV) marks the horizontal rotor axis. The magenta arrows represent parcel trajectories that enter the rotor. Light gray vectors are idealized vortex lines. The 'M' represents the location of the Minco mesovortex. The dotted curves in (II) and (III) mark the location of the enhanced westerly momentum associated with the dissipation of the initial mesovortex. The 'v' behind the outflow surge from the initial mesovortex in (III) marks the location of the small area of vertical vorticity moving through the rotor. The 'T' in (IV) marks the location of the TLV.

3.4 Summary and conclusions

Although little is known about the development of quasi-linear convective system (QLCS) tornadoes, observations indicate that they tend to form in close association with strong, long-lived mesovortices. In this chapter, results were presented from a numerical study of one such strong, long-lived mesovortex that occurred in association with a MCS and line-end vortex on 8-9 May 2007 in central Oklahoma. The simulation was run using the ARPS model with a high-resolution (100-m grid spacing) domain nested within two larger, lower-resolution (2 km and 400 m grid spacing) domains. The two lower-resolution simulations were initialized by assimilating data from both operational WSR-88D radars and from the high-density experimental CASA radar network, as well as data from conventional sources.

The simulated mesovortex was generated in a manner consistent with the development mechanism for mesovortex couplets proposed by Atkins and St. Laurent (2009b). Namely, cyclonic and anticyclonic vortex couplets formed on either side of an enhanced updraft associated with a bulging gust front. The cyclonic member of the vortex couplets strengthened and persisted for ~ 1 hr. The simulated mesovortex produced a strong low-level sub-mesovortex scale tornado-like vortex (TLV). Closer inspection of the genesis of this TLV showed that a strong low-level updraft was critical for the convergence and amplification of the vertical vorticity associated with this mesovortex to tornado strength. This low-level updraft was found to be the upward branch of a strong horizontal rotor located just to the northwest of the TLV. The cause of the rotor was shown to be the interaction between the convective outflow and

frictionally-generated near-ground horizontal vorticity underneath enhanced low-level storm inflow.

The results presented herein come with a common caveat to studies focusing on high-resolution numerical simulations; that is, they are only explicitly valid for this one case and may be limited by the experiment design (resolution, etc.). However, an important aspect of this study is that, as far as we know, it is the first to highlight the existence and importance of the rotor circulation and show a possible substantial impact of surface drag on the storm and sub-storm scale [rather than on the sub-tornado scale (e.g., Fiedler 1994)]. It is also one of few studies of this type whose simulated storms are initialized using real data and in which the model simulations verify reasonably with observations. Our findings are also consistent with earlier studies that showed tornadoes within QLCSs are typically associated with strong, long-lived mesovortices. In our study, a critical ingredient for rotor development is the frictional generation of near-surface horizontal vorticity associated with the intensification of the inflow into the Minco mesovortex. This flow profile takes about 10 min to develop after the genesis of the Minco mesovortex. We speculate that weaker, shorter lived mesovortices may dissipate before a rotor-circulation develops, which could preclude tornadogenesis.

The important role of surface drag and the rotor circulation raises a number of questions that will be the focus of future work. Most importantly, how common is a rotor feature in tornadic mesovortices associated with QLCSs? It seems probable that the environment of our simulation is at least somewhat typical of environments associated with many QLCSs. Is a similar rotor type feature common and/or important in supercell tornadogenesis? Dowell and Bluestein (1997) found very strong shear in

wind observations from a 440-m tall instrumented tower in near-updraft supercell inflow (see their Fig. 18). They speculated that this shear may have been caused by stretching of baroclinic vorticity associated with anvil shading. However, numerical simulations investigating the impact of anvil shading (Frame and Markowski 2010) showed that a similar shear profile was the result of surface drag slowing the near-ground flow. Additionally, an examination of dual-Doppler and mobile mesonet data from the Goshen County, Wyoming, 5 June 2009 supercell intercepted during the VORTEX2 project suggests that surface drag cannot be ruled out as a contributor to positive circulation (Markowski 2012a, b). It seems probable that the only way to answer these questions will be through additional high-resolution simulations of different cases as, even in targeted field campaigns, near ground (~200 m AGL or below) high-resolution observations are generally not available. One such simulation is the subject of the following chapter.

Chapter 4: Tornadogenesis in the Simulated 8 May 2003 Oklahoma City Tornadic Supercell

In the previous chapter, tornadogenesis in a high-resolution numerical simulation of a QLCS was examined and explained. However, as noted in that chapter, most tornadoes occur in association with supercell thunderstorms. To that end, the focus of this dissertation now shifts to study a high-resolution simulation of one such event that occurred on 8 May 2003 in the Oklahoma City metro area. This simulation is investigated thoroughly with hopes of discovering the important processes and steps leading up to tornadogenesis in the simulated 8 May 2003 Oklahoma City supercell.

4.1 The 8 May 2003 Oklahoma City tornadic supercell

The 8 May 2003 Oklahoma City supercell (hereafter, the OKC supercell) formed in the middle of an unusually long tornado outbreak that occurred over much of the central US from 3-11 May 2003, producing 361 tornadoes (Hamill et al. 2005). Hamill et al. (2005) studied this extended outbreak and found that it was the result of a persistent large scale trough over the southwest US. Intermittent shortwave troughs moving through the longwave trough led to daily tornado outbreaks from the Central and Southern Plains into the mid-Atlantic region. A notable aspect of the extended outbreak was the lack of any strong cold fronts within the affected area, meaning that warm, moist air from the gulf was continually present, leading to a favorable environment for tornadic supercells when combined with the persistent longwave trough.

The OKC storm initiated along a dryline in central Oklahoma around 2100 UTC 8 May 2003. The storm formed in a very favorable environment for tornadic supercells,

with large mixed-layer CAPE (> 3800 J kg^{-1}) and SREH of > 450 m^2 s^{-2} [see fig. 3 in Romine et al. (2008)]. The OKC storm rapidly took on supercell characteristics and produced two weak, short-lived tornadoes just southwest of Moore, OK between 2200 and 2208 UTC. At 2210 UTC, a third tornado formed on the west side of Moore and persisted for 28 min, producing widespread F2-F3 and localized F4 damage along it's ~27 km track (Fig. 2.1). Following the dissipation of this tornado, the storm began to weaken with no additional tornadoes. The OKC storm dissipated shortly after 0000 UTC 9 May 2003.

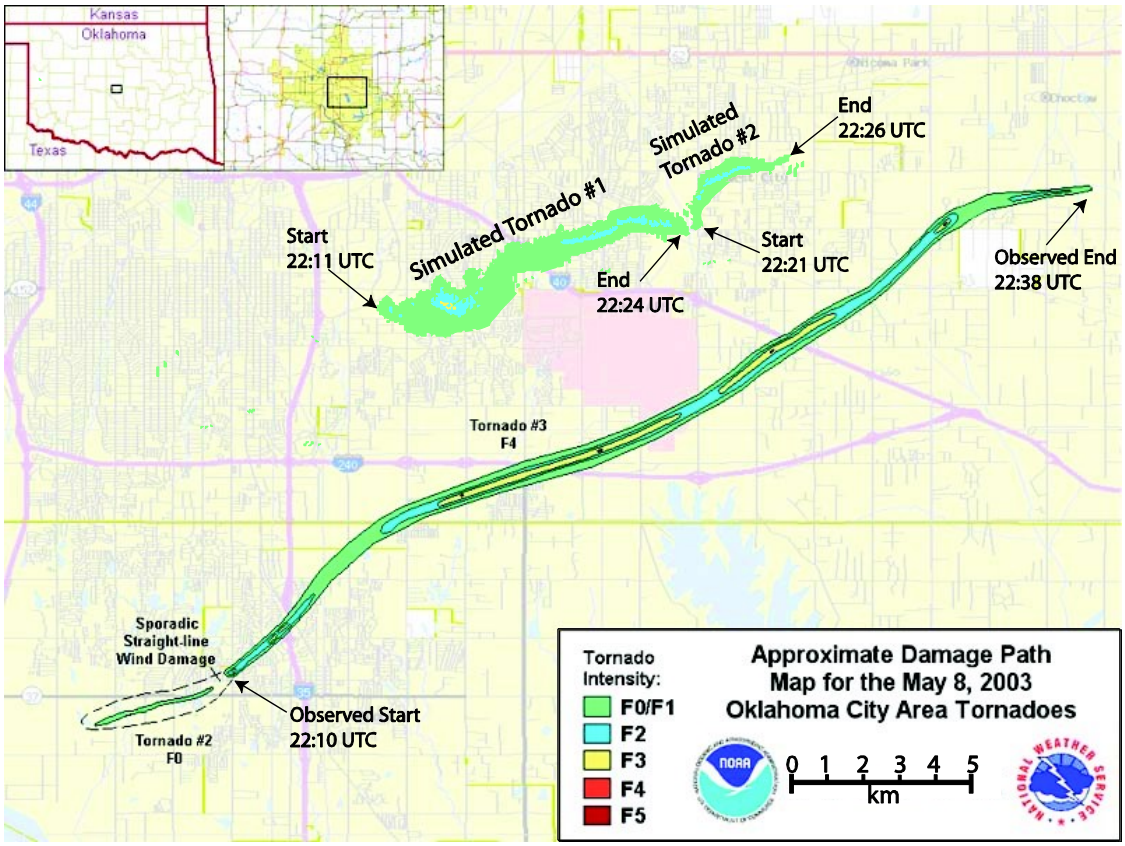

Fig. 4.1. Map of the south Oklahoma City area overlaid with the track of the simulated tornadoes and the observed tornadoes on 8 May 2003. Image is adapted from the NWS Norman's website: http://www.srh.noaa.gov/oun/?n=events-20030508

Owing to its proximity to a major metropolitan area and the high observation density present in Oklahoma, varying aspects of the OKC storm have been examined

and discussed in several past studies (Ryzhkov et al. 2005; Hu and Xue 2007; Liu et al. 2007; Romine et al. 2008; Dowell and Wicker 2009; Dowell et al. 2011; Gao and Stensrud 2012). For the most part, these studies use data from the OKC storm as a test or demonstration case for a variety of topics including: polarimetric radar data analysis (e.g., Ryzhkov et al. 2005; Romine et al. 2008; Kumjian and Ryzhkov 2009), data assimilation techniques (e.g., Dowell and Wicker 2009; Dowell et al. 2011; Gao and Stensrud 2012), tornado detection/characterization algorithms (Liu et al. 2007; Wang et al. 2008; Potvin et al. 2009), and advection correction techniques (Shapiro et al. 2010).

Using polarimetric radar observations, Romine et al. (2008) performed the most detailed dynamical analysis of the OKC storm. However, their study was mainly focused on the behavior of the polarimetric variables and possible microphysical implications. One notable aspect of Romine et al. (2008) was the observation that the FFGF was associated with meager temperature perturbations, with much larger cold perturbations behind the RFGF. On the other hand, Romine et al. (2008) reaches this conclusion based on data from only two stationary surface observation sites which, especially considering the results presented in Lee et al. (2012), likely means that thermodynamic structure of the cold pool was largely unresolved.

The present study aims to explore the dynamical processes behind tornadogenesis in the OKC storm by examining a high-resolution (50-m horizontal grid-spacing) simulation of the storm initialized via assimilation of real data. The remainder of this chapter is organized as follows: Section 4.2 discusses the numerical simulation and data assimilation configurations. An overview of the simulated OKC storm and associated tornadoes is provided in section 4.3. Section 4.4 presents a detailed analysis

of the processes responsible for tornadogenesis in the simulation. A summary is provided in section 4.5.

4.2 Experiment design

As in the simulation of the 8-9 May 2007 tornadic convective system presented in chapter 3, the present simulation employs multiple (in this simulation, four) one-way nested grids in order to capture the evolution of the 8 May 2003 tornado outbreak on a variety of scales (Fig. 4.2). The outermost grid has 9-km grid spacing, covers a 2300 km x 2300 km area, and assimilates hourly conventional data (including Oklahoma Mesonet data) using the ARPS 3DVAR between 1800 UTC 8 May 2003 and 0000 UTC 9 May 2003. Rawinsonde data are also assimilated at 1800 and 0000 UTC. The 1800 UTC NAM is used to provide initial conditions at 1800 UTC and boundary conditions every 3 hours. A 1-km grid spacing domain that covers a 280 km x 280 km area is nested within the 9-km domain. Five-minute data assimilation cycles are performed over a 70 min period beginning at 2030 UTC 8 May 2003. Radial velocity data from the WSR-88D KTLX are assimilated during these cycles via the ARPS 3DVAR. KTLX reflectivity data are assimilated using a complex cloud analysis package.

Two very high-resolution domains are nested within the 1-km domain. The first has 100-m grid spacing, covers a 160 km x 120 km area, and begins a 60-min forecast at 2140 UTC, obtaining initial and boundary conditions from the 1-km domain. A 50-m grid spacing domain that covers an 80 km x 60 km area is nested within the 100-m simulation. A 40-min simulation is run on the 50-m domain beginning at 2200 UTC. No data assimilation is performed on the 100-m and 50-m grid-spacing domains. All

four model domains use a stretched vertical coordinate with 53 vertical levels and a minimum grid-spacing of 20 m near the model ground.

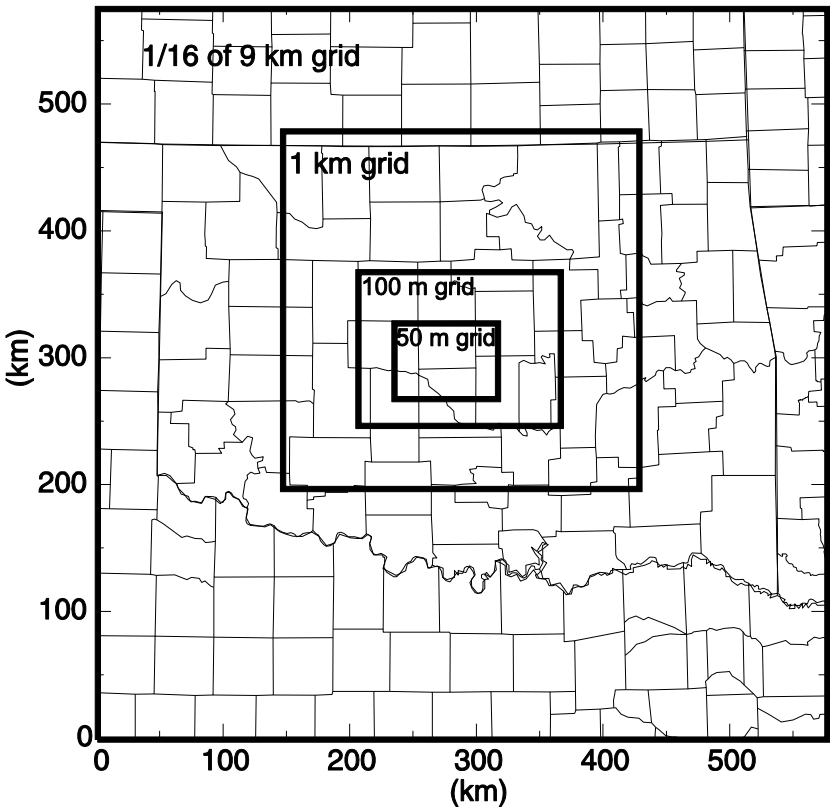

Fig. 4.2. Map of the 1/16 of 9 km grid-spacing simulation domain with black squares marking the boundaries of 1-km, 100-m, and 50-m grid spacing domains. Image courtesy of Ming Hu.

Model configurations for the 100-m and 50-m grid spacing simulations include: Lin 3-ice microphysics with the rain intercept parameter kept at the default value of 8 x 10^6 m^{-4}, fourth-order advection in the horizontal and vertical, a rigid top boundary condition with a wave absorbing layer beginning at 12 km AGL, fourth-order computational mixing, a 1.5-order TKE-based subgrid-scale turbulent mixing scheme and PBL parameterization. Surface fluxes are determined according to stability-dependent drag coefficients. The Coriolis parameter is latitude dependent and includes

the effect of earth curvature. A two-layer soil model is used that is based on Noilhan and Planton (1989). Because the focus of the present study is on the dynamical processes responsible for tornadogenesis in the OKC storm, the remainder of this chapter is focused on the 50-m grid spacing simulation.

4.3 Simulation overview

In this section, the general evolution of the 8 May 2003 simulation is discussed. This discussion will focus on introducing the important features in the simulated OKC storm. A more detailed analysis of the dynamics responsible for tornadogenesis in this simulation is presented in section 4.4.

The simulation begins at 22:00 UTC with a large cold pool at low-levels in the western portion of the model domain (Fig. 4.3a). The leading edge of the cold pool is oriented in the north-south direction. The make-up of the southern portion of the cold pool is initially very heterogeneous, with several warm and cold pockets. With time, the cold pool becomes more organized and homogeneous with the development of rear and forward flank gust fronts by 22:06 (Fig. 4.3b). To the northwest of the RFGF, an internal RFD surge has formed and is moving to the south.

The internal RFD surge behind the RFGF is associated with several small vorticity maxima (Fig. 4.3b). None of these maxima organize into a tornado strength vortex. Over the next couple of minutes, two small vertical vorticity maxima form in the vicinity of the RFGF. The first vorticity maximum (V1) forms around 22:07:30 (Fig. 4.4a) and intensifies while moving northeast, north, and finally slightly to the west (Fig. 4.4b,c). The second vorticity maximum (V2) initially forms around 22:08 UTC (Fig. 4.4b) to the north of V1 and remains stationary. As V1 moves to the north and

west it combines with V2 to create a pre-tornadic vortex (PTV) around 22:09:30 UTC (Fig. 4.4c,d). The PTV is fairly intense (in terms of maximum vorticity values), but is compact with winds weaker than tornado strength.

Concurrent with the development of the PTV, an internal RFD surge begins to overtake the FFGF (Fig. 4.4c,d). This internal RFD surge originated at about 22:06 UTC about 5 km north of the PTV and is a different surge from the one shown in Fig. 4.3b. The air behind the internal RFD surge is relatively cold (Fig. 4.4d), associated with a simulated reflectivity maximum (not shown), and backward trajectory analysis suggests that this surge is composed of air that originated a few km above the surface (not shown). All of this suggests that the internal RFD surge is the result of a downdraft that was caused by water loading and evaporation in the core of the OKC supercell. The internal surge rapidly moves to the southeast and approaches the PTV around 22:10 UTC (Fig. 4.5a). A few small vorticity maxima are present along the leading edge of the internal surge, with one maximum in particular (V3) appearing to merge with the PTV (Fig. 4.5b,c). As V3 merges with the PTV, tornadogenesis occurs rapidly around 22:11 UTC (Fig. 4.5d). The simulated tornado (hereafter, tornado 1) moves to the east-northeast at about 15-20 m/s. Maximum winds in the tornado exceed 70 m s^{-1} on its south side.

Fig. 4.6 shows the evolution of tornado 1 from genesis to just before dissipation (22:11-22:24 UTC) and can be summarized as follows: After forming, the tornado maintains its intensity for about four minutes. During this period occasional peaks in intensity are associated with secondary vortices embedded within the tornado (e.g., Lewellen et al. 1997). The tornado then briefly becomes two-celled and weakens

rapidly as an axial downdraft develops and reaches the surface (not shown). After about one minute, this weakening trend ceases and the tornado re-organizes about 1 km north. The tornado maintains its intensity for about seven minutes (again becoming two-celled), before dissipating well to the rear of the RFGF. Dissipation occurs fairly quickly, with strong near-surface divergence again associated with a strong downdraft within the circulation (not shown).

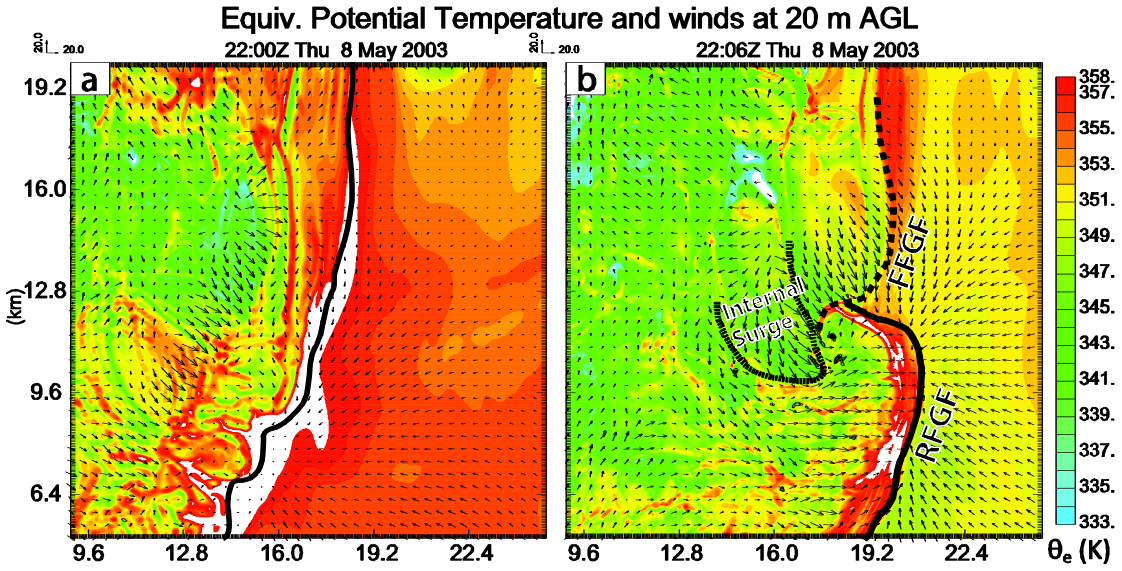

Fig. 4.3. Equivalent potential temperature (shaded, K) and horizontal wind vectors (m s^{-1}) at 20 m AGL, at (a) 2200 UTC and (b) 2206 UTC 8 May 2003. In (b) the locations of the locations of the RFGF (solid black line), FFGF (dashed black line), and an internal outflow surge (short dashed line) are marked.

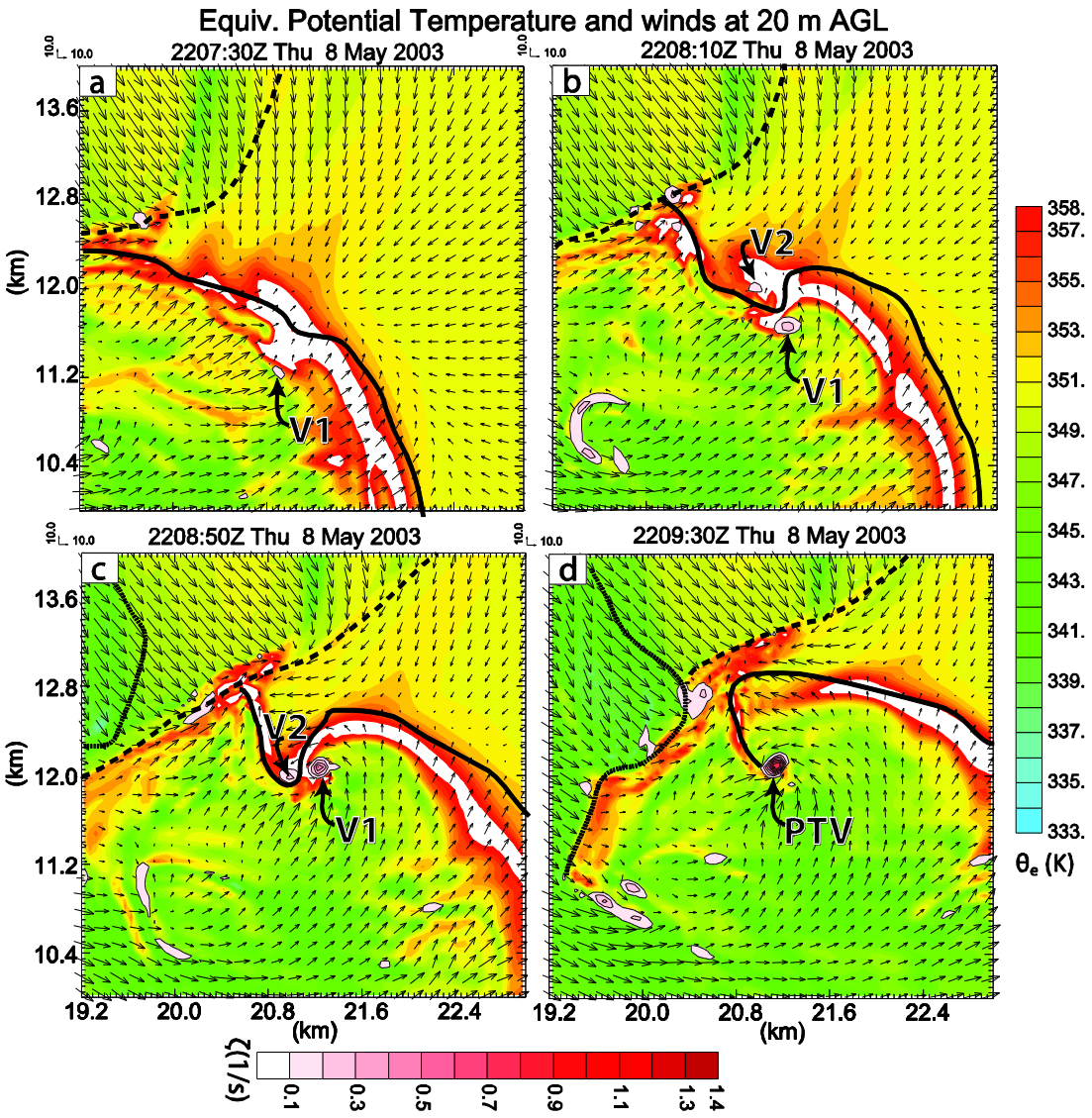

Fig. 4.4. Equivalent potential temperature (shaded, K), horizontal wind vectors (m s^{-1}) and vertical vorticity (shaded in red hues, starting at 0.1 s^{-1}) at 20 m AGL at (a) 2207:30 UTC, (b) 2208:10 UTC, (c) 2208:50 UTC, and (d) 2209:30 UTC 8 May 2003. Gust fronts are denoted with the same convention as Fig. 4.3.

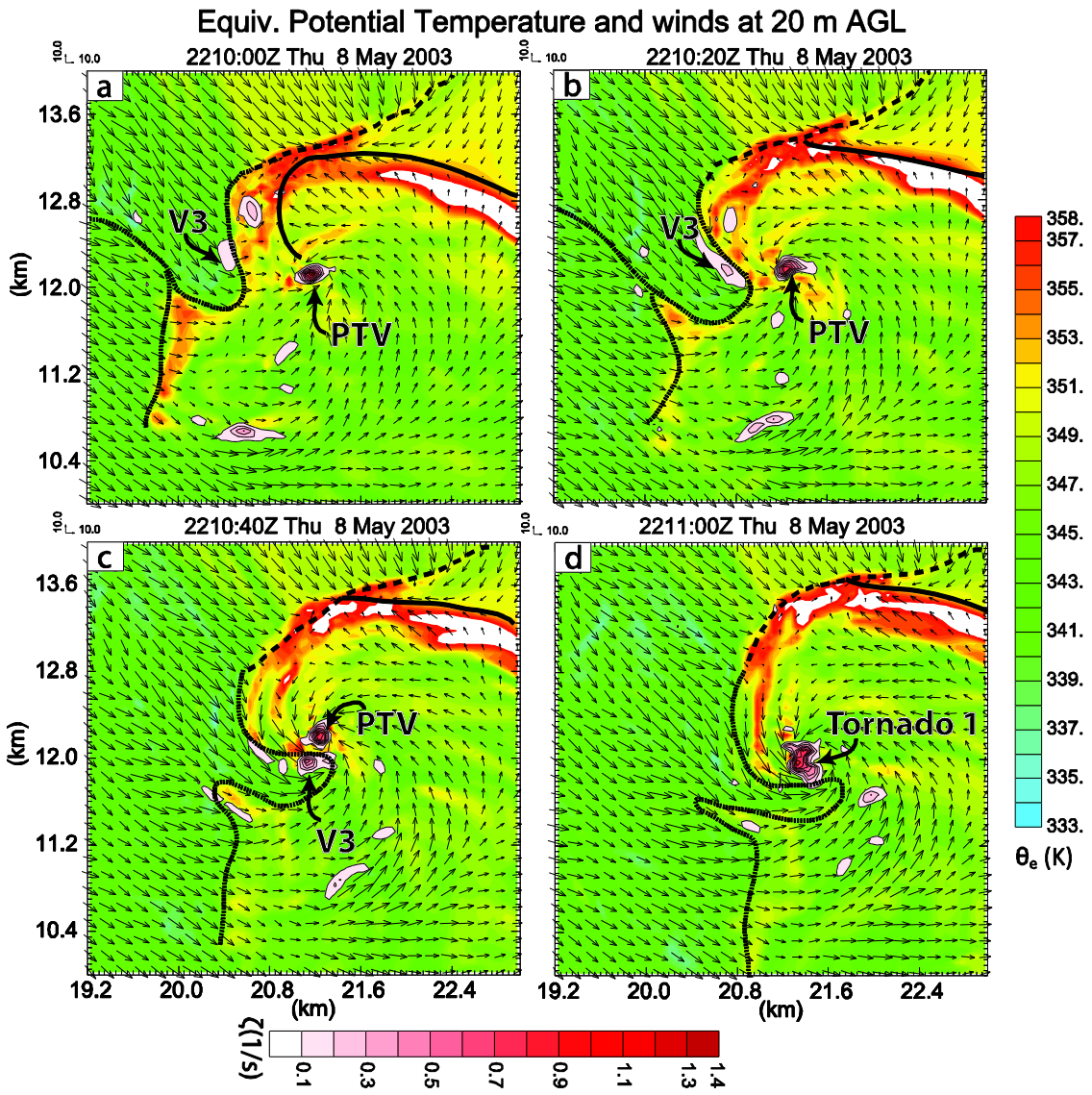

Fig. 4.5. As Fig. 4.4 but at (a) 2210:00 UTC, (b) 2210:20 UTC, (c) 2210:40 UTC, and (d) 2211:00 UTC 8 May 2003.

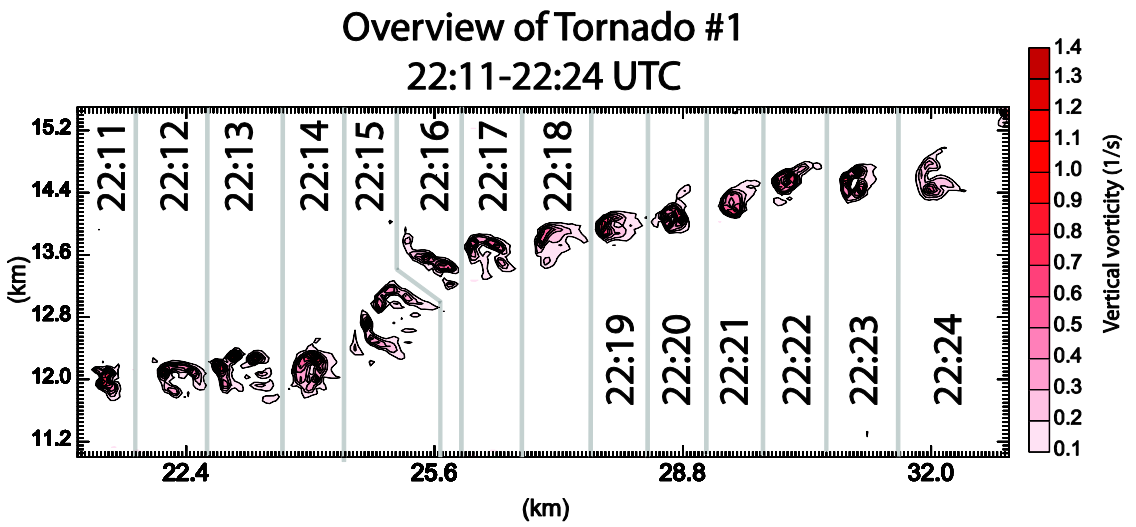

Fig. 4.6. Overview of the vertical vorticity (shaded > 0.1 s^{-1}) at 20 m AGL for tornado 1 plotted each minute between 2211 and 2224 UTC 8 May 2003. Gray lines are added for clarity to indicate which vorticity is associated with which time.

A few km to the east of the first tornado another vertical vorticity maximum (V4) forms just in advance of the RFGF around 22:17 (Fig. 4.7a,b). V4 initially forms as a new updraft that has developed in the inflow region of the OKC storm encounters the RFGF. V4 intensifies rapidly while moving north along the RFGF (Fig. 4.7c). As the RFGF occludes, V4 continues to strengthen and the wind associated with it reaches tornadic strength (hereafter, tornado 2) by 22:20 UTC (Fig. 4.7d). Tornado 2 moves briefly northward and then east-northeast at about 20 m s^{-1} along the FFGF at the occlusion point with the RFGF. Tornado 2 is smaller than tornado 1 and, unlike tornado 1, tornado 2 consists of one vorticity maximum through its entire lifetime. Tornado 2 rapidly weakens below tornado strength after 22:25 UTC and dissipates around 22:27 UTC. Fig. 4.8 plots the vertical vorticity associated with tornado 2 from the formation of V4 to the dissipation of tornado 2 (22:18 – 22:27 UTC). Following the dissipation of tornado 2, the OKC supercell becomes outflow dominant and no additional tornadoes form.

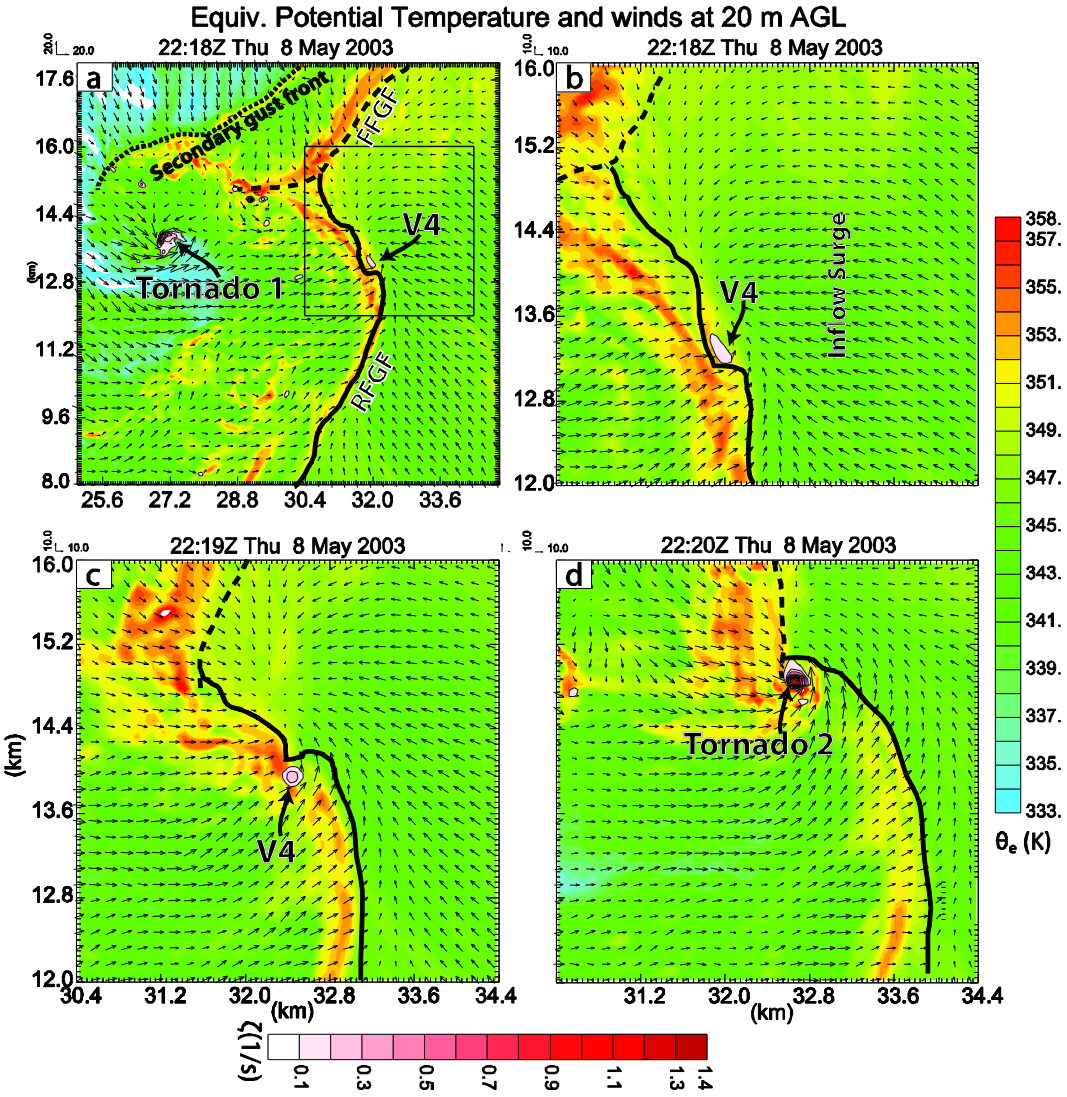

Fig. 4.7. As Fig. 4.4 but for (a) 2218 UTC, and for a zoomed in section of (a) at (b) 2218 UTC, (c) 2219 UTC, and (d) 2220 UTC. The rectangle in (a) marks the boundary of the area plotted in (b-d).

An overview of the simulated tornado tracks of both tornadoes is provided in Fig. 4.1. Note that, while the simulated tornado track is shorter and the tornado is somewhat weaker, tornado 1 is within a few km of the observed location of the OKC tornado (observed tornado #3 in Fig. 4.1). In addition, while tornado 2 is spurious, in that an additional tornado was not observed after the dissipation of the OKC tornado,

tornado 2 occurs along the same general path as tornado 1. Given the close spatio-temporal proximity to tornado 1, it is possible (though, perhaps unlikely) that in reality an additional tornado could have occurred and been recorded as the same tornado rather than a separate tornado. Seeing as this possibility cannot be entirely ruled out, the processes behind the generation of tornado 2 are examined in the following section. However, given the possibility that tornado 2 is spurious, this study focuses more heavily on tornado 1.

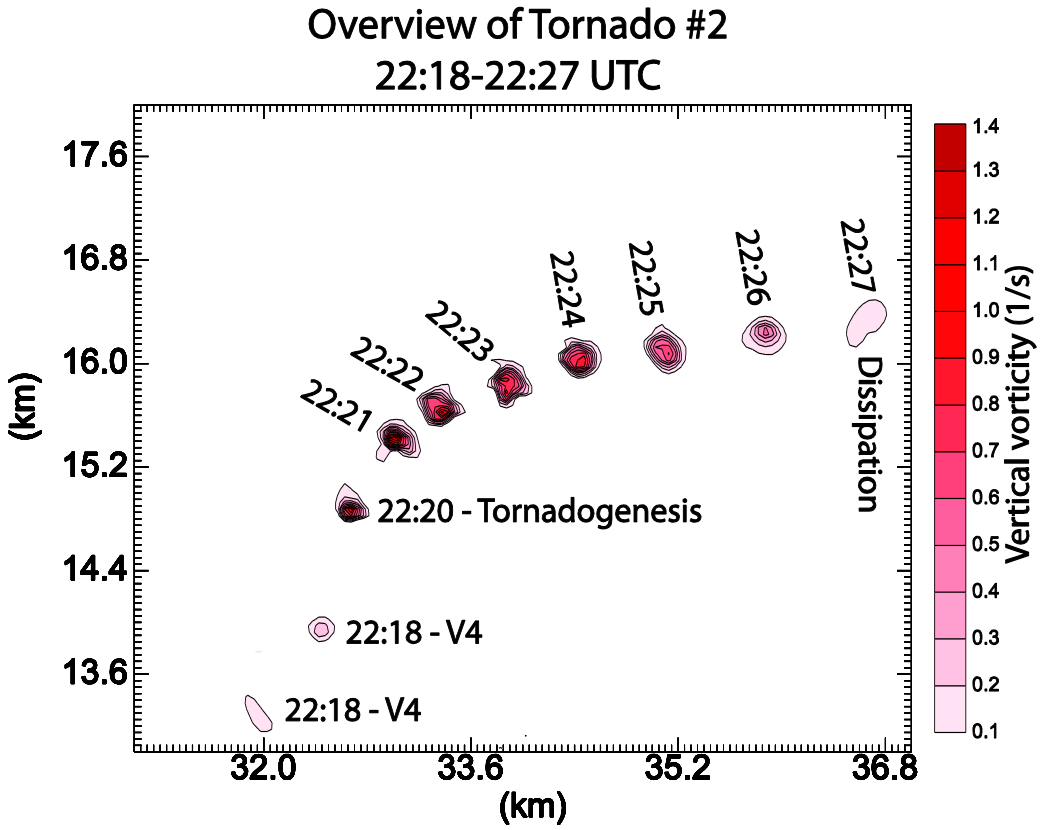

Fig. 4.8. As Fig. 4.6 but for tornado 2 between 2218 and 2227 UTC. Gray lines are omitted because the vorticity pattern is less complicated than for tornado 1.

4.4. Detailed analysis of tornadogenesis

Now that a general overview of the evolution of the simulation has been provided, a more detailed analysis is performed to elucidate the important processes and

features responsible for tornadogenesis in the OKC storm simulation. Because they develop quite differently (and tornado 2 may be spurious), tornado 1 and 2 are discussed separately.

4.4.1 Development of the first tornado

As described above, tornado 1 developed as a result of the merger of at least three different areas of vertical vorticity (V1-V3). Each of these vorticity centers formed under different circumstances and in different areas of the storm. In order to determine the origin of V1-V3, detailed backward trajectory, vorticity budget, and vortex line analyses were performed for each vorticity maximum.

The first vorticity maximum to form that was directly related to tornado 1 in the OKC storm simulation was V1. Given the RFGF relative position of V1, one may be tempted to implicate the tilting of baroclinically generated vorticity in the development of V1 (e.g., Markowski et al. 2008). However, closer inspection of the horizontal vorticity vectors near V1 reveals large ($> 0.1\ s^{-1}$) mainly northward -pointing vorticity at low-levels behind the RFGF (Fig. 4.9). This orientation of the horizontal vorticity vectors is opposite to that which would be expected if the vorticity was generated baroclinically along the RFGF. Instead, the orientation of the horizontal vorticity is more consistent with it originating as a result of surface drag. Moreover, rather than being 'arched' over the RFD, vortex lines that enter V1 instead are mainly horizontal at low-levels behind the RFGF before rising about 100 m in the updraft along the northern portion of the RFGF (Fig. 4.9). Vortex lines then descend and can be linked with a weak area of anti-cyclonic vorticity to the northwest of V1.

To verify that surface drag is responsible for generating the northward-pointing horizontal vorticity, horizontal vorticity budget calculations are performed along backward trajectories that terminate in and around V1. A representative trajectory is plotted in Fig. 4.10. Vorticity budget calculations along this trajectory (Fig. 4.11) indeed confirm that frictionally generated vorticity is the dominant term in the vorticity budget. Specifically, as the parcel travels southward near the ground, x-component vorticity is generated by surface drag. The parcel then rises about 200 m before descending in the RFD. Following this descent, the parcel accelerates to the east and large y-component vorticity is generated via drag. Vertical vorticity budget calculations show that this horizontal vorticity is tilted and then stretched to generate V1 (Fig. 4.11c).

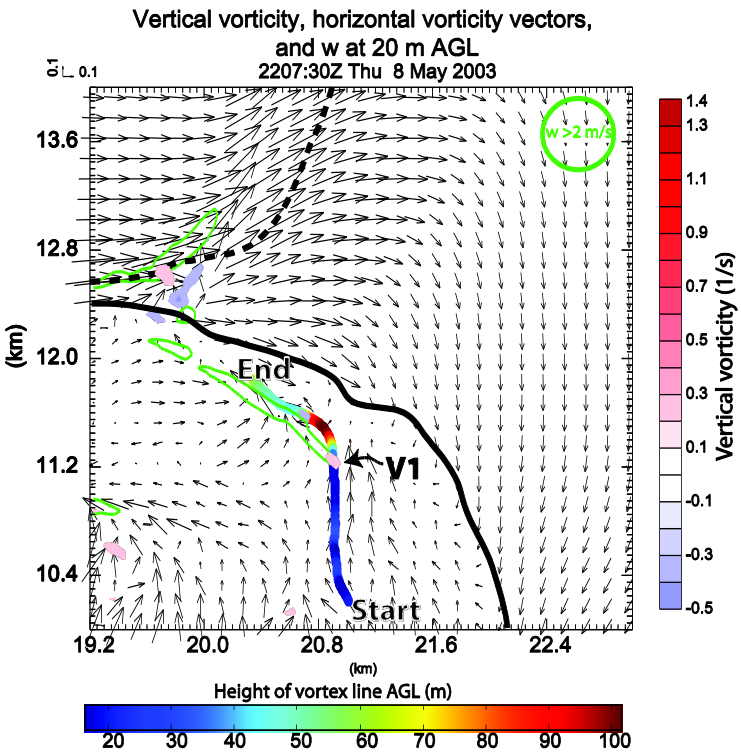

Fig. 4.9. Vertical vorticity (shaded, s^{-1}), horizontal vorticity vectors (s^{-1}), and vertical velocity (> 2 m s^{-1}, green contours) at 20 m AGL at 2207:30. A vortex line that passes through V1 at 20 m AGL is color coded by height AGL (m). 'Start' and 'End' mark the

start and end of the segment of the plotted vortex line and are included to indicate the direction of the horizontal vorticity along the vortex line (i.e., pointing from 'Start' to 'End'). Plotted area is the same as Fig. 4.4a.

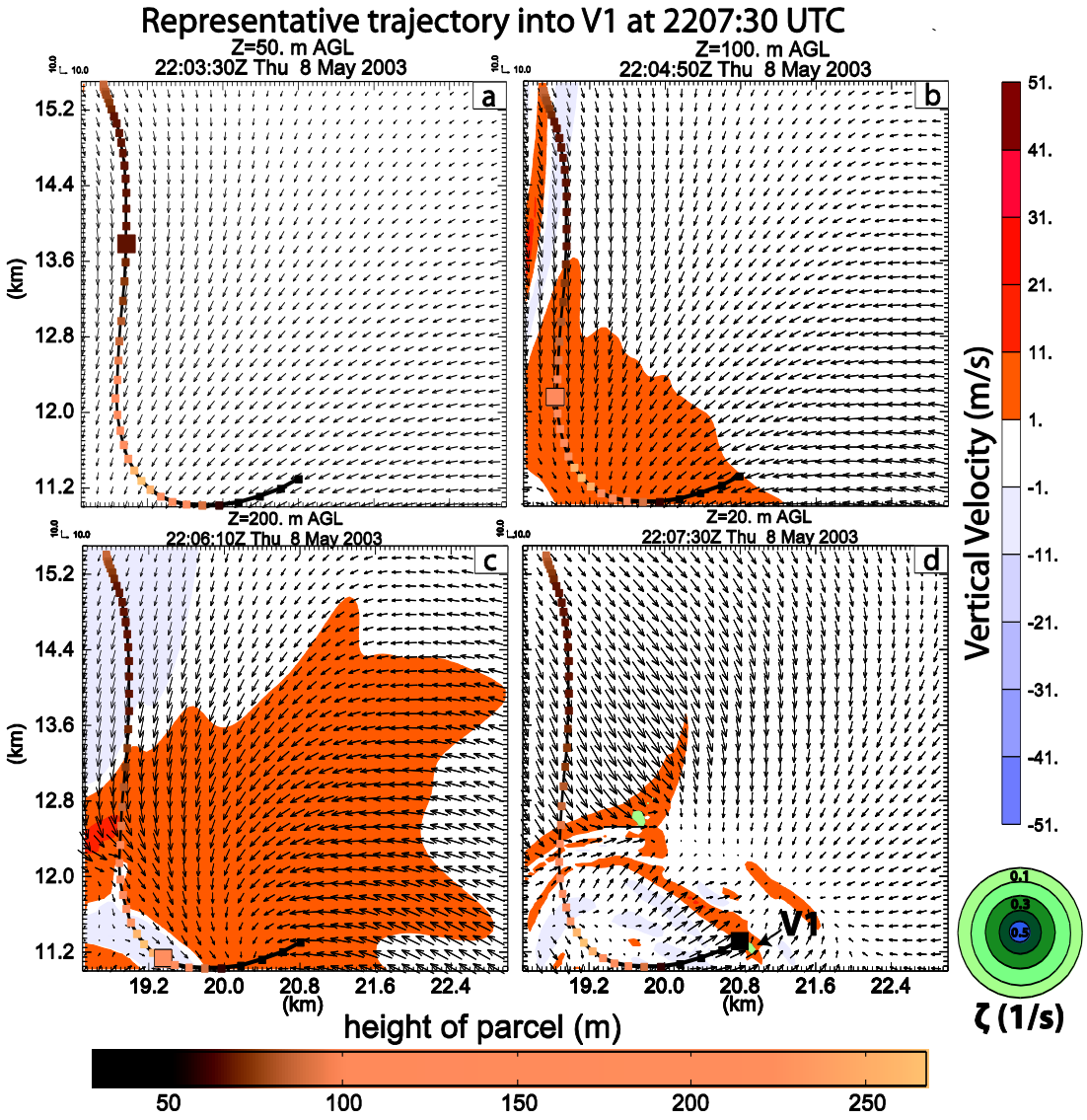

Fig. 4.10. Vertical velocity (shaded, m s^{-1}), horizontal wind vectors (m s^{-1}), and vertical vorticity (shaded in red hues starting at 0.1 s^{-1}) (a) 50 m AGL at 2203:30 UTC, (b) 100 m AGL at 2204:50 UTC, (c) 200 m AGL at 2206:10 UTC, and (d) 20 m AGL at 2207:30. A representative trajectory for a parcel that enters V1 20m AGL at 2207:30 UTC is color coded by height AGL (m). The panel-relative location is indicated by a larger color coded square in (a-d). The height AGL of fields plotted in (a-d) are the same as the height AGL of the parcel at the time plotted.

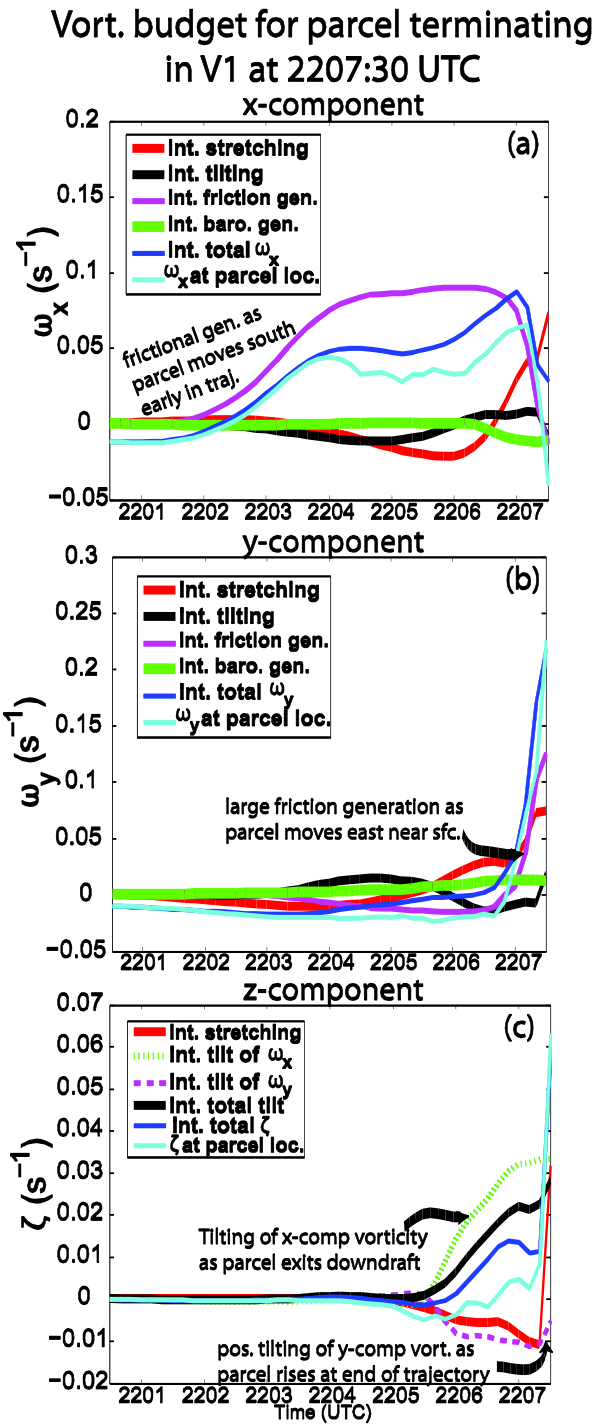

Fig. 4.11. Vorticity budgets calculated along the trajectory plotted in Fig. 4.10 for (a) x-component vorticity, (b) y-component vorticity, and (c) z-component vorticity. In (a), the dark blue line is the sum of the time-integrated x-component stretching (red line), tilting (black line), frictional generation (purple line), and baroclinic generation (green line). In (b), the dark blue line is the sum of the time-integrated y-component stretching (red line), tilting (black line), frictional generation (purple line), and baroclinic

generation (green line). In (c), the black line is the sum of the time-integrated tilting of x-component vorticity (green dashed line) and y-component vorticity (dashed purple line). The dark blue line in (c) is the sum of the time-integrated z-component stretching (red line) and tilting (black line). The cyan line represents the value of (a) x-component, (b) y-component, and (c) z-component vorticity interpolated from the model grid to the parcel location at each time.

A similar analysis conducted for V2 and V3 found that surface drag again plays a vital role in the development of horizontal vorticity that is tilted into the vertical. In the case of V2, vortex lines close to the ground point to the east-southeast, before turning to the south and rising into V2 (Fig. 4.12). Calculations along a representative trajectory that enters V2[11] (Fig. 4.13) show that the predominantly east-southeast pointing horizontal vorticity north of V2 (Fig. 4.12) was originally generated by drag in north-northeasterly low-level inflow (Fig. 4.14a,b). This horizontal vorticity is then tilted into the vertical as the inflow rises in the low-level updraft along the northern portions of the FFGF (Fig. 4.14c).

V3 is also the result of tilting of frictionally generated horizontal vorticity at low-levels, this time in the internal RFD surge. This is somewhat surprising as the internal RFD surge is relatively cold (Fig. 4.4d) which, at first glance, would seem to favor the generation and subsequent arching of baroclinically generated vorticity, as was suggested in Marquis et al. (2012). However, in the case under consideration, the horizontal vorticity vectors at low-levels again point in the opposite direction (vectors point toward the northeast) of that which would be expected for baroclinically generated vorticity (Fig. 4.15). Vortex lines lie near the ground point northeast in the internal

[11] It should be noted that these budgets are calculated for parcels that terminate in V2 at 200 m AGL (and 100 m AGL for V3) rather than 20 m AGL. This was necessitated by large sensitivities in the horizontal vorticity calculations for backward trajectories that were initialized very close to the ground. This occurred because the gradients in the vorticity generation terms (especially, frictional generation) are large near the ground, thus small errors in the vertical position of the trajectory led to large errors in the generation. Issues with errors in trajectory calculations will be discussed further in chapter 5.

RFD surge and then turn upward along the north side of the internal surge gust front (Fig. 4.15). A representative backward trajectory that terminates in V3 is plotted in Fig. 4.16. Vorticity budgets along this trajectory indicate that the northeastward pointing horizontal vorticity within the RFD surge was frictionally generated as low-level parcels travelled to the southeast behind the internal surge gust front (Fig. 4.17a,b). The horizontal vorticity is then tilted into the vertical and is subsequently stretched by the updraft along the leading edge of the internal RFD surge to create V3 (Fig. 4.17c).

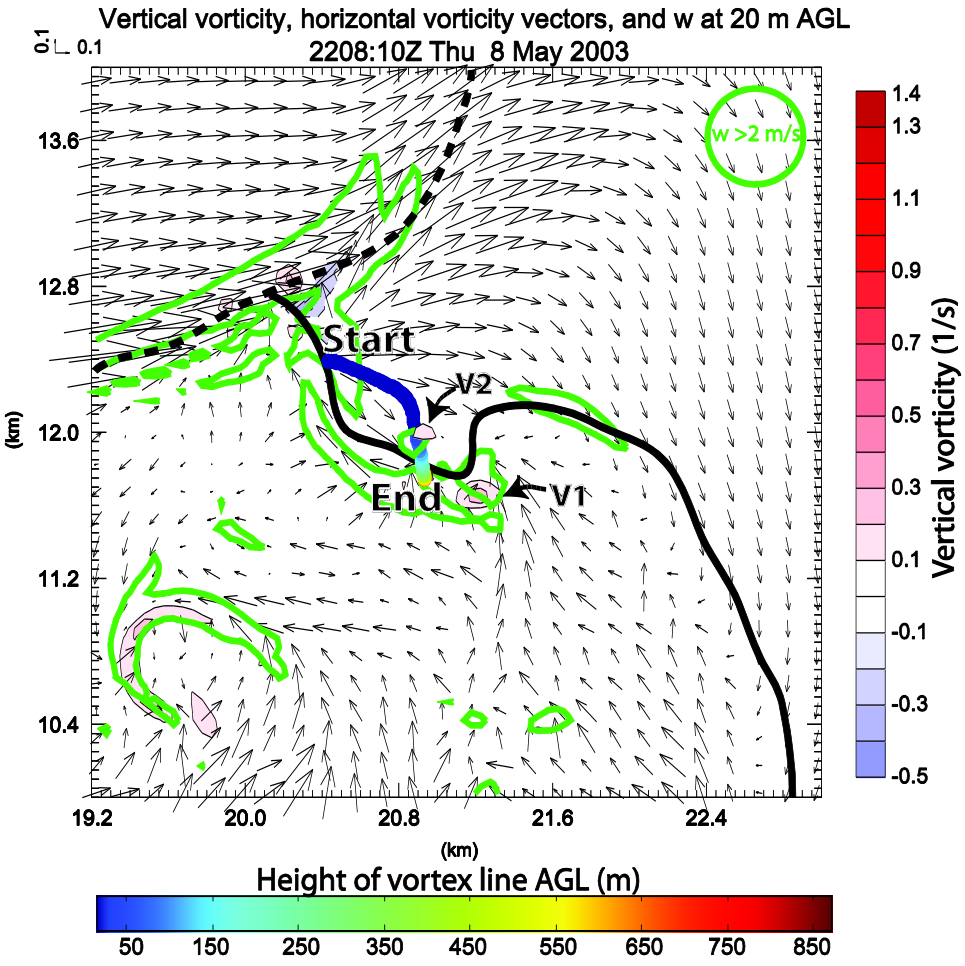

Fig. 4.12. As Fig. 4.9 but for a vortex line entering V2 at 20 m AGL at 2208:10 UTC. Plotted area is the same as Fig. 4.4b. (Note values on the color scale for the vortex line height are not the same as in Fig. 4.9)

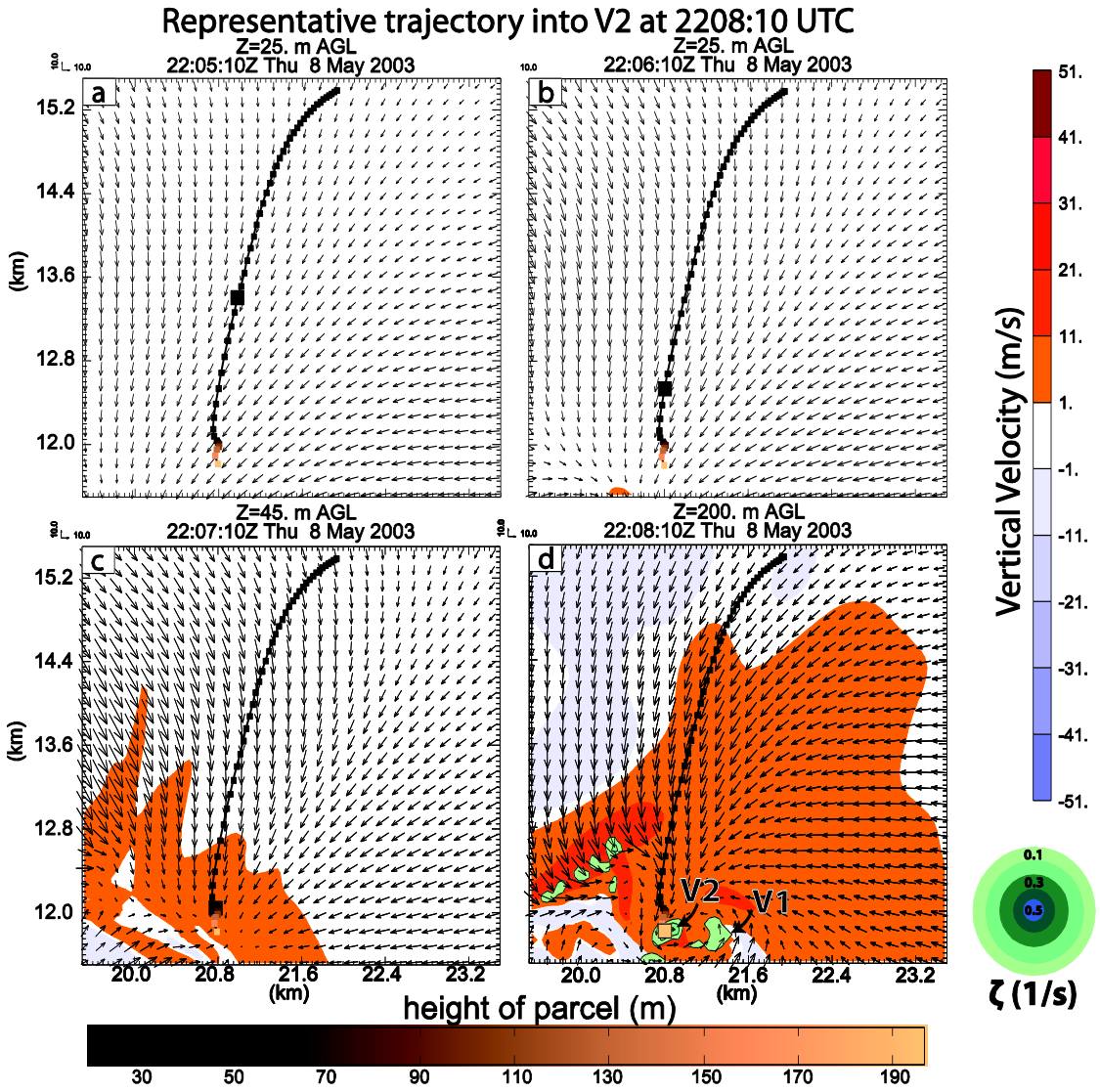

Fig. 4.13. As Fig. 4.10 but at (a) 25 m AGL at 2205:10 UTC, (b) 25 m AGL at 2206:10 UTC, (c) 45 m AGL at 2207:10 UTC, and (d) 200 m AGL at 2208:10 UTC. A representative parcel is plotted that enters V2 at 200 m AGL at 2208:10 UTC. (Note values on the color scale for the parcel height are not the same as in Fig. 4.10)

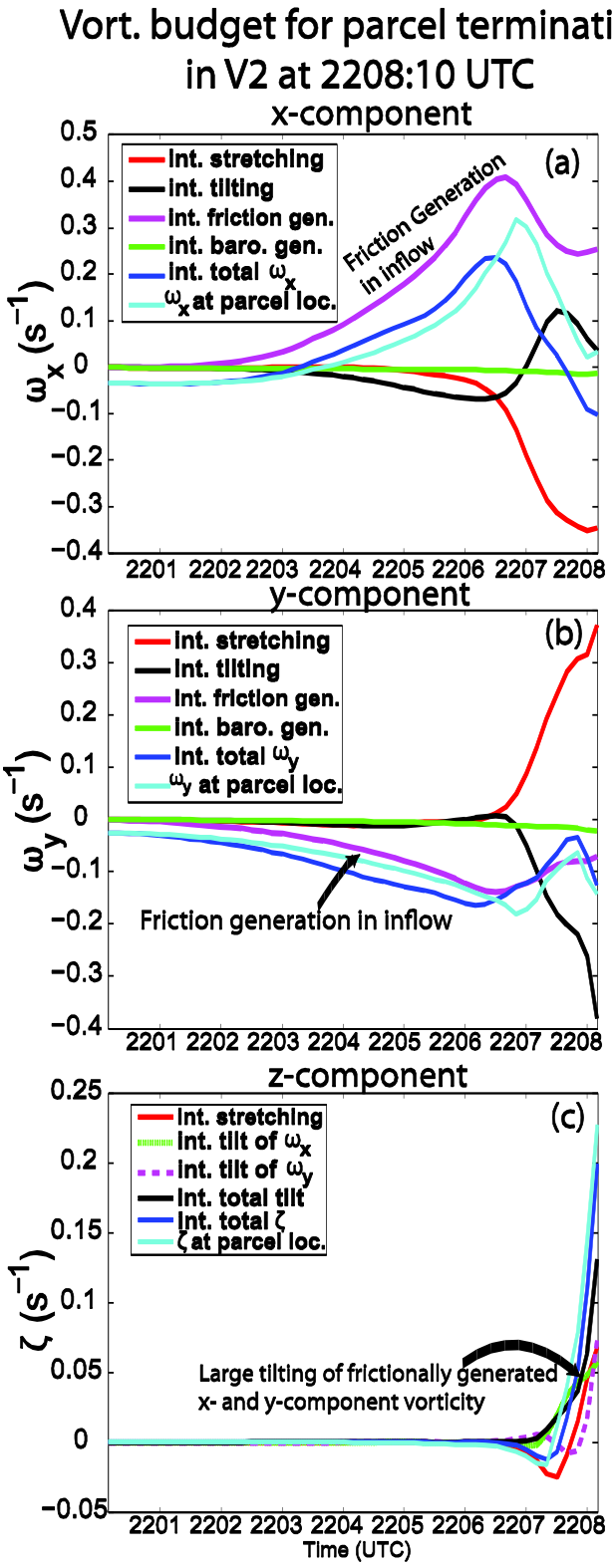

Fig. 4.14. As Fig. 4.11 but for parcel plotted in Fig. 4.13.

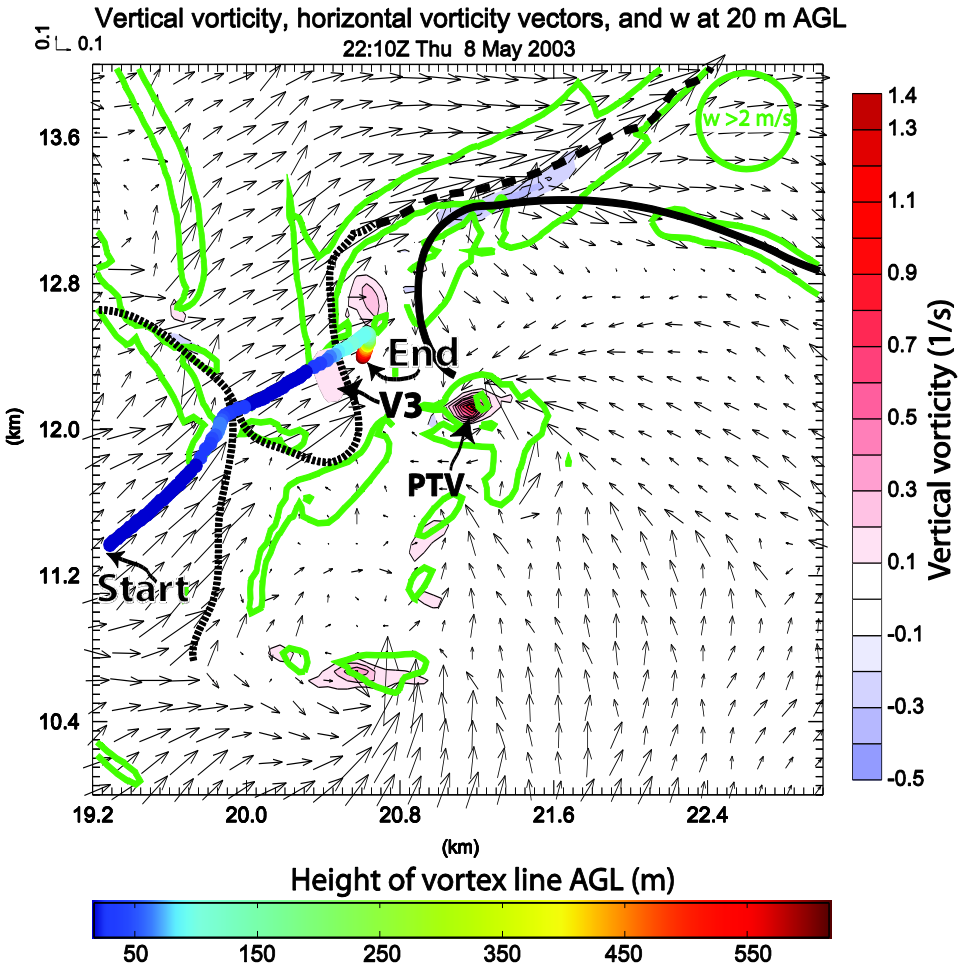

Fig. 4.15. As Fig. 4.9 but for but for a vortex line entering V3 at 20 m AGL at 2210 UTC. Plotted area is the same as Fig. 4.5a. (Note values on the color scale for the vortex line height are not the same as in Fig. 4.9).

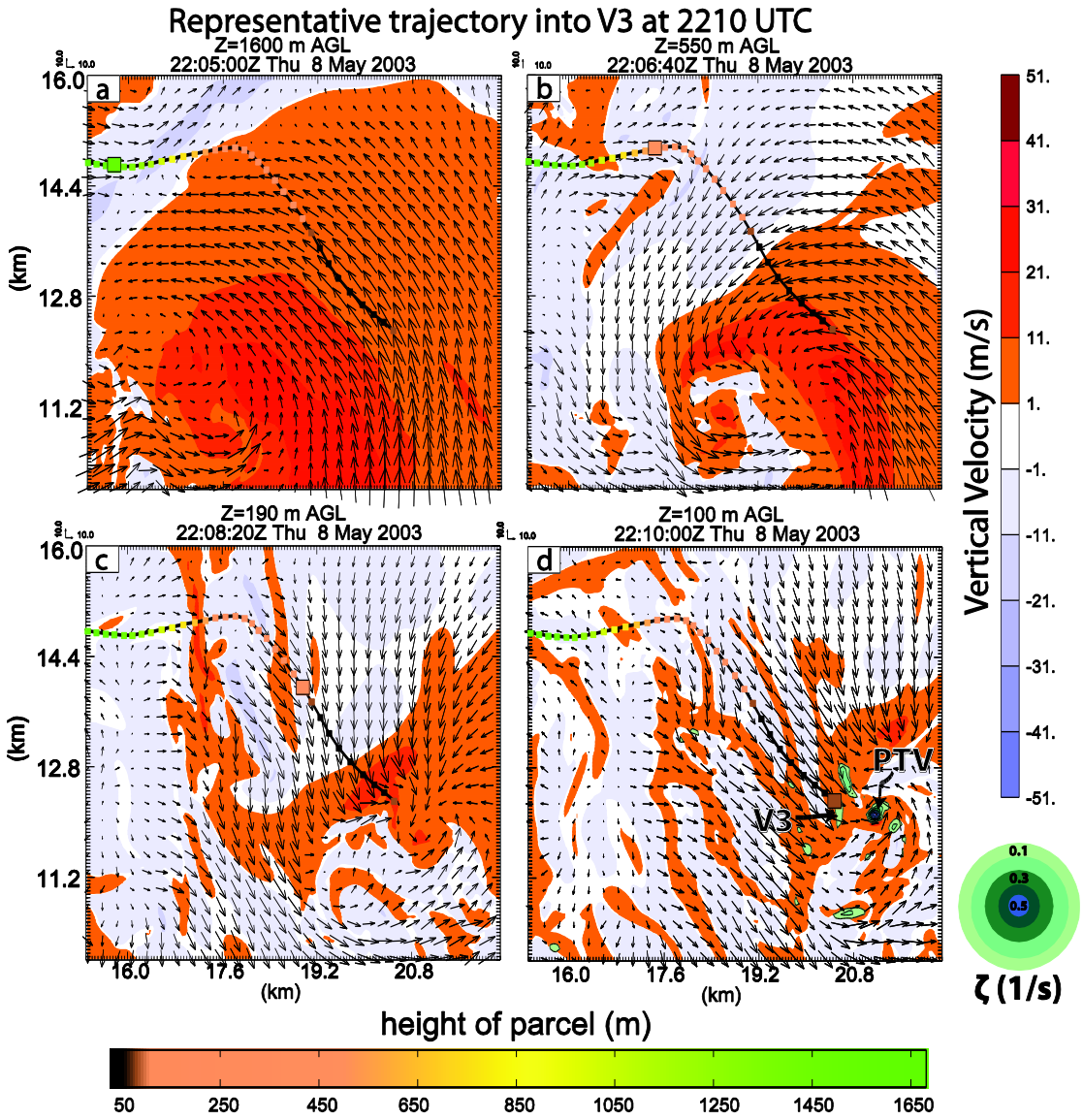

Fig. 4.16. As Fig. 4.10 but at (a) 1600 m AGL at 2205:00 UTC, (b) 550 m AGL at 2206:40 UTC, (c) 190 m AGL at 2208:20 UTC, and (d) 100 m AGL at 2210:00 UTC. A representative parcel is plotted that enters V3 at 100 m AGL at 2210:00 UTC. (Note values on the color scale for the parcel height are not the same as in Fig. 4.10)

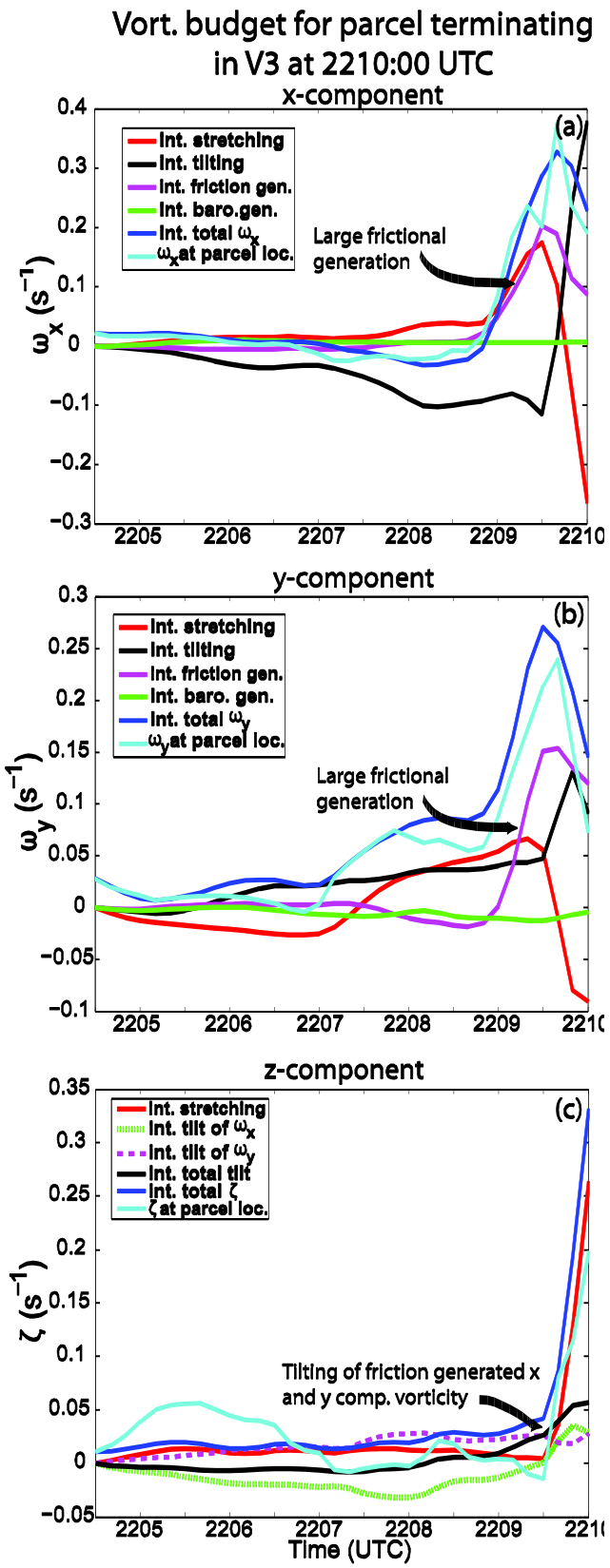

Fig. 4.17. As Fig. 4.11 but for parcel plotted in Fig. 4.16.

As the internal RFD surge approaches the low-level updraft associated with the PTV, V3 dramatically amplifies as seen in Fig. 4.5b,c. Tornadogenesis occurs as V3 (and the internal RFD surge) combines with the PTV. As these features merge, low-level horizontal vorticity vectors within the internal RFD surge, which initially are mainly crosswise to the flow, become increasingly streamwise as the flow develops a radially inward component toward the developing tornado (Fig. 4.18a,b). This streamwise vorticity is subsequently tilted in the vertical and stretched as it flows into the developing tornado (Fig. 4.18c).

The above result lends credence to the finding of recent studies that internal RFD surges play a major role in tornadogenesis and/or maintenance (Mashiko et al. 2009; Marquis et al. 2012; Lee et al. 2012). Marquis et al. (2012) concluded that these internal surges may be important because they increase low-level convergence and augment the vertical vorticity of the tornado via tilting of baroclinically generated horizontal vorticity along the internal surge gust front. Meanwhile, Mashiko et al. (2009) suggested that the internal RFD surge brought large environmental streamwise vorticity to the ground and into the tornado. The role of mechanically generated vorticity via surface drag in the internal RFD surge discussed above adds yet another possible way in which these internal surges may play an important role. It is worth noting that, unlike the studies mentioned above, the mechanism by which the internal surge plays an important role in the present case does not rely on the internal surge being very cold nor on their being extremely large environmental vorticity. This is encouraging given the variability in the thermodynamic characteristics of observed internal RFD surges (e.g., Lee et al. 2012) and the fact that extreme shear like that seen

in the tropical cyclone environment of Mashiko et al. (2009) is not typically observed in classic supercell environments.

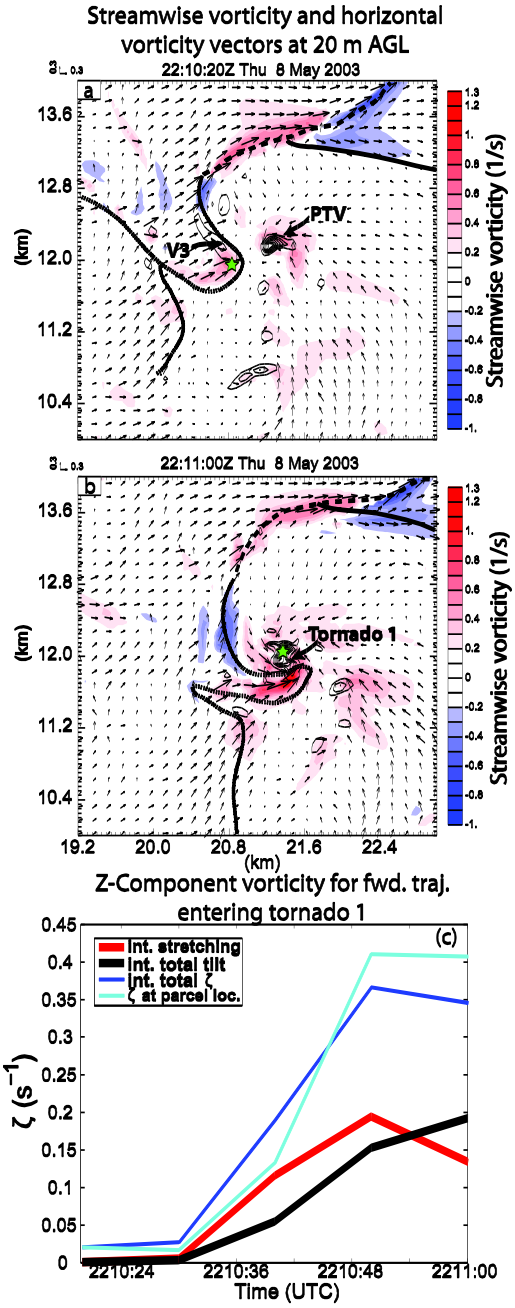

Fig. 4.18. Streamwise vorticity (shaded, s^{-1}), vertical vorticity (contoured, $^{s-1}$), and horizontal vorticity vectors (s^{-1}) at (a) 2210:20 UTC and (b) 2211:00 UTC. The green star in (a) and (b) marks the start and end location of a forward trajectory, respectively. A vertical vorticity budget for this parcel is plotted in (c). The dark blue line is the sum of the time-integrated stretching (red line) and tilting (black line). The cyan line is the model value of vertical vorticity interpolated to the parcel location at each time.

4.4.2 Development of the second tornado

As mentioned above, the development of the tornado 2 was somewhat less complex than that of tornado 1 with only one important vertical vorticity maximum contributing to tornado 2. This vertical vorticity maximum, V4, developed immediately in advance of the RFGF as a stronger surge of inflow air moved toward the RFGF (Fig. 4.7b). The stronger surge of inflow air was associated with a new convective updraft that developed in advance of the RFGF (not shown). This evolution resembles the case described in Wakimoto and Atkins (1996) in which a tornado developed rapidly in association with a new convective cell that formed along the flanking line of a mature supercell. On the storm-scale, this evolution also resembles the type-II descending reflectivity core scenario presented in Byko et al. (2009), with V4 developing between stage 3 and 4 of their conceptual model. More specifically, V4 develops as the new updraft encountered the RFGF and began to merge with the main updraft of the OKC storm.

In order to investigate further the development of V4 and tornado 2, a detailed trajectory and vortex line analysis was performed. This analysis reveals that, at low-levels, horizontal vorticity vectors in the inflow surge associated with the new updraft point toward the southwest (Fig. 4.19). Vortex lines that enter V4 are horizontal, pointing to the southwest, before rising abruptly as they reach the RFGF (Fig. 4.19). Backward trajectory analysis indicates that parcels that enter V4 come from the southeast at low-levels and rise as they encounter the RFGF (a representative parcel is plotted in Fig. 4.20). Vorticity budget calculations along the trajectory shown in Fig. 4.20 indicate that the parcel acquires large horizontal vorticity as it moves towards V4

(Fig. 4.21a,b). In the y-direction, much of this vorticity is generated via surface drag (Fig. 4.21b). The x-component vorticity is budget is more complicated (Fig. 4.21a), as the parcel begins with substantial negative x-component vorticity associated with the environmental shear profile. As the parcel accelerates westward, x-component vorticity increases owing to a combination of tilting of y-component frictionally generated vorticity, a brief period of generation of x-component vorticity by surface drag, and stretching of the both the original environmental vorticity and the new frictionally generated vorticity. Because the stretching term is non-linear it is not possible to determine whether stretching acts more on the pre-existing environmental vorticity or the frictionally generated vorticity. Thus, the relative importance of environmental vorticity vs. mechanically generated vorticity cannot be determined. The vertical vorticity budget indicates that tilting of x-component vorticity is the most important in generating V4 (Fig. 4.21c). As such, the most definitive statement that can be made about V4 is that it is likely the result of tilting of both environmental vorticity as well as vorticity generated by surface drag (i.e., it is *not* the result of baroclinic vorticity generation).

Between 22:18 and 22:20, V4 continues to strengthen as it moves north (see Fig. 4.7). During this time period, V4 is located on the southern edge of a low-level updraft maximum along the RFGF (Fig. 4.22a). Around 22:20, V4 becomes better collocated with the low-level updraft and reaches tornadic strength (Fig. 4.22b). An area of strong westerly flow develops to the west of tornado 2 with large frictionally generated northward pointing vorticity (Fig. 4.22a,b). This vorticity begins crosswise, but becomes streamwise as the flow accelerates radially inward toward tornado 2 (Fig.

4.22c). This streamwise vorticity is then tilted and stretched, aiding in the intensification of the developing tornado. This is somewhat similar to the role played by the internal RFD surge that was associated with the generation of tornado 1. However, unlike the earlier internal RFD surge, the internal surge of westerly momentum associated with tornado 2 cannot be traced far upstream and, instead, appears to develop in-situ as the flow accelerates in response to the development of tornado 2 and associated low-level updraft.

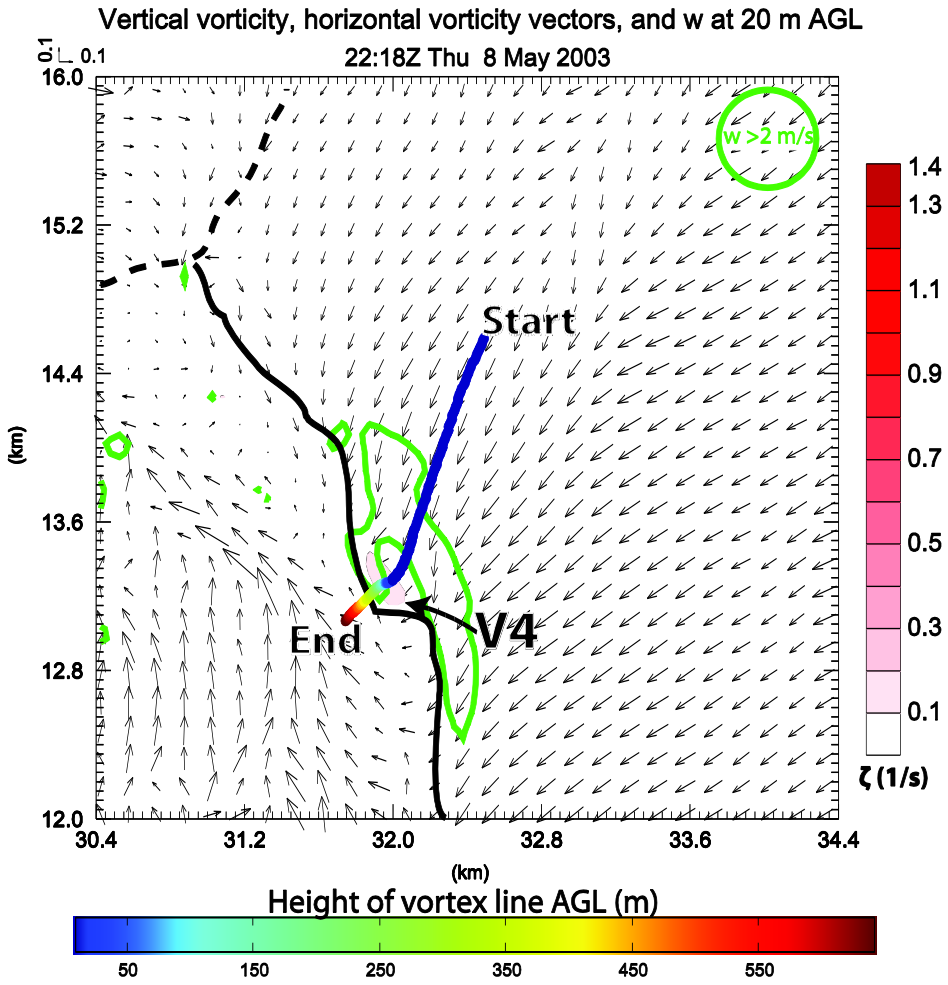

Fig. 4.19. As Fig. 4.9 but for a vortex line entering V4 at 20 m AGL at 2218 UTC. Plotted area is the same as Fig. 4.7b. (Note values on the color scale for the vortex line height are not the same as in Fig. 4.9)

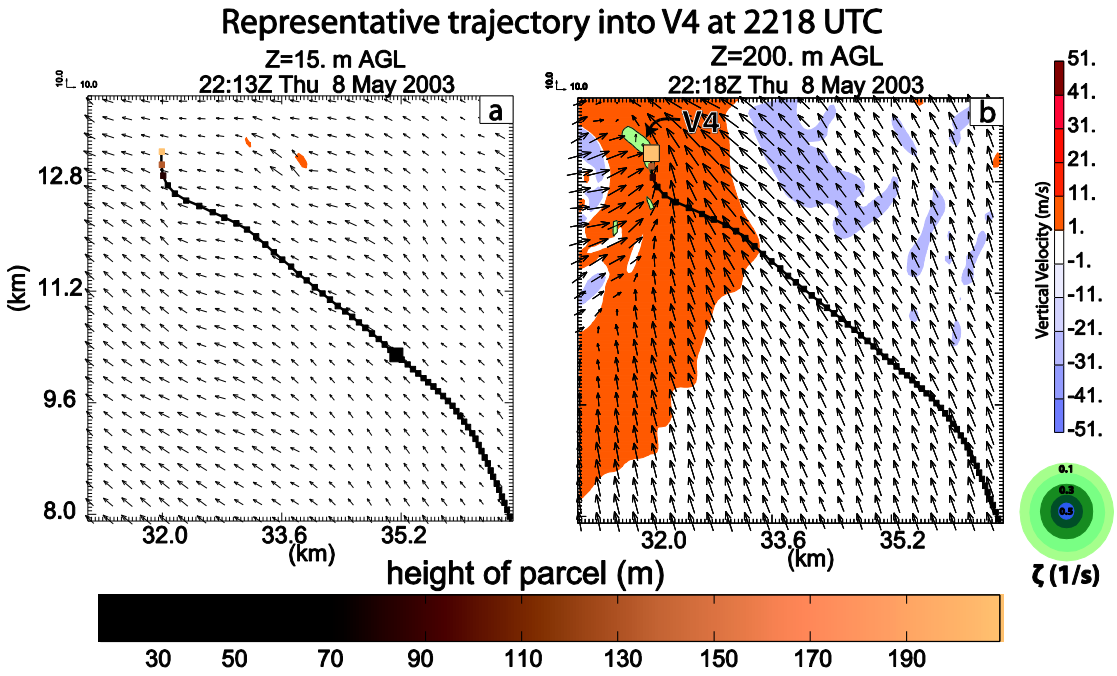

Fig. 4.20 As Fig. 4.10 but at (a) 15 m AGL at 2213 UTC, (b) 200 m AGL at 2218 UTC. A representative parcel is plotted that enters V4 at 200 m AGL at 2218. (Note values on the color scale for the parcel height are not the same as in Fig. 4.10)

It is important to clarify the role of the new updraft and associated DRC presented herein. Specifically, rather than impacting the low-level horizontal vorticity distribution via outflow from the DRC, it appears that the enhancement of inflow into the new updraft responsible for the DRC is key in horizontal vorticity generation and amplification. As this inflow surge encounters the pre-existing RFGF, increasing low-level convergence dynamically extends the updraft closer to the surface. This downward extension of the updraft allows the frictionally generated and environmental vorticity within the inflow surge to be tilted and stretched at low-levels, thus leading to the formation of V4.

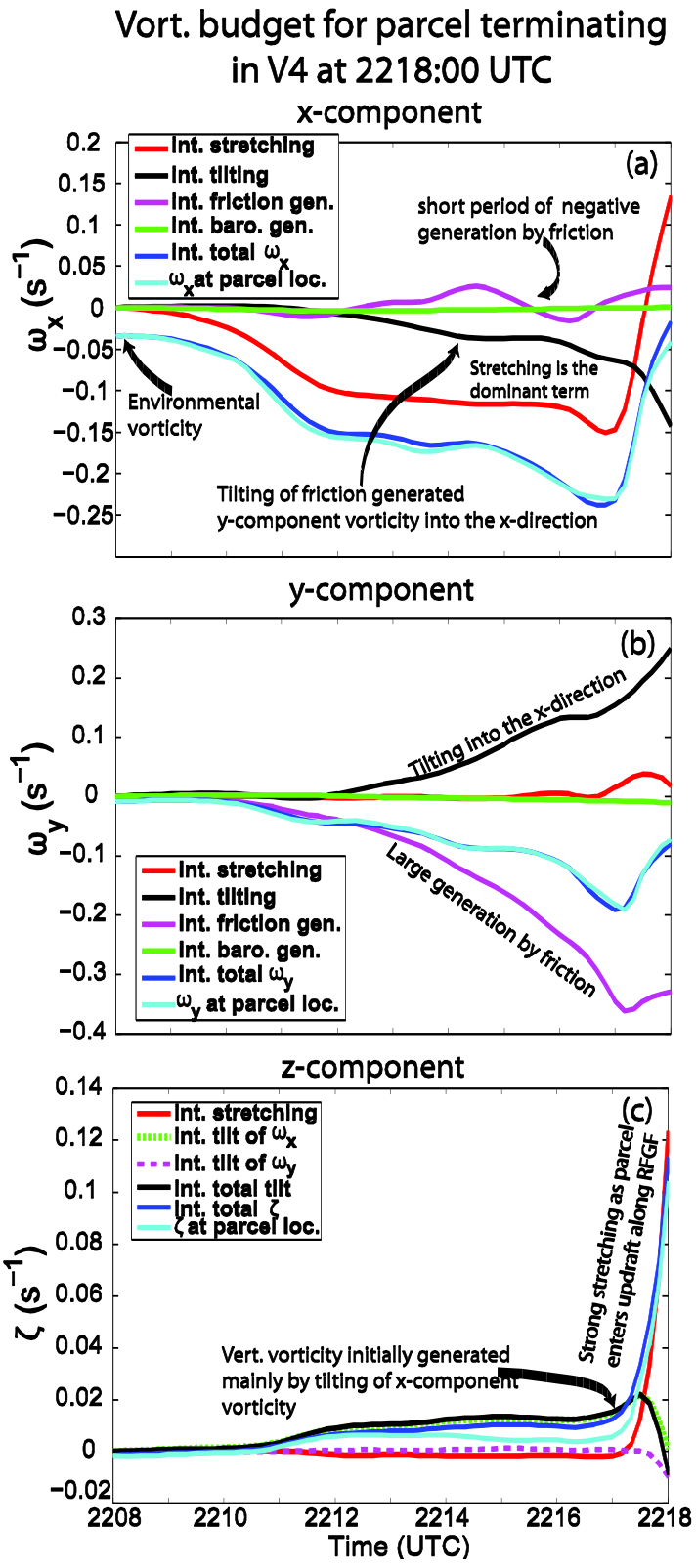

Fig. 4.21. As Fig. 4.11 but for the trajectory plotted in Fig. 4.20.

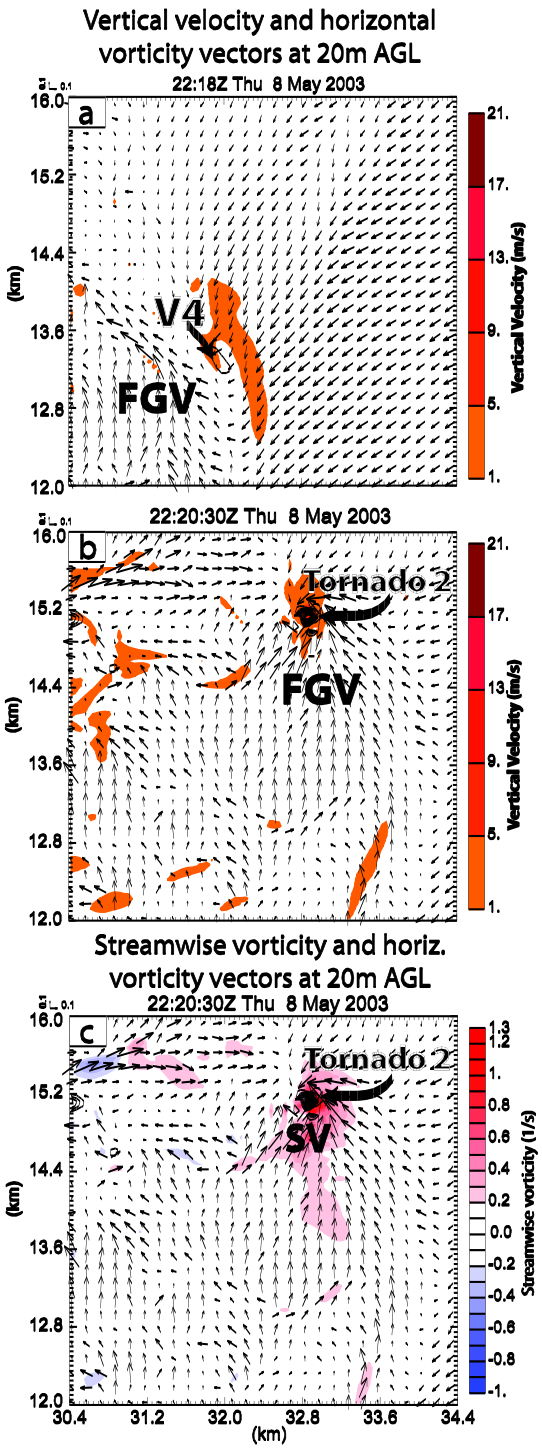

Fig. 4.22. Vertical velocity (shaded, m s^{-1}) and horizontal vorticity vectors (s^{-1}) at 20 m AGL at (a) 2218:00 UTC and (b) 2220:30 UTC. The same area is plotted in (c) but streamwise vorticity (shaded, s^{-1}) is plotted instead of vertical velocity at 2220:30 UTC. 'FGV' and 'SV' mark locations of large frictionally generated and streamwise vorticity, respectively.

4.4.3 Low-level mesocyclones

Thus far, this study has focused predominantly discussing a ground-up viewpoint of tornadogenesis. However, many studies of tornadic supercells have found an intimate connection between the tornado and the low-level mesocyclone (e.g., Burgess et al. 1993). On the other hand, past studies have found little correlation between the intensity of the low-level mesocyclone and the tornado (e.g., Trapp 1999). Moreover, it is estimated that only roughly 40 % of low-level mesocyclones are associated with tornadoes (Trapp et al. 2005a). It is the author's opinion that the only well-established connection between the low-level mesocyclone and tornado, is that when a tornado is present a low-level mesocyclone is also typically present.

In the simulation under investigation, low-level mesocyclones are present but they are fairly transient, difficult to define, and there does not appear to be a strong link between them and the simulated tornadoes. In fact, examination of the surface fields indicates that low-level mesocyclones may be caused by the near-surface convergence pattern and associated low-level updrafts caused by the RFGF and FFGF. This implies that the presence of a low-level mesocyclone may be a result of the near-surface wind pattern that is also associated with the pre-tornadic and/or tornadic supercell. In other words, a possible reason low-level mesocyclones are typically present in association with most tornadoes is that the near-surface wind field is responsible for both the tornado and the low-level mesocyclone. Low-level mesocyclones are often observed in both tornadic and non-tornadic supercells, however, which may be a reflection of the fact that the low-level wind field in tornadic supercells has been found to be similar to

the wind field in non-tornadic supercells just prior to tornadogenesis failure (Trapp 1999).

To illustrate the above points, the low-level mesocyclone associated with tornado 1 is examined. At 2211 UTC, about 1 km to the north of the developing tornado 1, an intense low-level updraft is present where the RFGF is colliding with the FFGF (Fig. 4.23a). This intense low-level updraft is at the center of a low-level mesocyclone (Fig. 4.23a). Backward trajectory calculations indicate that much of the air rising within the updraft is coming from the cool side of the FFGF. Specifically, air parcels that enter the updraft originate in the inflow to the east of the storm ~200 m AGL, descend gradually in the FFD, and then ascend rapidly as they approach the FFGF from the rear (not shown). Vorticity budget analyses along a representative trajectory reveal that environmental horizontal vorticity is amplified via horizontal stretching as air parcels accelerate towards the low-level updraft (Fig. 4.24a,b). These air parcels then rise rapidly in the updraft and the large streamwise horizontal vorticity is tilted into the vertical, leading to the development of the low-level mesocyclone (Fig. 4.24c).

As the RFGF occludes, the forcing for the low-level updraft on the cool side of FFGF weakens leading to the rapid weakening of the low-level mesocyclone around 2214 UTC (Fig. 4.23b). Tornado 1 continues to move east-northeast and persists until 2224 UTC. During this period, there is no persistent low-level mesocyclone and, even when broader low-level rotation is present, there seems to be little or no direct dynamical connection between it and tornado 1.

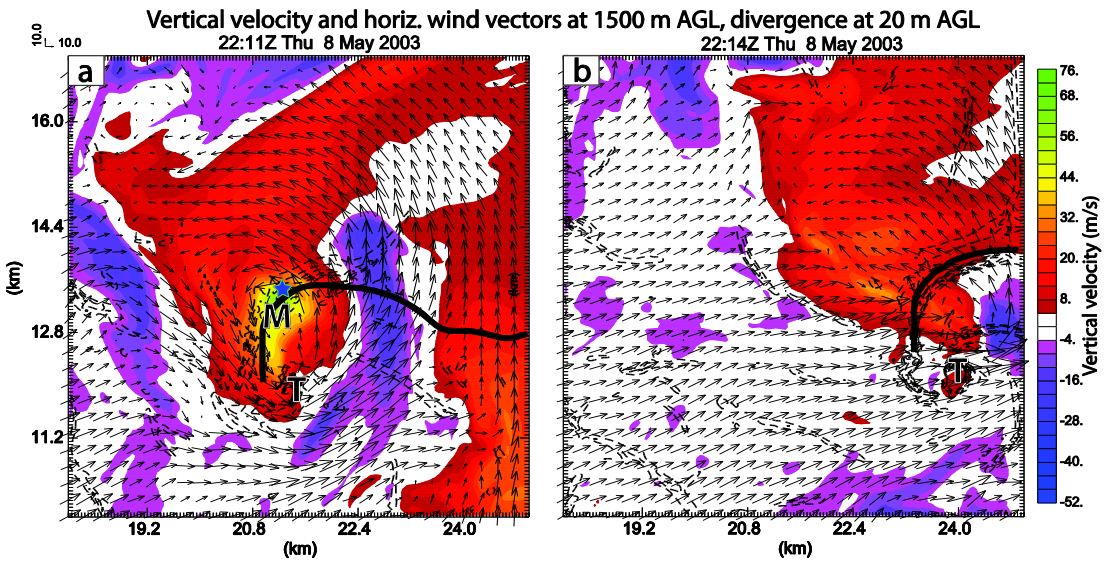

Fig. 4.23. Vertical velocity (shaded, m s^{-1}) and horizontal wind vectors at 1500 m AGL and horizontal divergence (dashed contours < 0.10 s^{-1}) at 20 m AGL at (a) 2211 UTC and (b) 2214 UTC. The solid black line marks the location of the forward-flank gust front at 20 m AGL. The 'M' marks the location of the low-level mesocyclone at 1500 m AGL. The 'T' marks the location of tornado 1 at 20 m AGL. The blue star near x=21.2, y=13.4 in (a) marks the location of the backward trajectory used for vorticity budget calculations in Fig. 4.24.

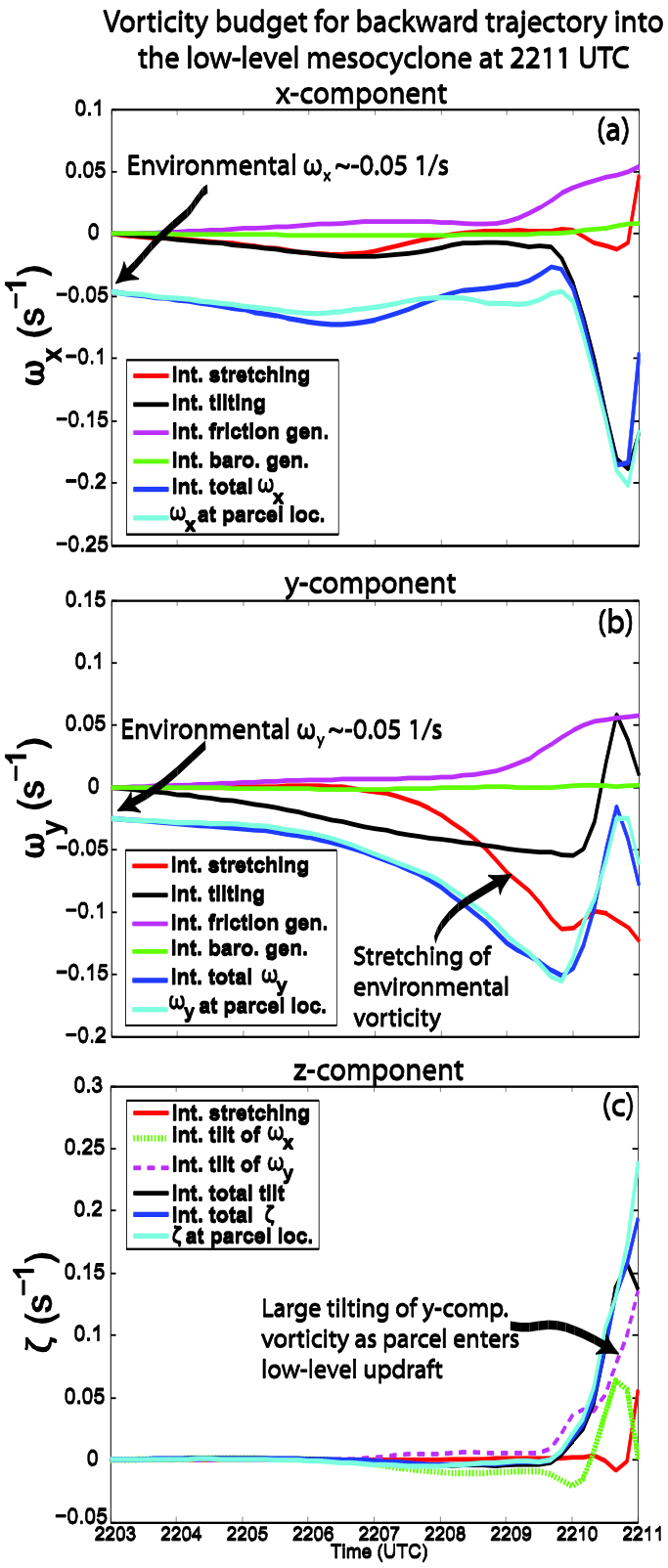

Fig. 4.24. As Fig. 4.11 but for the parcel terminating at the green star within the low-level mesocyclone at 1500 m AGL at 2211 UTC in Fig. 4.23.

4.4.4 Experiment without surface drag

In attempt to verify the important role surface drag played in the simulation discussed above, the simulation was re-run with the mechanical drag coefficient set to zero. As in the simulation of the 8-9 May 2007 tornadic mesovortex presented in chapter 3, only the innermost grid (in the present case, the 50-m grid-spacing domain) was re-run with drag turned off. Boundary and initial conditions are still impacted by the surface drag parameterizations. However, given that the tornadoes and low-level structure of the supercell developed largely during the simulation on the 50-m grid-spacing domain, it is assumed that the impact of drag from the boundary and initial conditions should be relatively small.

Comparison of the no-drag and drag simulations reveals considerable differences. Not surprisingly, the largest differences in the simulations involve the low-level wind field. Specifically, the RFGF structure is substantially different with a less distinct RFGF in the no-drag experiment (Fig. 4.25). Additionally, while a tornado does develop in the no-drag simulation (hereafter, tornado ND1), it is much shorter-lived than tornado 1 in the drag simulation. Tornado ND1 follows a very different path than tornado 1, initially moving northeast before briefly turning to the west and then southeast before dissipating (Fig. 4.26). The maximum wind speeds in the no-drag simulation tornado are briefly stronger than those in the drag simulation; however, it appears that these winds may be primarily caused by an extremely strong occlusion downdraft that develops to the northeast of tornado ND1 (not shown). This downdraft is also responsible for the westward motion of the tornado ND1. Tornado ND1 then

weakens while being pushed to the southeast by a cold internal outflow surge (not shown). No additional tornadoes form after the dissipation of tornado ND1.

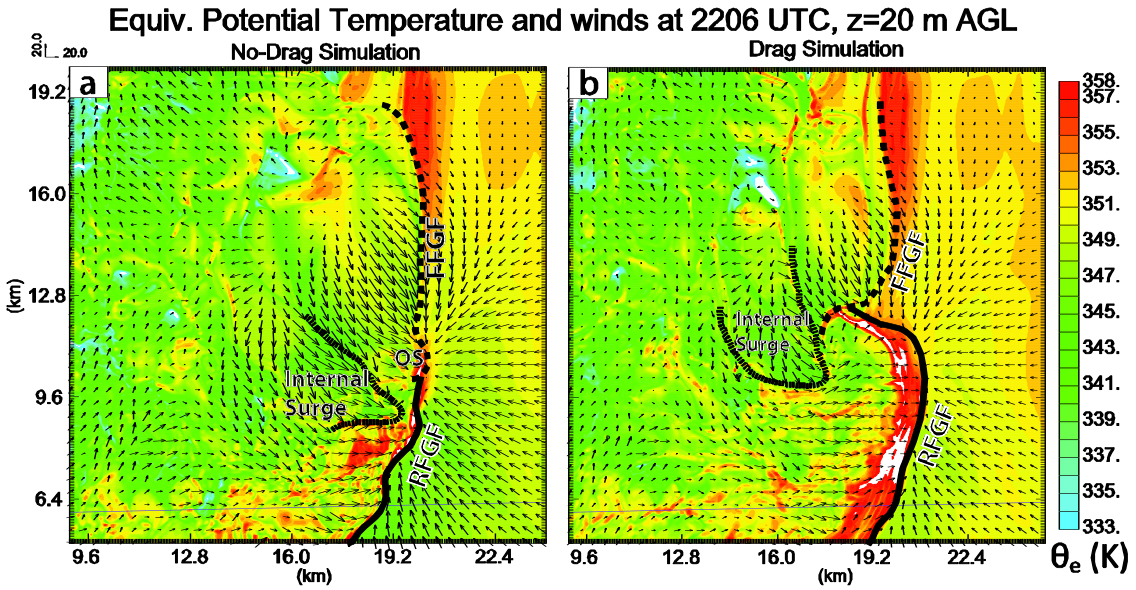

Fig. 4.25. (a) as Fig. 4.3b but for the no-drag run for comparison with (b) a reproduction of Fig. 4.3b.

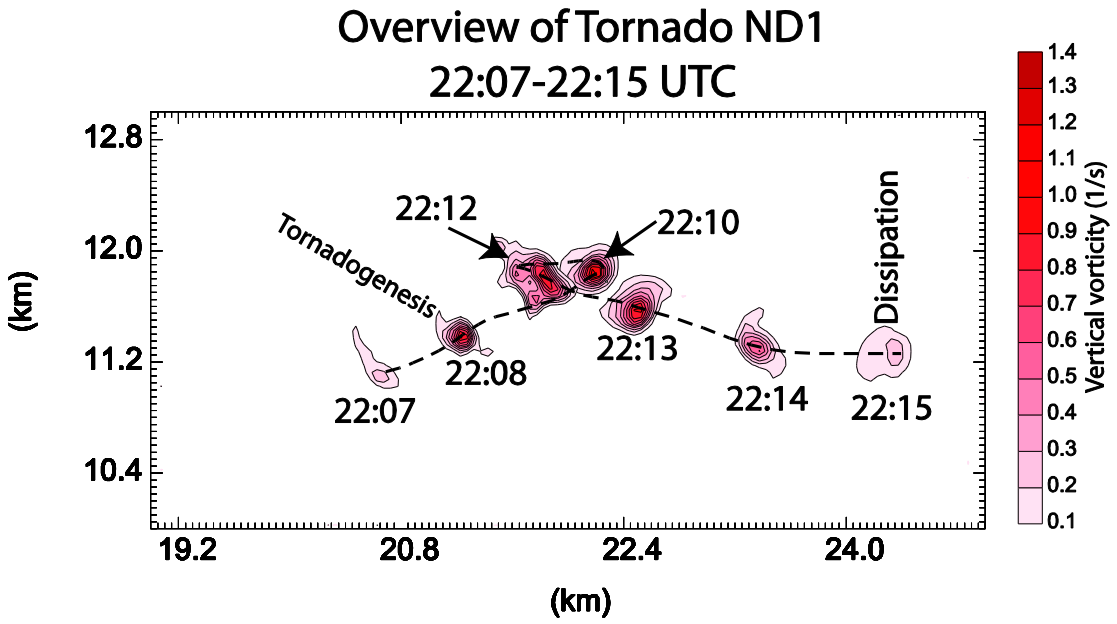

Fig. 4.26. As Fig. 4.6 but for tornado ND1. For clarity, the dashed line is included to mark the track of tornado ND 1.

Closer examination of the formation of tornado ND1 reveals that it originated as a small vorticity maximum along the leading edge of an outflow surge (Fig. 4.27). A detailed vortex line and trajectory analysis was performed in order to determine the origin of this vertical vorticity. The vortex line analysis shows that southeastward-pointing horizontal vortex lines within the outflow surge tilt upward, turn toward the southwest, and arch over the outflow surge creating a vorticity couplet (Fig. 4.27). The northern cyclonic member of this couplet is the vorticity maximum that becomes tornado ND1. The southern anti-cyclonic member of the couplet dissipates with time.

Vorticity budgets along backward trajectories that enter tornado ND1 were examined in order to determine the origin of the horizontal vorticity that was tilted into the developing tornado. Unfortunately, this analysis proved inconclusive as large errors were present in the horizontal vorticity budget calculations. These errors seemed to be caused by too much generation by horizontal stretching as parcels accelerated towards the tornado. Errors in trajectory calculations will be discussed in much greater detail in the following chapter.

Vorticity budgets along backward trajectories in the vicinity of tornado ND1 (~1 km upstream of the tornado) within the outflow surge were much more accurate than those that were initiated within the developing tornado. This analysis revealed that the outflow surge is composed of parcels that originate 300-500 m AGL in the inflow to the northeast of the supercell. Vorticity budgets for these parcels indicate that the horizontal vorticity present in the outflow surge is predominantly environmental vorticity that is tilted and stretched (in the horizontal direction) as the parcels accelerate towards the southeast after descending in the RFD (Fig. 4.28). In other words,

baroclinic vorticity generation does not play a large role in generating the horizontal vorticity within the outflow surge. Although, it cannot be said with complete certainty that the parcels within the vicinity of the tornado in the outflow surge actually enter the tornado, the balance of the evidence suggests that the horizontal vorticity that is tilted to generate tornado ND1 originates barotropically (i.e., from the environment) and not baroclinically.

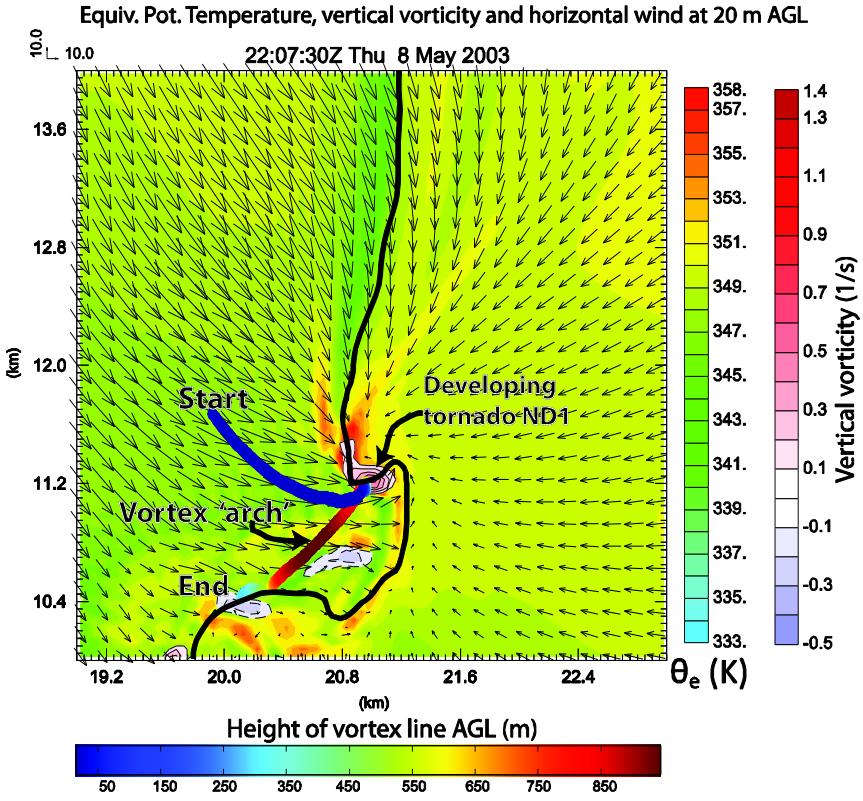

Fig. 4.27. As Fig. 4.9 but including equivalent potential temperature (shaded, K) and for a vortex line entering tornado ND1 20 m AGL at 2207:30 UTC.

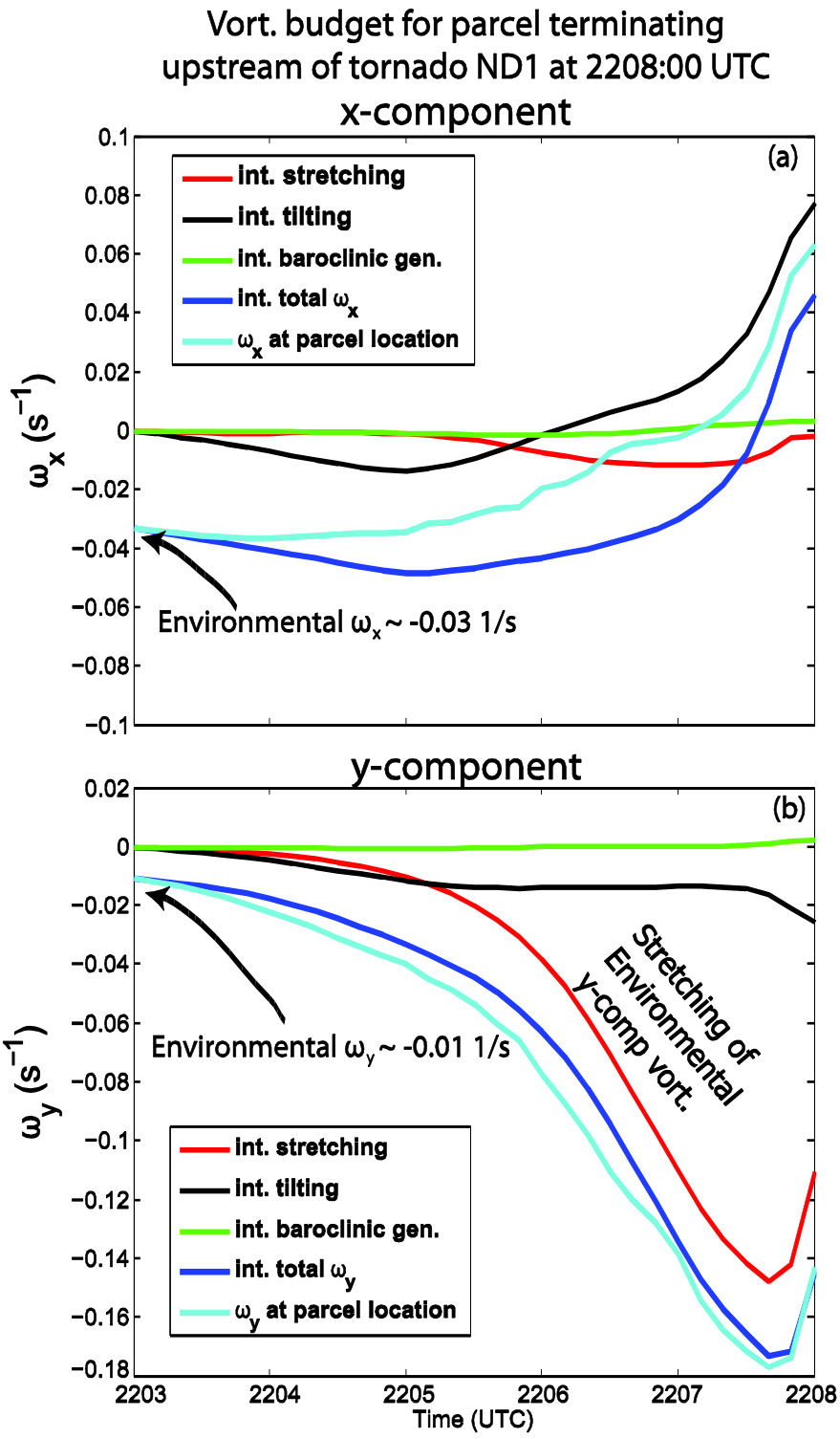

Fig. 4.28. As Fig. 4.11 but only for the x- and y–component vorticity for a parcel terminating about 1 km to the northwest of tornado ND1 at 2208 UTC in the no-drag simulation.

It is interesting to note that while outflow surges in both the drag and no-drag simulations were important in tornadogenesis, the mechanism by which they instigated tornadogenesis was quite different. In the drag simulation, frictionally generated horizontal vorticity is the dominant term in the vorticity budget and supplies a large source of streamwise vorticity for tilting and subsequent stretching in the tornado. In the no-drag simulation, the outflow surge appears to be important for re-orienting, amplifying, and then tilting environmental vorticity into the vertical. Because the environmental shear is initially the same in both experiments, this amplification of environmental vorticity should also be present in the drag simulation. However, in the drag simulation this amplification is likely damped by the fact that horizontal accelerations of downdraft parcels near the ground are slowed by the surface drag parameterization. It is also possible that large generation of vorticity by drag overwhelms the initial environmental vorticity: Environmental inflow vorticity points to the west and south while frictionally generated vorticity (for the southeast flow within the outflow surge) is to the east and north.

The above results are likely case and location dependent. For example, Mashiko et al. (2009) found that an internal outflow surge was also important in amplifying and tilting pre-existing environmental vorticity. Their simulation included the parameterized effects of surface drag and they mention that the frictional generation of horizontal vorticity is relatively small in their case. However, their simulation was conducted for a storm that was predominantly located over water. Resolving the relative impact of surface drag vs. pre-existing environmental vorticity will likely require extensive sensitivity experiments that are beyond the scope of the present study.

4.5 Summary and discussion

Tornadogenesis was investigated in detail in a high-resolution simulation of the 8 May 2003 Oklahoma City tornadic supercell. The simulation, which featured 50-m horizontal grid spacing, was one-way nested within three coarser-resolution simulations. The outermost domain had 9-km grid spacing and assimilated conventional observations via the Advanced Regional Prediction System (ARPS) 3DVAR. The ARPS 3DVAR was also used in five-minute data assimilation cycles to assimilate radar data onto a 1-km grid-spacing domain that was nested within the 9-km domain. The 1-km grid spacing domain provided boundary and initial conditions for a nested 100-m grid spacing domain. Boundary and initial conditions for the 50-m grid spacing simulation were obtained from this 100-m grid spacing simulation.

Two tornadoes developed in the 50-m grid spacing simulation (tornado 1 and tornado 2). Both of these tornadoes tracked within 10 km of the observed OKC tornado. Detailed analysis of the models fields, vortex lines, and backward trajectories was conducted to elucidate the important processes responsible for the genesis for tornadoes 1 and 2. Conceptual models are now presented that summarize the results of this detailed analysis. The conceptual model for tornado 1 (Fig. 4.29) has three stages and can be summarized as follows:

I. The RFD becomes organized and large frictionally generated vorticity develops behind the RFGF at low-levels. This vorticity is tilted into the vertical on the northern edge of the RFGF, leading to the formation of a small vertical vorticity maximum (V1). Concurrently, large eastward-pointing horizontal vorticity is frictionally generated in low-level northerly inflow to the north and east of the

RFGF. As parcels are forced to rise upon encountering the RFGF, this vorticity is tilted and another small vertical vorticity maximum (V2) forms near the intersection of the RFGF and FFGF.

II. As the RFGF occludes, the two areas of vorticity described in step 1 merge to form a pre-tornadic vortex (PTV). At the same time, an internal RFD surge, that is the result of heavy precipitation in the core of the supercell, is moving quickly southeast toward the PTV. Large northeastward-pointing horizontal vorticity is generated by surface drag at low-levels within the internal RFD surge. This vorticity is tilted upward on the northeast side of the internal surge to create a third vorticity maximum (V3).

III. The internal RFD surge triggers tornadogenesis as it merges with the PTV, providing a substantial source of horizontal vorticity that is readily ingested into the developing tornado.

Although, its development differs substantially from tornado 1, the development of tornado 2 is also well-described by a three-step conceptual model (Fig. 4.30). This model can be described as follows:

I. A new convective updraft develops to the southeast of the supercell. The updraft is associated with enhanced southeasterly low-level flow which acts to stretch pre-existing environmental negative x-component vorticity and generate new negative y-component vorticity (some of which is tilted into the negative x-direction). The end result is an enhanced area of southwestward-pointing horizontal vorticity at low-levels associated with the enhanced southeasterly low-level flow.

II. The new updraft in the inflow and associated low-level surge encounter the RFGF. The enhanced low-level convergence extends the updraft to low-levels. A small vertical vorticity maximum (V4) forms as the horizontal vorticity described in step 1 is tilted upward on the southeast edge of the low-level updraft.

III. The vertical vorticity maximum strengthens as it becomes better collocated with the low-level updraft, leading to more intense vertical stretching. Concurrently, large frictionally generated crosswise horizontal vorticity develops beneath enhanced westerly flow on the south side of the tornado. This vorticity becomes streamwise as the flow turns radially inward toward the tornado. Rapid intensification to tornado strength occurs owing to the combination of these effects.

The substantial impact of surface drag in the genesis of both tornadoes prompted the execution of a simulation in which the surface drag coefficient was set to zero. Substantial differences were seen between this no-drag simulation and the drag simulation, confirming the importance of surface drag. More specifically, the no-drag simulation featured only one tornado that was shorter-lived, developed in a much different manner, and took a substantially different track than the tornadoes in the drag simulation. Vortex line and vorticity budgets along backward trajectories strongly suggest that the origin of rotation in the tornado in the no-drag simulation was tilting and subsequent stretching of the horizontal vorticity associated with the environmental shear.

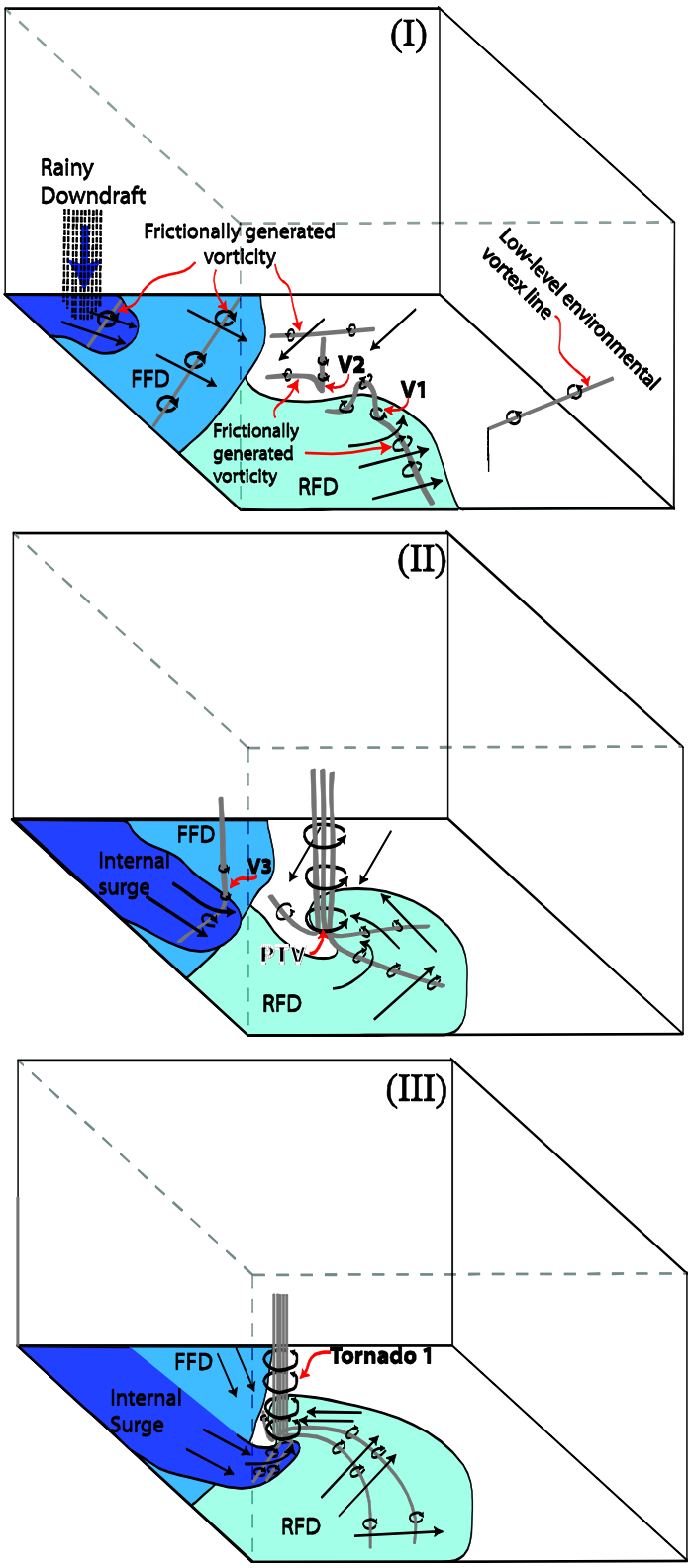

Fig. 4.29. Three-stage conceptual model for the genesis of tornado 1. Gray lines are vortex lines, black vectors are the horizontal wind. The shades of blue from lightest to darkest represent the RFD, FFD, and internal outflow surge.

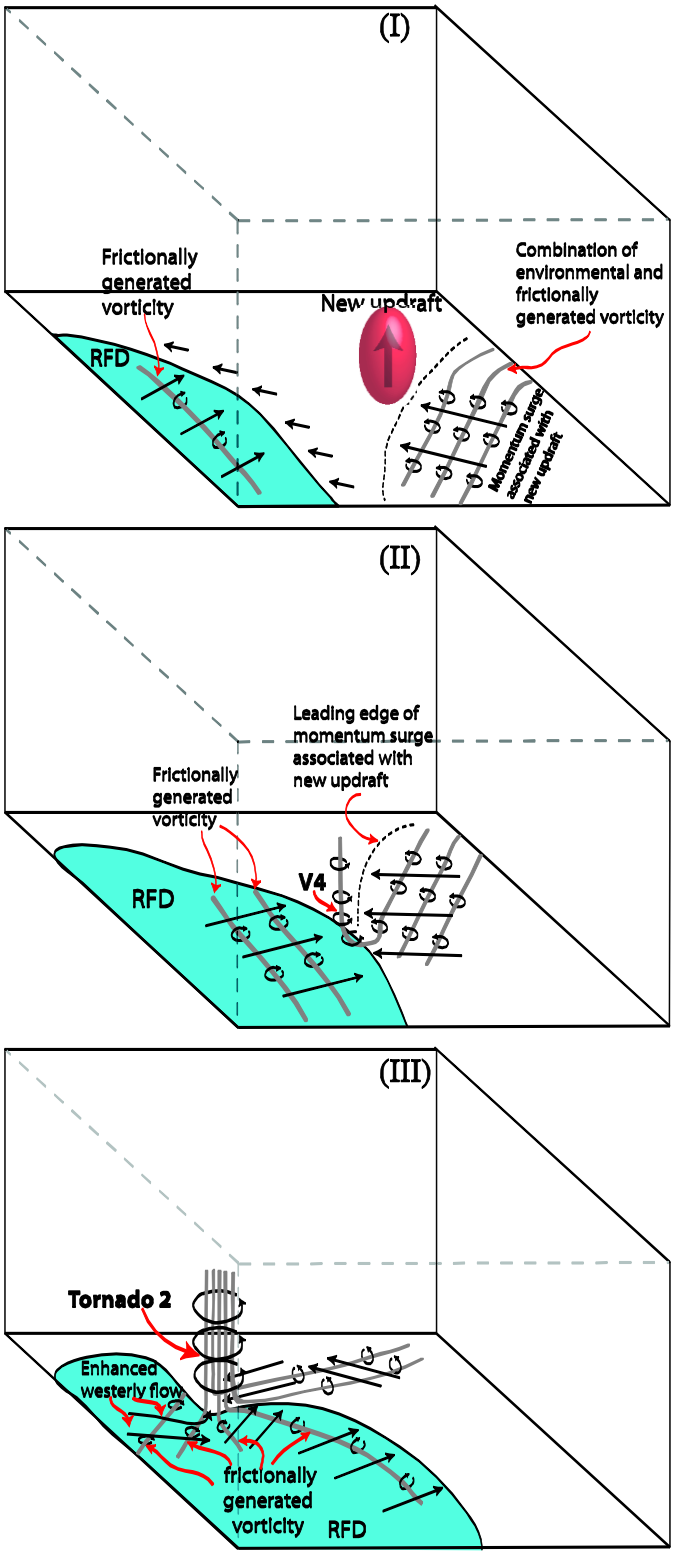

Fig. 4.30. As Fig. 4.29 but for tornado 2. The red oval represents the new updraft in developing the inflow.

Perhaps the most significant finding of the present study was the large role played by surface drag in the origin of vertical vorticity near the ground in the drag simulation. It is important not to overemphasize the exact steps in the conceptual model for tornado 1, as the exact evolution in tornadogenesis is likely strongly case dependent; more important, is the general process whereby frictionally generated vorticity is tilted into the vertical to generate near-surface vertical vorticity. To the author's knowledge, the present study represents the first time that this role of surface drag has been discussed and implicated in tornadogenesis. Future work should examine additional high-resolution simulations of tornadogenesis, with a surface drag parameterization turned on, to determine whether surface drag is playing a similar role. If future simulations confirm the results presented herein, it will be necessary to rethink and reformulate our present understanding of the origin of near-surface vertical vorticity in tornadic supercells.

One hopeful aspect of the importance of surface drag in the present study is it alleviates the necessity for a hand-waving explanation regarding the need for some, but not too much, baroclinity in tornadic supercells. This is not to say that the temperature of the cold pool has no importance in supercells; it simply implies that other processes may be responsible for the origin of near-surface vorticity. It is almost certain that too strong of a cold pool will tend to 'undercut' the storm and lead to its dissipation. Moreover, a cold pool that is too cold may inhibit the lifting of low-level parcels that contain large values of frictionally generated and/or amplified environmental horizontal vorticity. However, this study found that baroclinic vorticity generation did not play a direct role in tornadogenesis in both the drag and no-drag simulations. This is another

area that will require additional simulations to confirm. However, a simplified scale analysis reveals that this finding may not be as surprising as it first seems. Following Klemp and Rotunno (1983), streamwise baroclinically generated vorticity, $\Delta\omega_s$, can be approximated by,

$$\Delta\omega_s \approx \frac{g}{\theta}\frac{\partial\theta}{\partial n}\frac{\Delta s}{v_s} \qquad (4.1)$$

where g is gravity, θ is potentional temperature, s and n are the parallel and perpendicular directions to the flow, and v_s is the storm-relative flow. In order to generate $\Delta\omega_s \sim 0.1$ s^{-1} in 60 s (as was seen for the vorticity budgets presented in figs. 4.11 and 4.17), a temperature gradient of ~ 50 K km^{-1} would be required. This is a very unrealistic magnitude for temperature gradient in supercell cold pools and suggests that drag vorticity will generally be *at least* one order magnitude larger than baroclinically generated vorticity near the ground.

In addition to further simulations, observational data may be able to help confirm or disprove the proposed importance of surface drag. However, given the spatial and temporal scales of the phenomena examined in this study, it will require very high-resolution observations in the lowest 200 m of the atmosphere. Such observations may be possible with a combination of mobile mesonet (or sticknet data) and mobile Doppler radar. Determining whether such a data set presently exists (and analyzing it) is a direction that should be explored in future research.

There are still a number of open questions surrounding tornadogenesis that the mechanism discussed in the present study does not address. The most perplexing of which is determining the difference between tornadic and non-tornadic supercells. It is unlikely that surface drag plays a direct role in this distinction because the bulk impact

of surface drag on the low-level flow should not differ between tornadic and non-tornadic supercells. Data sets from simulated (and possibly observed) non-tornadic supercells should be analyzed in order to examine this problem.

A final area that will be explored further in the future is the role that surface drag plays once the tornado has formed. The present simulation found that large horizontal vorticity was generated via surface drag as the flow accelerated around and into the tornado. This vorticity appeared to feed into and strengthen the tornadic vortex. Future work will examine this aspect of the present simulation in more detail. This effect may also be present in observational data as high-resolution mobile Doppler radar suggests that a strong horizontal vortex may be present to the east and south of an observed EF-5 tornado (J. Houser, Personal communication). This vortex is in the same tornado-relative location as the large streamwise vorticity in the simulation investigated in the present study, suggesting there may be a relationship between the observed feature and surface drag.

The above discussion indicates that many important research questions remain open in the area of tornadogenesis and tornado dynamics. The role of surface drag presented herein may be an important piece in solving some of the remaining puzzles. However, because this is only one simulation, it is *very important* not to overemphasize its generality. Future work should carefully consider the role of surface drag and attempt to further reconcile it with the present understanding and theories for tornadogenesis.

Chapter 5: Errors in Trajectory Calculations

5.1 Introduction

Trajectory analysis has been used heavily to help understand the dynamics of both of the simulations examined in this dissertation. It has also been used for similar purposes in many past studies of high-resolution numerical simulations (e.g., Klemp and Rotunno 1983; Wicker and Wilhelmson 1995; Mashiko et al. 2009). Trajectory calculations are appealing because they allow the investigator to determine the origin of air parcels that reside in features of interest (e.g., tornadoes, updrafts, downdrafts). When used in a numerical simulation, the temporal evolution of thermodynamic and kinematic variables for a parcel can be traced through time along a trajectory.

Although trajectory analysis offers important dynamical insight, it should be used with caution as quickly evolving and high-velocity flows may lead to large spatial errors in trajectory calculations. A recent study by Dahl et al. (2012) explored some of the potential problems with trajectory calculations in a high-resolution simulation of a supercell and associated low-level mesocyclone. By using a model in which forward trajectories are run with the model integration, Dahl et al. (2012) examined errors in backward trajectories calculated using model data output over a range of temporal frequencies. They did this by comparing the backward and forward trajectories with the same end point (start point for the backward trajectory in backward time). They found that backward trajectory calculations resulted in spurious parcels reaching the low-level mesocyclone from the inflow of the supercell. In these backward trajectories, parcels approached the storm from the inflow at low-levels, passed through the gust front, and entered the low-level mesocyclone. No forward trajectories exhibited this behavior,

suggesting that the backward trajectories are spurious and should not be trusted in making dynamical inferences about the processes occurring in the supercell. Spurious inflow backward trajectories were found to occur even when the trajectories were calculated with the same time step as the model integration (dt = 2 s). The reason for this has to do with the convergent nature of the mesocyclone and is discussed in more detail in the following subsection.

In attempt to use accurate backward trajectories in the analysis conducted for the simulations examined in this dissertation, a three-dimensional vorticity budget check was used. Specifically, if the sum of the integrated vorticity source and sink terms for all three vorticity components were qualitatively in close agreement with the interpolated model value along the trajectory, the trajectory was assumed to be accurate. This assumption is likely fairly robust as it is highly unlikely that the vorticity forcing terms (four for each horizontal vorticity component and two for the vertical vorticity component) would coincidentally add up to equal the model vorticity value. In some circumstances, however, no trajectories could be found that passed the vorticity budget check. This occurred for many near-surface parcels in the drag simulation, as well as for parcels that enter the tornado in the no-drag simulation. In these situations, trajectories terminating in the vicinity of (but not within) the features of interest were examined.

5.2 Errors in backward trajectory calculations into convergent features

As described above, the results of Dahl et al. (2012) suggest that convergent flow is less forgiving to errors in backward trajectory calculations than those in forward

trajectory calculations. This problem can be understood by examining a parcel in a simple one-dimensional flow,

$$u = -Ax \tag{5.1}$$

where *u* is the flow velocity, *A* is the divergence, and *x* is the parcel location. It is trivial to show that for this flow the parcel trajectory is described by

$$x(t) = x(0)e^{-At} \tag{5.2}.$$

An expression for the growth of an initial error for a parcel entering the flow described in (5.1) is easily obtained and is given by

$$r(t) = r(0)e^{-At} \tag{5.3}$$

where the error, $r(t)$, is defined as $x_{truth}(t)-x_{calculated}(t)$.

Equation (5.3) implies that for a backward trajectory in convergent flow (i.e., $t<0$ and $A > 0$), an initial error in a trajectory calculation will grow exponentially. Fig. 5.1 plots (eq. 5.3) with $\alpha \equiv -At$.

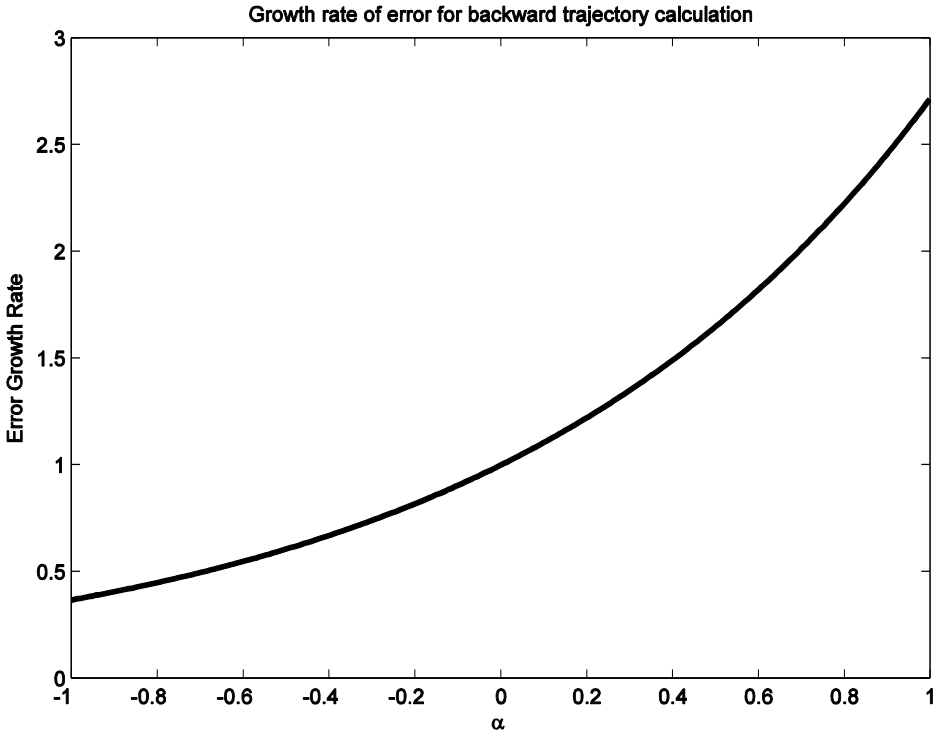

Fig. 5.1. Growth rate of an initial error for a parcel entering an area of divergence/convergence.

In order to understand the implication of the above plot, consider an example where a backward trajectory initialized within a tornado acquires a modest amount of error owing to the curved, high-velocity flow in the tornado. If this trajectory then encounters a strong convergent (divergent in backward time) flow where A=0.1 s^{-1}, the initial error (i.e., the error that was accumulated while the parcel was in the tornado) will double in less than 7 s and increase by an order of magnitude in ~ 23 s. For a forward trajectory the error will be halved in less than 7 s. This simple example shows how errors impact backward trajectories much more severely than forward trajectories in convergent flow and helps explain the results described in Dahl et al. (2012). The opposite effect occurs for backward and forward trajectories in divergent flow.

5.3 Error mitigation

Given that tornadogenesis relies on strong stretching of vorticity, the flow is generally strongly convergent. Moreover, tornadoes tend to form along and/or at the intersection of gust fronts which also tend to have large values of convergence associated with them. This implies that the type of error growth discussed above is common for backward trajectories that terminate in a tornado.

One obvious way to mitigate errors in backward trajectory calculations is to avoid them all together and only perform forward trajectory calculations during the model integration. Unfortunately, it is generally not possible to know a priori where and when forward trajectories would need to be initialized in the model in order to obtain trajectories relevant to tornadogenesis. Such an approach would likely require calculating thousands, if not millions, of trajectories in order to make sure relevant trajectories are obtained. Taken to its limit, this method would approximate a Lagrangian model. This would likely be prohibitively expensive for very high-resolution simulations of tornadic supercells. Moreover, errors in forward trajectory calculations are just as sensitive to divergent flows as backward trajectories are to convergent flows. Thus, if forward parcels with some initial error were to enter a strongly divergent flow (for example, in a strong downdraft near the ground) errors would quickly become large.

Another way to help limit error growth in backward trajectories is to reduce errors that occur as a result of the backward trajectory integration being unable to resolve the speed and temporal evolution of the flow in the tornado (i.e., if the Courant-Friedricks-Lewy, hereafter CFL, condition is not met). In other words, if one could

minimize the errors that occur while the parcel is within the tornado, then when the parcel encounters the convergent zone(s) and gust front(s) near the tornado the initial error will remain small, even if it increases by an order of magnitude. This could be accomplished by using more frequent model output data in the backward integration. In the simulations examined in this dissertation, 2-s data were used for OKC storm and 3-s data were used for the 9 May 2007 mesovortex. While this temporal frequency resulted in some good backward trajectory calculations (as judged by vorticity budget comparisons); many trajectories were still highly inaccurate. In order to increase the number of accurate trajectories one would ideally dump output data even more frequently. However, this becomes very expensive in terms of computational expense owing to the large i/o and disk storage space requirements.

An alternative to increasing the model data availability is to use a sub-interval time step that linearly interpolates between two data availability times. This approach should help reduce error in scenarios in which the flow speed and integration time step leads to violation of the CFL condition. This approach does not impact the exponential growth of errors in convergent zones, but may help increase trajectory accuracy prior to the parcel entering the convergent zone. Unfortunately, preliminary tests with a sub-interval for the simulations discussed herein did not show large improvements, likely because the model output data is already available at a high temporal frequency. This suggests there may be other sources of error in trajectory calculations besides the inability to resolve the temporal and spatial variability of the flow. Determining these errors sources and how to best mitigate them will be considered in future work.

5.4 An alternative to trajectory calculations: Circulation analysis

In a recent paper, Markowski et al. (2012b) used a circulation analysis to examine dual-Doppler synthesized wind fields from a tornadic supercell. This approach was motivated by errors that are typically present in the calculation vorticity forcing terms along trajectories, as well as errors that accumulate owing to poor temporal resolution in the available data. Markowski et al. (2012b) argue that a circulation analysis will help avoid these issues because a 'material circuit' that encloses the area of strong rotation will not be subject to the errors that would occur if trajectories were examined that terminated within a strong vortex.

While the circulation calculations are likely more accurate than direct trajectory calculations for the relatively low-spatial resolution, smoothed dual-Doppler data considered in Markowski et al. (2012b). The justification for the 'material' circuit approach for a high-resolution numerical simulation is likely not valid because circuits become exceedingly complex when integrated backward for any substantial amount of time (i.e., longer than 60 s). In addition, the trajectories that make up the material circuit are also subject to spatial errors which could invalidate the assumption that a material circuit is well-approximated by a ring of parcels traced backward in time.

One way to mitigate the problems with integrating material circuits backward in high-resolution NWP is to smooth the model fields. Smoothing the model fields should improve the accuracy of trajectory calculations and, more importantly, prevent large discontinuities from developing in the circuit. On the other hand, analyses conducted with smoothed data must be interpreted with caution as it is unknown at what point the smoothing will remove features with significant dynamical importance in

tornadogenesis. Further examination of the utility of smoothed high-resolution model data in circulation analyses is planned in the future.

Chapter 6: Summary and Future Work

High-resolution numerical simulations of two case studies were examined in order to determine the important dynamical processes responsible for tornadogenesis. Simulations were conducted using the Advanced Regional Prediction System (ARPS) model and were initialized with real data (including radar data) that were assimilated via the ARPS 3DVAR. Simulations of both case studies forecasted the observed events with good accuracy, closely reproducing the timing and location of tornadogenesis.

The first simulation discussed was of a tornadic mesovortex that occurred in central Oklahoma on 9 May 2007. This simulation had 100-m horizontal grid spacing and forecasted the development of a long-lived mesovortex that spawned a short-lived EF-0 tornado. Detailed examination of the simulation revealed that horizontal vorticity generated by surface drag became concentrated immediately behind a gust front to the northwest of the mesovortex, leading to the development of a strong horizontal rotor. A strong low-level updraft in association with this horizontal rotor caused the concentration of mesovortex low-level vertical vorticity leading to tornadogenesis. The dynamics behind the formation of the rotor were found to closely resemble those responsible for the development of rotors in the lee of mountains for stably stratified flow. An additional simulation was conducted that turned off the surface drag parameterization. This simulation did not produce a rotor, strong low-level updraft, or tornado confirming that surface drag was critical to tornadogenesis in the original simulation.

The discussion of the 9 May 2007 mesovortex was followed by a detailed study of a simulation of the 8 May 2003 Oklahoma City tornadic supercell. This simulation

was run with 50-m horizontal grid spacing and forecasted the development of two tornadoes that tracked within 10 km of the observed Oklahoma City tornado. The first tornado in the simulation reached F-3 intensity and persisted for 13 min, while the second reached F-2 intensity and lasted only ~ 5 min.

As with the simulation of the 9 May 2007 tornadic mesovortex, horizontal vorticity generated by surface drag was found to play an important role in tornadogenesis in the simulated 8 May 2003 OKC supercell. However, instead of leading to the formation of a rotor, drag generated vorticity in the 8 May 2003 simulation was shown to be tilted into the vertical and, for the first tornado, was determined to be the primary source of vorticity for the origin of near-surface rotation. Near-surface rotation for the second tornado originated via the tilting of a combination of environmental and frictionally generated vorticity. Both tornadoes ingested large low-level frictionally generated vorticity within internal RFD surges. For the first tornado this RFD surge was likely caused by evaporation and water loading upstream in the convective core. In contrast, the RFD surge associated with the second tornado appeared to be generated in-situ by the flow accelerating into the developing tornado.

A simulation in which surface drag was turned off was conducted in attempt to verify the importance of surface drag in tornadogenesis. This simulation still produced a tornado, though it was shorter-lived and behaved much differently than the tornadoes in the drag simulation. Examination of the generation of the tornado in the no-drag simulation strongly suggested that it originated along the leading edge of an outflow surge, owing to the tilting of environmental vorticity that was enhanced within the outflow surge. It seems likely that a similar effect should be present in the drag

simulation; however, its impact is likely overwhelmed by the large generation of horizontal vorticity by drag. While the results of the no-drag simulation imply that tornadogenesis is still possible without the inclusion of surface drag, the substantial differences between the drag and no-drag simulation confirm that surface drag has a large impact on the evolution of the tornadic supercell.

Overall, the results presented in this dissertation strongly suggest future work should focus on verifying the importance of surface drag in tornadogenesis. Because no prior research has examined the dynamics associated with mesovortex tornadogenesis, the development and importance of the horizontal rotor described in this dissertation have not been previously identified or discussed. Thus, numerous additional simulations will be required to verify that such a process occurs frequently. In addition, high-resolution observations from mobile Doppler radars may be able to verify or discount the possibility that such a rotor is commonly associated with tornadic mesovortices in the real atmosphere.

Unlike tornadic mesovortices, there has been a great deal of research on tornadic supercells. However, the role of surface drag in generating near-surface rotation (as discussed herein) has not been previously identified. Additional simulations will be necessary to determine whether this process is common in tornadic supercells. Detailed observational studies may also be able to verify the occurrence of this process.

Previous research focused on forecasting tornado potential in supercells has identified several key variables, the most important of which being low-level environmental shear. Future work should examine the sensitivity of the tilting of frictionally generated vorticity to these previously identified important tornado potential

variables. Through such a study it may be possible to better fit the tilting of frictionally generated vorticity within the broader context and knowledge of supercells, their environment, and tornadic potential. This should make it possible to develop a more complete conceptual understanding of tornadogenesis and possibly better discriminate between tornadic and non-tornadic supercells.

References

Adlerman, E. J., 2003: Numerical simulations of cyclic storm behaviors: Mesocyclogenesis and tornadogenesis. Ph.D. Dissertation, School of Meteorology, University of Oklahoma, 219 pp.

Agee, E., and E. Jones, 2009: Proposed conceptual taxonomy for proper identification and classification of tornado events. *Wea. and Forecasting*, **24,** 609-617.

Alexander, C., 2010: A mobile radar based climatology of supercell tornado structures and dynamics, Meteorology, University of Oklahoma, 229 pp.

Atkins, N. T., and M. S. Laurent, 2009a: Bow echo mesovortices. Part I: Processes that influence their damaging potential. . *Mon. Wea. Rev.*, **137,** 1497-1513.

——, 2009b: Bow echo mesovortices. Part II: Their genesis. *Mon. Wea. Rev.*, **137,** 1514-1532.

Atkins, N. T., J. M. Arnott, R. W. Przybylinski, R. A. Wolf, and B. D. Ketcham, 2004: Vortex structure and evolution within bow echoes. Part I: Single-Doppler and damage analysis of the 29 June 1998 derecho. . *Mon. Wea. Rev.*, **132,** 2224-2242.

Atkins, N. T., C. S. Bouchard, R. W. Przybylinski, R. J. Trapp, and G. Schmocker, 2005: Damaging surface wind mechanisms within the 10 June 2003 Saint Louis bow echo during BAMEX. . *Mon. Wea. Rev.*, **133,** 2275-2296.

Barnes, S. L., 1968: On the source of thunderstorm rotation. National Severe Storms Laboratory, 28 pp.

——, 1978: Oklahoma thunderstorms on 29-30 April 1970. Part I: Morphology of a tornadic storm. *Mon. Wea. Rev.*, **106,** 673-684.

Bluestein, H. B., J. G. LaDue, H. Stein, D. Speeder, and W. P. Unruh, 1993: Doppler radar wind spectra of supercell tornadoes. *Mon. Wea. Rev.*, **121,** 2200-2221.

Bluestein, H. B., M. M. French, I. PopStefanija, R. T. Bluth, and J. B. Knorr, 2010: A mobile, phased-array Doppler radar for the study of severe convective storms. *Bulletin of the American Meteorological Society*, **91,** 579-600.

Bluestein, H. B., W. P. Unruh, D. C. Dowell, T. A. Hutchinson, T. M. Crawford, A. C. Wood, and H. Stein, 1997a: Doppler radar analysis of the Northfield, Texas, tornado of 25 May 1994. *Mon. Wea. Rev.*, **125,** 212-230.

Bluestein, H. B., S. G. Gaddy, D. C. Dowell, A. L. Pazmany, J. C. Galloway, R. E. McIntosh, and H. Stein, 1997b: Doppler Radar Observations of Substorm-Scale Vortices in a Supercell. *Mon. Wea. Rev.*, **125,** 1046-1059.

Brady, R. H., and E. Szoke, 1989: A case study of nonmesocyclone tornado development in northeast Colorado: Similarities to wa-terspout formation. *Mon. Wea. Rev.*, **117,** 843-856.

Brandes, E. A., 1978: Mesocyclone evolution and tornadogenesis: Some observations. *Mon. Wea. Rev.*, **106,** 995-1011.

——, 1981: Finestructure of the Del City-Edmond tornadic meso-circulation. *Mon. Wea. Rev.*, **109,** 635-647.

——, 1984: Vertical vorticity generation and mesocyclone suste-nance in tornadic thunderstorms: The observational evidence. *Mon. Wea. Rev.*, **112,** 2253-2269.

Brewster, K., 1996: Application of a Bratseth analysis scheme including Doppler radar data. *Preprints, 15th Conf. Wea. Anal. Forecasting*, Norfolk, VA, Amer. Meteor. Soc., 92-95.

——, 2002: Recent advances in the diabatic initialization of a non-hydrostatic numerical model. *Preprints, 15th Conf Num. Wea. Pred./ 21st Conf Severe Local Storms*, San Antonio, TX, Amer. Meteor. Soc., J6.3.

Brock, F. V., G. Lesins, and R. Walko, 1987: Measurements of pressure and air temperature near severe thunderstorms: An inexpensive and portable instrument. Extended Abstracts. *Sixth Symp. on Meteorological Observations and Instrumentation*, Amer. Meteor. Soc., 320-323.

Brock, F. V., K. C. Crawford, R. L. Elliott, G. W. Cuperus, S. J. Stadler, H. L. Johnson, and M.D. Eilts, 1995: The Oklahoma Mesonet: A technical overview. *J. Atmos. Oceanic Tech.*, **12,** 5-19.

Brooks, H. E., C. A. Doswell, and R. Davies-Jones, 1993: Environmetal helicity and the maintenance and evolution of low-level mesocyclones. *The Tornado: Its Structure, Dynamics, Prediction and Hazards*, C. R. Church, Ed., Amer. Geophys. Union Press, 97-104.

Brooks, H. E., C. A. Doswell III, and J. Cooper, 1994: On the environments of tornadic and nontornadic mesocyclones. *Wea. Forecasting*, **9,** 606-618.

Brown, R. A., D. W. Burgess, and K. C. Crawford, 1973: Twin tornado cyclones within a severe thunderstorm: Single-Dopper radar observations. *Weatherwise*, **26,** 63-71.

Brown, R. A., L. R. Lemon, and D. W. Burgess, 1978: Tornado detection by pulsed Doppler radar. *Mon. Wea. Rev.*, **106,** 29-38.

Browning, K. A., 1964: Airflow and precipitation trajectories within severe local storms which travel to the right of the mean winds. *J. Atmos. Sci.*, **21,** 634-639.

Browning, K. A., and R. J. Donaldson, 1963: Airflow and structure of a tornadic storm. *J. Atmos. Sci.*, **20,** 533-545.

Bunkers, M. J., B. A. Klimowski, J. W. Zeitler, R. L. Thompson, and M. L. Weisman, 2000: Predicting supercell motion using a new hodograph technique. *Wea. Forecasting*, **15,** 61-79.

Burgess, D. W., R. J. Donaldson, Jr., and P. R. Desrochers, 1993: Tornado detection and warning by radar. *The Tornado: Its Structure, Dynamics, Prediction and Hazards*, C. Church, D. Burges, C. Doswell, and R. Davies-Jones, Eds., Amer. Geophys. Union, 203-221.

Burgess, D. W., L. D. Hennington, R. J. Doviak, and P. S. Ray, 1976: Multi-moment Doppler display for severe storm identification. *J. Appl. Meteor.*, **15,** 1302-1306.

Burgess, D. W., R. A. Brown, L. R. Lemon, and C. R. Safford, 1977: Evolution of a tornadic thunderstorm. *Preprints Tenth Conf. on Severe Local Storms*, Amer. Meteor Soc., 84-89.

Byko, Z., P. M. Markowski, Y. Richardson, J. Wurman, and E. Adlerman, 2009: Descending reflectivity cores in supercell thunderstorms observed by mobile radars and in a high-resolution numerical simulation. *Wea. and Forecasting*, **24,** 155-186.

Chen, F., and J. Dudhia, 2001: Coupling an advanced land surface-hydrology model with the Penn State-NCAR MM5 modeling system. Part I: Model implementation and sensitivity. *Mon. Wea. Rev.*, **129,** 569.

Dahl, J. M. L., M. D. Parker, and L. J. Wicker, 2012: Uncertainties in trajectory calculations within near-surface mesocyclones of simulated supercells. *Mon. Wea. Rev.*, **140,** 2959-2966.

Davies-Jones, R., 2008: Can a descending rain curtain in a supercell instigate tornadogenesis barotropically? *J. Atmos. Sci.*, **65,** 2469-2496.

Davies-Jones, R., D. W. Burgess, and M. Foster, 1990: Test of helicity as a tornado forecast parameter. *16th Conf. Severe Local Storms*, Amer. Meteor. Sec., 216-219.

Davies-Jones, R. P., 1984: Streamwise vorticity: The origin of updraft rotation in supercell storms. *J. Atmos. Sci.*, **41,** 2991-3006.

Davies-Jones, R. P., and H. Brooks, 1993: Mesocyclogenesis from a theoretical perspective. *The Tornado: Its Structure, Dynamics, Prediction, and Hazards*, C. R. Church, Ed., Amer. Geophys. Union Press, 105-114.

Davis, C., and Coauthors, 2004: The bow echo and MCV experiment: Observations and opportunities. *Bulletin of the American Meteorological Society*, **85,** 1075-1093.

Dowell, D. C., and H. B. Bluestein, 1997: The Arcadia, Oklahoma, storm of 17 May 1981: Analysis of a supercell during tornadogenesis. *Mon. Wea. Rev.*, **125,** 2562-2582.

Dowell, D. C., and L. J. Wicker, 2009: Additive noise for storm-scale ensemble data assimilation. *J. Atmos. Oceanic Technol.*, **26,** 911-927.

Dowell, D. C., L. J. Wicker, and C. Snyder, 2011: Ensemble Kalman filter assimilation of radar observations of the 8 May 2003 Oklahoma City supercell: Influence of reflectivity observations on storm-scale analysis. *Mon. Wea. Rev.*, **139,** 272-294.

Doyle, J., and D. R. Durran, 2002: The dynamics of mountain-wave induced rotors. *J. Atmos. Sci.*, **59,** 186-201.

——, 2007: Rotor and subrotor dynamics in the lee of three-dimensional terrain. *J. Atmos. Sci.*, **64,** 4202–4221.

Evensen, G., 1994: Sequential data assimilation with a nonlinear quasi-geostrophic model using Monte Carlo methods to forecast error statistics. *J. Geophys. Res.*, **99,** 10143-10162.

Fiedler, B., 1994: The thermodynamic speed limit and its violation in axisymmetric numerical simulations of tornado-like vortices. *Atmos. Ocean*, **32,** 335-359.

Fiedler, B. H., and R. Rotunno, 1986: A theory for the maximum windspeeds in tornado-like vortices. *J. Atmos. Sci.*, **43,** 2328-2340.

Forbes, G. S., and R. M. Wakimoto, 1983: A concentrated outbreak of tornadoes, downbursts and microbursts, and implications regarding vortex classification. *Mon. Wea. Rev.*, **111,** 220-235.

Frame, J., and P. M. Markowski, 2010: Numerical simulations of radiative cooling beneath the anvils of supercell thunderstorms. *Mon. Wea. Rev.*, **138,** 3024-3047.

French, M. M., 2012: Mobile, phased-array, Doppler radar observations of tornadoes at X band. Ph. D Dissertation, University of Oklahoma, 322 pp.

Fujita, T., 1978: Manual of downburst identification for project NIMROD, 104 pp pp.

Fujita, T. T., 1958: Mesoanalysis of the Illinois tornadoes of 9 April 1953. *J. Meteor.*, **15,** 288-296.

——, 1965: Formation and steering mechanisms of tornado cyclones and associated hook echoes. *Mon. Wea. Rev.*, **93,** 67-78.

Fujita, T. T., and H. Grandoso, 1968: Split of a thunderstorm into anticyclonic and cyclonic storms and their motion as determined from numerical model experiments. *J. Atmos. Sci.*, **25,** 416439.

Gao, J.-D., M. Xue, K. Brewster, and K. K. Droegemeier, 2004: A three-dimensional variational data analysis method with recursive filter for Doppler radars. *J. Atmos. Ocean. Tech.*, **21,** 457-469.

Gao, J., and D. J. Stensrud, 2012: Assimilation of reflectivity data in a convective-scale, cycled 3DVAR framework with hydrometeor classification. *J. Atmos. Sci.*, **69,** 1054-1065.

Golden, J. H., 1971: Waterspouts and tornadoes over south Florida. *Mon. Wea. Rev.*, **99,** 146-154.

Grasso, L. D., and W. R. Cotton, 1995: Numerical simulation of a tornado vortex. *J. Atmos. Sci.*, **52,** 1192-1203.

Grzych, M. L., B. D. Lee, and C. A. Finley, 2007: Thermodynamic analysis of supercell rear-flank downdrafts from project ANSWERS. *Mon. Wea. Rev.*, **135,** 240-246.

Hamill, T. M., R. S. Schneider, H. E. Brooks, G. S. Forbes, H. B. Bluestein, M. Steinberg, D. Melendez, and R. M. Dole, 2005: The May 2003 extended tornado outbreak. *Bulletin of the American Meteorological Society*, **86,** 531-542.

Hu, M., and M. Xue, 2007: Impact of configurations of rapid intermittent assimilation of WSR-88D radar data for the 8 May 2003 Oklahoma City tornadic thunderstorm case. *Mon. Wea. Rev.*, **135,** 507–525.

Hu, M., M. Xue, and K. Brewster, 2006: 3DVAR and cloud analysis with WSR-88D level-II data for the prediction of Fort Worth tornadic thunderstorms. Part I: Cloud analysis and its impact. *Mon. Wea. Rev.*, **134,** 675-698.

Kerr, B. W., and G. L. Darkow, 1996: Storm-relative winds and helicity in the tornadic thunderstorm environment. *Wea. and Forecasting*, **11,** 489-505.

Kessler, E. I., 1969: *On the distribution and continuity of water substance in atmospheric circulations.* Amer. Meteor. Soc., 84 pp.

Klemp, J. B., and R. B. Wilhelmson, 1978a: Simulations of right- and left-moving thunderstorms produced through storm splitting. *J. Atmos. Sci.*, **35,** 1097-1110.

——, 1978b: The simulation of three-dimensional convective storm dynamics. *J. Atmos. Sci.*, **35,** 1070-1096.

Klemp, J. B., and R. Rotunno, 1983: A study of the tornadic region within a supercell thunderstorm. *J. Atmos. Sci.*, **40,** 359-377.

Klemp, J. B., R. B. Wilhelmson, and P. S. Ray, 1981: Observed and numerically simulated structure of a mature supercell thunderstorm. *J. Atmos. Sci.*, **38,** 1558-1580.

Kosiba, K., J. Wurman, Y. Richardson, P. M. Markowski, P. Robinson, and J. Marquis, 2012: Genesis of the Goshen County, Wyoming tornado on 05 June 2009 during VORTEX2. *Mon. Wea. Rev.*, in press.

Kumjian, M. R., and A. V. Ryzhkov, 2008: Polarimetric signatures in supercell thunderstorms. *J. Appl. Meteor. Climatol.*, **47,** 1940-1961.

——, 2009: Storm-relative helicity revealed from polarimetric radar measurements. *J. Atmos. Sci.*, **66,** 667-685.

Lee, B. D., and R. B. Wilhelmson, 1997a: The numerical simulation of non-supercell tornadogenesis. Part I: Initiation and evolution of pretornadic misocyclone circulations along a dry outflow boundary. *J. Atmos. Sci.*, **54,** 32-60.

——, 1997b: The numerical simulation of non-supercell tornadogenesis. Part II: Evolution of a family of tornadoes along a weak outflow boundary. *J. Atmos. Sci.*, **54,** 2387-2415.

Lee, B. D., C. A. Finley, and R. B. Wilhelmson, 2000: Simulating deep convection initiation by misocyclones. Preprints. *20th Conf. Severe Local Storms*, Amer. Meteor. Soc.

Lee, B. D., C. A. Finley, and T. M. Samaras, 2011: Surface analysis near and within the Tipton, Kansas, tornado on 29 May 2008. *Mon. Wea. Rev.*, **139**.

Lee, B. D., C. A. Finley, and C. D. Karstens, 2012: The Bowdle, South Dakota, cyclic tornadic supercell of 22 May 2012: Suface analysis of rear-flank downdraft evolution and multiple internal surges. *Mon. Wea. Rev.*, in press.

Lemon, L. R., 1976: Wake vortex structure and aerodynamic origin in severe thunderstorms. *J. Atmos. Sci.*, **33,** 678-685.

——, 1977: New severe thunderstorm radar identification techniques and warning criteria: A preliminary report. NOAA tech. memo. NWS-NSSFC 1, 60 pp.

Lemon, L. R., and C. A. Doswell, 1979: Severe thunderstorm evolution and mesocyclone structure as related to tornadogenesis. *Mon. Wea. Rev.*, **107,** 1184-1197.

Lemon, L. R., D. W. Burgess, and R. A. Brown, 1978: Tornadic storm airflow and morphology derived from single Doppler radar measurements. *Mon. Wea. Rev.*, **106,** 48-61.

Leslie, L. M., 1971: The development of concentrated vortices: A numerical study. *J. Fluid Mech.*, **48,** 1-21.

Lewellen, W. S., D. C. Lewellen, and R. I. Sykes, 1997: Large-eddy simulation of a tornado's interaction with the surface. *J. Atmos. Sci.*, **54,** 581-605.

Lilly, D. K., 1986: The structure, energetics and propagation of rotating convective storms. Part II: Helicity and storm stabilization. *J. Atmos. Sci.*, **43,** 126-140.

Lin, Y.-L., R. D. Farley, and H. D. Orville, 1983: Bulk parameterization of the snow field in a cloud model. *J. Climat. Appl. Meteor.*, **22,** 1065-1092.

Liu, S., M. Xue, and Q. Xu, 2007: Using wavelet analysis to detect tornadoes from Doppler radar radial-velocity observations. *J. Atmos. Ocean Tech.*, **24,** 344-359.

Mak, M., 2001: Nonhydrostatic barotropic instability: Applicability to nonsupercell tornadogenesis. *J. Atmos. Sci.*, **59,** 1209-1225.

Markowski, P., Y. Richardson, J. Marquis, J. Wurman, K. Kosiba, P. Robinson, D. Dowell, E. Rasmussen, and R. Davies-Jones, 2012a: The pretornadic phase of the Goshen County, Wyoming, supercell of 5 June 2009 intercepted by VORTEX2. Part I: Evolution of kinematic and surface thermodynamic fields. *Mon. Wea. Rev.*, **140,** 2887-2915.

——, 2012b: The pretornadic phase of the Goshen County, Wyoming, supercell of 5 June 2009 intercepted by VORTEX2. Part II: Intensification of low-level rotation. . *Mon. Wea. Rev.*, **140,** 2916-2938.

Markowski, P. M., 2002: Mobile mesonet observations on 3 May 1999. *Wea. Forecasting*, **17,** 430–444.

Markowski, P. M., and Y. Richardson, 2009: Tornadogenesis: Our current understanding, forecasting considerations, and questions to guide future research. *Atmospheric Research*, **93,** 3-10.

Markowski, P. M., and N. Dotzek, 2010: Comments on "Proposed conceptual taxonomy for proper identification and classification of tornado events". *Wea. and Forecasting*, **25,** 338-340.

Markowski, P. M., and Y. Richardson, 2010: *Mesoscale meteorology in midlatitudes.* Wiley, 430 pp.

Markowski, P. M., E. Rasmussen, and J. Straka, 1998a: The occurence of tornadoes in supercells interacting with boundaries during VORTEX-95. *Wea. and Forecasting*, **13,** 852-859.

Markowski, P. M., J. M. Straka, and E. N. Rasmussen, 2002: Direct surface thermodynamic observations within the rear-flank downdrafts of nontornadic and tornadic supercells. *Mon. Wea. Rev.*, **130,** 1692-1721.

Markowski, P. M., J. M. Straka, and E. N. Rasmussen, 2003a: Tornadogenesis resulting from the transport of circulation by a downdraft: Idealized numerical simulations. *J. Atmos. Sci.*, **60,** 795-823.

Markowski, P. M., E. N. Rasmussen, J. M. Straka, and D. C. Dowell, 1998b: Observations of low-level baroclinity generated by anvil shadows. *Mon. Wea. Rev.*, **126,** 2942-2958.

Markowski, P. M., M. Majcen, Y. Richardson, J. Marquis, and J. Wurman, 2011: Characteristics of the wind field in a trio of nontornadic low-level mesocyclones observed by the doppler on wheels radars. *Electronic J. Severe Storms Meteor.*, **6 (3),** 1-48.

Markowski, P. M., E. Rasmussen, J. Straka, R. Davies-Jones, Y. Richardson, and R. J. Trapp, 2008: Vortex lines within low-level mesocyclones obtained from pseudo-dual-Doppler radar observations. *Mon. Wea. Rev.*, **136,** 3513-3535.

Markowski, P. M., C. Hannon, J. Frame, E. Lancaster, A. Pietrycha, R. Edwards, and R. L. Thompson, 2003b: Characteristics of vertical wind profiles near supercells obtained from the Rapid Update Cycle. *Wea. and Forecasting*, **18,** 1262-1272.

Marquis, J., Y. Richardson, and J. Wurman, 2007: Kinematic observations of misocyclones along boundaries during IHOP. *Mon. Wea. Rev.*, **135,** 1749-1768.

Marquis, J., Y. Richardson, J. Wurman, and P. M. Markowski, 2008: Single- and dual-Doppler analysis of a tornadic vortex and surrounding storm-scale flow in the Crowell, Texas, supercell of 30 April 2000. *Mon. Wea. Rev.*, **136,** 5017-5043.

Marquis, J., Y. Richardson, P. M. Markowski, D. Dowell, and J. Wurman, 2012: Tornado maintenance investigated with high-resolution dual-Doppler and EnKF analysis. *Mon. Wea. Rev.*, **140,** 3-27.

Marwitz, J. D., 1972: The structure and motion of severe hailstorms. Part I: Supercell storms. *J. Appl. Meteor.*, **11,** 166-179.

Mashiko, W., H. Niino, and K. Teruyuki, 2009: Numerical simulations of tornadogenesis in an outer-rainband minisupercell of typhoon Shanshan on 17 September 2006. *Mon. Wea. Rev.*, **137,** 4238-4260.

McLaughlin, D., and Coauthors, 2009: Short-wavelength technology and the potential for distributed networks of small radar systems. *Bulletin of the American Meteorological Society*, **90,** 1797-1817.

Noilhan, J., and S. Planton, 1989: A simple parameterization of land surface processes for meteorological models. *Mon. Wea. Rev.*, **117,** 536-549.

Orlanski, I., 1975: A rational subdivision of scales for atmospheric processes. *Bulletin of the American Meteorological Society*, **56,** 527-530.

Potvin, C. K., A. Shapiro, T.-Y. Yu, J. Gao, and M. Xue, 2009: Using a low-order model to detect and characterize tornadoes in multiple-Doppler radar data. *Mon. Wea. Rev.*, **137,** 1230-1249.

Przybylinski, R. W., 1995: The bow echo: Observations, numerical simulations, and severe weather detection methods. *Wea. and Forecasting*, **10,** 203-218.

Rasmussen, E., 2003: Refined supercell and tornado forecast parameters. *Wea. and Forecasting*, **18,** 530-535.

Rasmussen, E., and D. O. Blanchard, 1998: A baseline climatology of sounding-derived supercell and tornado forecast parameters. *Wea. and Forecasting*, **13,** 1148-1164.

Rasmussen, E. A., J. M. Straka, R. P. Davies-Jones, C. E. D. III, F. Carr, M. Eilts, and D. R. MacGorman, 1994: Verification of the Origins of Rotation in Tornadoes Experiment: VORTEX. *Bulletin of the American Meteorological Society*, **75,** 1-12.

Rasmussen, E. N., S. Richardson, J. M. Straka, P. M. Markowski, and D. O. Blanchard, 2000: The association of significant tornadoes with a baroclinic boundary on 2 June 1995. *Mon. Wea. Rev.*, **128,** 174-191.

Rogers, R. R., and M. K. Yau, 1989: *A Short Course in Cloud Physics.* 3rd ed. Pergamon Press, 293 pp.

Romine, G. S., D. W. Burgess, and R. B. Wilhelmson, 2008: A dual-polarization-radar-based assessment of the 8 May 2003 Oklahoma City area tornadic supercell. *Mon. Wea. Rev.*, **136,** 2849-2870.

Rotunno, R., 1981: On the evolution of thunderstorm rotation. *Mon. Wea. Rev.*, **109,** 171-180.

Rotunno, R., and J. B. Klemp, 1982: The influence of the shear-induced pressure gradient on thunderstorm motion. *Mon. Wea. Rev.*, **110,** 136-151.

——, 1985: On the rotation and propagation of simulated supercell thunderstorms. *J. Atmos. Sci.*, **42,** 271-292.

Rust, W. D., R. Davies-Jones, D. W. Burgess, R. A. Maddox, L. C. Showell, T. C. Marshall, and D. K. Lauritsen, 1990: Testing a mobile version of a Cross-Chain Loran Atmospheric (M-CLASS) Sounding System. *Bulletin of the American Meteorological Society*, **71,** 173-180.

Ryzhkov, A. V., T. J. Schuur, D. W. Burgess, and D. S. Zrnic, 2005: Polarimetric tornado detection. *J. Appl. Meteor.*, **44,** 557-570.

Schenkman, A., M. Xue, A. Shapiro, K. Brewster, and J. Gao, 2011a: Impact of CASA radar and Oklahoma mesonet data assimilation on the analysis and prediction of tornadic mesovortices in a MCS. *Mon. Wea. Rev.*, **139,** 3422-3445.

——, 2011b: The analysis and prediction of the 8-9 May 2007 Oklahoma tornadic mesoscale convective system by assimilating WSR-88D and CASA radar data using 3DVAR. *Mon. Wea. Rev.*, **139,** 224-246.

Schenkman, A. D., M. Xue, and A. Shapiro, 2012: Tornadogenesis in a simulated mesovortex within a mesoscale convective system. *J. Atmos. Sci.***,** in press.

Schlesinger, R. E., 1975: A three-dimensional numerical model of an isolated deep convective cloud: Preliminary results. *J. Atmos. Sci.*, **32,** 934-957.

——, 1980: A three-dimensional numerical model of an isolated thunderstorm. Part II: Dynamics of updraft splitting and mesovortex couplet evolution. *J. Atmos. Sci.*, **37,** 395-420.

Shabbot, C. J., and P. M. Markowski, 2006: Surface in situ observations within the outflow of forward-flank downdrafts of supercell thunderstorms. *Mon. Wea. Rev.*, **2006,** 1422-1441.

Shapiro, A., K. M. Willingham, and C. K. Potvin, 2010: Spatially variable advection correction of radar data. Part II: Test results. *J. Atmos. Sci.*, **67,** 3457-3470.

Skinner, P. S., C. C. Weiss, J. L. Shroeder, L. Wicker, and M. I. Biggerstaff, 2011: Observations of the surface boundary structure within the 23 May 2007 Perryton, Texas, supercell. *Mon. Wea. Rev.*, **139,** 3730-3749.

Smith, R. K., and L. M. Leslie, 1978: Tornadogenesis. *Quart. J. Roy. Meteor. Soc.*, **104,** 189-199.

——, 1979: A numerical study of tornadogenesis in a rotating thunderstorm. *Quart. J. Roy. Meteor. Soc.*, **105**.

Snook, N., and M. Xue, 2008: Effects of microphysical drop size distribution on tornadogenesis in supercell thunderstorms. *Geophy. Res. Letters*, **35,** L24803, doi:24810.21029/22008GL035866.

Stout, G. E., and F. A. Huff, 1953: Radar records Illinois tornadogenesis. *Bulletin of the American Meteorological Society*, **34,** 281-284.

Straka, J., E. Rasmussen, and S. Frederickson, 1996: A mobile mesonet for finescale meteorological observations. *J. Atmos. Oceanic Technol.*, **13,** 921-936.

Straka, J. M., E. N. Rasmussen, R. P. Davies-Jones, and P. M. Markowski, 2007: An observational and idealized numerical examination of low-level counter-rotating vortices in the rear flank of supercells. *Electronic J. Severe Storms Meteor.*, **2 (8),** 1-22.

Thompson, R. L., C. M. Mead, and R. Edwards, 2007: Effective storm-relative helicity and bulk shear in supercell tornado environments.

Trapp, R. J., 1999: Observations of nontornadic low-level mesocyclones and attendant tornadogenesis failure during VORTEX. *Mon. Wea. Rev.*, **127,** 1693-1705.

Trapp, R. J., and B. Fiedler, 1995: Tornado-like vortexgenesis in a simplified numerical model. *J. Atmos. Sci.*, **52,** 3757-3778.

Trapp, R. J., and M. L. Weisman, 2003: Low-level mesovortices within squall lines and bow echoes. Part II: Their genesis and implications. *Mon. Wea. Rev.*, **131,** 2804-2823.

Trapp, R. J., G. J. Stumpf, and K. L. Manross, 2005a: A reassessment of the percentage of tornadic mesocyclones. *Wea. and Forecasting*, **20,** 680-687.

Trapp, R. J., S. A. Tessendorf, E. S. Godfrey, and H. E. Brooks, 2005b: Tornadoes from squall lines and bow echoes. Part I: Climatological distribution. *Wea. Forecasting*, **20,** 23-34.

Wakimoto, R. M., and J. W. Wilson, 1989: Non-supercell tornadoes. *Mon. Wea. Rev.*, **117,** 1113-1140.

Wakimoto, R. M., and N. T. Atkins, 1996: Observations of the origins of rotation: The Newcastle tornado during VORTEX 94. *Mon. Wea. Rev.*, **124,** 384-407.

Wakimoto, R. M., and C. Liu, 1998: The Garden City, Kansas, storm during VORTEX 95. Part II: The wall cloud and tornado. *Mon. Wea. Rev.*, **126,** 393-408.

Wakimoto, R. M., and H. Cai, 2000: Analysis of a nontornadic storm during VORTEX 95. *Mon. Wea. Rev.*, **128,** 565-592.

Wakimoto, R. M., C. Liu, and H. Cai, 1998: The Garden City, Kansas, storm during VORTEX 95. Part I: Overview of the storm's life cycle and mesocyclogenesis. *Mon. Wea. Rev.*, **126,** 372-392.

Wakimoto, R. M., H. V. Murphey, C. A. Davis, and N. T. Atkins, 2006a: High winds generated by bow echoes. Part II: The relationship between the mesovortices and damaging straight-line winds. *Mon. Wea. Rev.*, **134,** 2813-2829.

Wakimoto, R. M., W. C. Lee, H. B. Bluestein, C. H. Liu, and P. H. Hildebrand, 1996: ELDORA observations during VORTEX 95. *Bulletin of the American Meteorological Society*, **77**.

Wakimoto, R. M., H. V. Murphey, A. Nester, D. P. Jorgensen, and N. T. Atkins, 2006b: High winds generated by bow echoes. Part I: Overview of the Omaha bow echo 5 July 2003 storm during BAMEX. *Mon. Wea. Rev.*, **134,** 2793-2812.

Wang, Y., T.-Y. Yu, M. Yeary, A. Shapiro, S. Nemati, M. Foster, D. L. J. Andra, and M. Jain, 2008: Tornado detection using a neur-fuzzy system to integrate shear and spectral signatures. *J. Atmos. Oceanic Technol.*, **25,** 1136-1148.

Weisman, M. L., and C. A. Davis, 1998: Mechanisms for the generation of mesoscale vortices within quasi-linear convective systems. *J. Atmos. Sci.*, **55,** 2603-2622.

Weisman, M. L., and R. J. Trapp, 2003: Low-level mesovortices within squall lines and bow echoes. Part I: Overview and dependence on environmental shear. *Mon. Wea. Rev.*, **131,** 2779-2803.

Wheatley, D. M., and R. J. Trapp, 2008: The effect of mesoscale heterogeneity on the genesis and structure of mesovortices within quasi-linear convective systems. *Mon. Wea. Rev.*, **136,** 4220-4241.

Wheatley, D. M., R. J. Trapp, and N. T. Atkins, 2006: Radar and damage analysis of severe bow echoes observed during BAMEX. *Mon. Wea. Rev.*, **134,** 791-806.

Wicker, L. J., and R. B. Wilhelmson, 1995: Simulation and analysis of tornado development and decay within a three-dimensional supercell thunderstorm. *J. Atmos. Sci.*, **52,** 2675-2703.

Wilczak, J. M., and T. W. Christian, 1990: Case study of an orographically induced mesoscale vortex (Denver cyclone). *Mon. Wea. Rev.*, **118,** 1082-1102.

Wilhelmson, R. B., and J. B. Klemp, 1978: A numerical study of storm splitting that leads to long-lived storms. *J. Atmos. Sci.*, **35,** 1975-1986.

Wurman, J., Y. Richardson, C. Alexander, S. Weygandt, and P. F. Zhang, 2007: Dual-Doppler and single-Doppler analysis of a tornadic storm undergoing mergers and repeated tornadogenesis. *Mon. Wea. Rev.*, **135,** 736-758.

Wurman, J., K. Kosiba, P. M. Markowski, Y. Richardson, D. Dowell, and P. Robinson, 2010: Finescale single- and dual-Doppler analysis of tornado intensification, maintenance, and dissipation in the Orleans, Nebraska, supercell. *Mon. Wea. Rev.*, **138,** 4439-4455.

Wurman, J., D. dowell, Y. Richardson, P. M. Markowski, E. Rasmussen, D. W. Burgess, L. Wicker, and H. B. Bluestein, 2012: The second verification of the origins of rotation in tornadoes experiment: VORTEX2. *Bulletin of the American Meteorological Society*, **93,** 1147-1170.

Xue, M., and W. J. Martin, 2006: A high-resolution modeling study of the 24 May 2002 case during IHOP. Part I: Numerical simulation and general evolution of the dryline and convection. *Mon. Wea. Rev.*, **134,** 149–171.

Xue, M., K. K. Droegemeier, and V. Wong, 2000: The Advanced Regional Prediction System (ARPS) - A multiscale nonhydrostatic atmospheric simulation and prediction tool. Part I: Model dynamics and verification. *Meteor. Atmos. Physics*, **75,** 161-193.

Xue, M., K. K. Droegemeier, V. Wong, A. Shapiro, and K. Brewster, 1995: *ARPS Version 4.0 User's Guide.* [Available at http://www.caps.ou.edu/ARPS], 380 pp.

Xue, M., D.-H. Wang, J.-D. Gao, K. Brewster, and K. K. Droegemeier, 2003: The Advanced Regional Prediction System (ARPS), storm-scale numerical weather prediction and data assimilation. *Meteor. Atmos. Physics*, **82,** 139-170.

Xue, M., K. K. Droegemeier, V. Wong, A. Shapiro, K. Brewster, F. Carr, D. Weber, Y. Liu, and D. Wang, 2001: The Advanced Regional Prediction System (ARPS) - A multi-scale nonhydrostatic atmospheric simulation and prediction tool. Part II: Model physics and applications. *Meteor. Atmos. Phys.*, **76,** 143-166.

Zhang, J., 1999: Moisture and Diabatic Initialization Based on Radar and Satellite Observation. Ph.D., School of Meteorology, University of Oklahoma, 194 pp.

Zhang, J., F. Carr, and K. Brewster, 1998: ADAS cloud analysis. *Preprints, 12th Conf. on Num. Wea. Pred.*, Phoenix, AZ., Amer. Met. Soc., 185-188.

Zhao, K., and M. Xue, 2009: Assimilation of coastal Doppler radar data with the ARPS 3DVAR and cloud analysis for the prediction of Hurricane Ike (2008). *Geophy. Res. Lett.***,** doi:10.1029/2009GL038658.

Appendix A: The ARPS 3DVAR and Cloud Analysis[12]

A.1 The ARPS 3DVAR

The ARPS 3DVAR minimizes a cost function that includes the background, observation and mass conservation constraint terms. Following Gao et al. (2004), this cost function may be written as

$$J(x) = \frac{1}{2}(\mathbf{x}-\mathbf{x}_b)^T \mathbf{B}^{-1}(\mathbf{x}-\mathbf{x}_b) + \frac{1}{2}[H(\mathbf{x})-\mathbf{y}_o]^T \mathbf{R}^{-1}[H(\mathbf{x})-\mathbf{y}_o] + J_c \qquad \text{(A1)}$$

where the first term measures the departure of the analysis vector, **x**, from the background vector, $\mathbf{x}_b$, weighted by the inverse of the background error covariance matrix **B**, the second term measures the departure of **x**, projected into observation space by H, from the observation vector $\mathbf{y}_o$. The third term in (1), J_c, is a penalty term consisting of a weak mass divergence constraint imposed on the analyzed wind field to help constrain wind components that are perpendicular to the radar beam [see Gao et al (2004) and Hu et al. (2006b) for more details]. The analysis vector, **x**, includes the three wind components (u, v, and w), potential temperature (θ), pressure (p) and water vapor mixing ratio (q_v). Hydrometeors are not analyzed variationally. Because no appropriate balance condition between analysis variables exists at the convective scales modeled in this study, the cross-correlations between variables are not included in **B**. In addition, flow-dependent spatial covariance structures are generally not available in a 3DVAR framework. In the ARPS 3DVAR, the spatial covariance of background error is assumed Gaussian, spatially homogeneous and isotropic. It is modeled using a one-

[12] The descriptions within this appendix are adapted from Schenkman et al. (2011b).

dimensional recursive filter applied successively in each of the three directions. The interested reader is referred to Gao et al. (2004) for more details on the use of recursive filters and the practical implementation of the cost function minimization (e.g., the transformation of **x** to a preconditioned control variable and the minimization algorithm).

As is common practice, observation errors are assumed to be uncorrelated, hence the observation error covariance matrix **R** is diagonal. The observation error variances are specified according to estimated errors for the various observational platforms (**Error! Reference source not found.**). Given the lack of reliable statistics n the scales of the background error correlation, and the practical issues of analyzing observations with very different network density (e.g., mesonet versus radar), multiple analysis passes are used to analyze different data types with different (recursive) filter de-correlation scales in order to account for the variations in the observation spacing among different data sources. Here we define the filter de-correlation scale as the radius at which the weight given to the observation in the recursive filter is e-folded. The choice of the filter de-correlation scales is guided by the density of observational networks whose data are analyzed within each pass. Such a procedure was used in earlier studies based on the ARPS 3DVAR (e.g., Hu et al. 2006a,b), and a similar procedure using multiple passes with variable spatial correlation scales is used in the ARPS Data Analysis System (ADAS, Brewster 1996) based on a successive correction method (e.g., Xue and Martin 2006).

A.2 The Cloud Analysis

Variational analysis of reflectivity in 3DVAR is difficult because of the lack of physical constraints to properly attribute to the contributions of multiple hydrometeor species to the reflectivity. A direct link between reflectivity and temperature (or moisture) does not exist and therefore reflectivity cannot directly update these variables within a 3DVAR framework without reliable flow-dependent cross covariance. For these reasons, we employ a complex cloud analysis procedure to assimilate reflectivity data, that has proven effective in past studies (Xue et al. 2003; Hu et al. 2006; Zhao and Xue 2009). The cloud analysis is performed as an additional step after the 3DVAR analysis, and utilizes the 3DVAR analysis to provide background information, including that of vertical velocity to determine if convection is present in a particular column.

Within the cloud analysis, the remapped reflectivity data are used to estimate hydrometeor fields via the (Kessler 1969) reflectivity equation for rainwater and (Rogers and Yau 1989) equations for hail and snow. The in-cloud temperature and moisture fields are estimated by assuming a modified moist-adiabatic ascent that accounts for entrainment as presented by Hu et al. (2006a). Because radar-observed reflectivity is generally much more reliable than the model prediction, the hydrometeor fields estimated from observations replace the background field everywhere observations are available. This helps to remove spurious precipitation in the forecast background. Where reflectivity observations are not available, the background field is retained. More information on the cloud analysis can be found in Zhang et al. (1998), Zhang (1999), Brewster (2002), and Hu et al (2006).

The cloud analysis was originally developed to alleviate the spin-up problem for forecasts beginning from a coarse-resolution analysis. Repeated application of the original cloud analysis in the high-frequency assimilation cycles of our study, however, led to unrealistic warming in the middle-troposphere. To mitigate this problem, the cloud analysis was modified so that the cloud water and water vapor mixing ratios were only adjusted during the first application of the analysis. In subsequent analyses, only the hydrometeor mixing ratios (rain, snow, and hail) and in-cloud temperatures were adjusted.